UNIVERSITÀ DEGLI STUDI DI PADOVA

Sede Amministrativa: Università degli Studi di Padova

Dipartimento di Fisica "G.Galilei"

SCUOLA DI DOTTORATO DI RICERCA IN FISICA

CICLO XXI

STUDY OF EXTERNAL FIELDS AROUND MAGNETARS AND ANALYSIS OF INTERSTELLAR ABSORPTION

Direttore della Scuola: Ch.mo Prof. Attilio Stella

Supervisore: Ch.mo Prof. Roberto Turolla

Co-supervisore: Dr. Silvia Zane

Dottoranda: Lucia Pavan

2 febbraio 2009

alla mia famiglia

Contents

Prefazione

Gli argomenti trattati nella presente tesi sono due: l' analisi del campo attorno a stelle di neutroni iper-magnetizzate (Magnetar) e la distribuzione dell' assorbimento interstellare nella nostra Galassia.

Le Magnetar sono state introdotte come modello teorico per spiegare le caratteristiche peculiari di un ristretto sottoinsieme di stelle di neutroni isolate, circa 15 oggetti su piú di 2000 noti. Nonostante siano così pochi, questi oggetti sono argomento di numerosi studi a causa delle loro proprietà estreme. All'interno del modello di magnetar, l'emissione di queste sorgenti viene spiegata come energia rilasciata dal campo magnetico (da cui il nome) piuttosto che da riserve di energia rotazionale, gravitazionale o termica come avviene per la maggior parte delle stelle di neutroni. Dalle misure dei periodi orbitali e dalla loro variazione nel tempo, i campi magnetici coinvolti sono stimati essere dell'ordine di 10^{14-15} G (10^{10-11} T), portando queste stelle ad essere "i magneti più intensi" dell'Universo. In questo quadro, lo studio delle magnetars apre la possibilità di analizzare gli effetti di campi magnetici su plasmi in condizioni davvero estreme. I campi magnetici che vengono trattati superano la soglia $B_{QED} \sim 4 \cdot 10^{13}$ G ($4 \cdot 10^{9}$ T) e quindi provocano grandi alterazioni delle proprietà intrinseche della materia (per una review si veda Harding & Lai [59]). Campi così intensi non solo interagiscono pesantemente col plasma modificando la struttura atomica della materia, ma alterano anche le proprietà del vuoto. Uno degli aspetti più significativi é la polarizzazione del vuoto che introduce i modi ordinario e straordinario di propagazione dei fotoni .

L'unico strumento per studiare questi oggetti è l'analisi della radiazione emessa; questo è il motivo per cui sono stati compiuti grandi sforzi per creare modelli sintetici di spettri delle magnetars. Lo scopo di queste ricerche è di derivare, indirettamente dagli spettri raccolti, alcuni vincoli sulle condizioni fisiche delle zone emittenti, sia sulla superficie della stella che nella magnetosfera.

Il modello è stato sviluppato in vari articoli a partire dal 1992 con il lavoro di Thompson e Duncan. Nel 2002, in un articolo di Thompson, Lyutikov e Kulkarni, il campo esterno delle magnetars è stato descritto come un dipolo twistato attorno al proprio asse magnetico. In questo modello una torsione si propaga dalle zone interne e gradualmente deforma la crosta, provocando una distorsione anche nel campo esterno. I burst osservati sarebbero quindi alimentati dall'improvviso rilascio di una grande quantità di energia dovuta a fratture della crosta, che avvengono quando lo stress sulla superficie diventa troppo forte. Assumendo questa configurazione del campo, il modello é in grado di riprodurre le caratteris-

tiche spettroscopiche della maggior parte delle Anomalous X-Ray Pulsars e dei Soft Gamma Repeaters. Sorprendenetemente il modello delle magnetar suggeriva anche un legame tra queste due classi di oggetti, che è stato confermato in seguito, dalla scoperta di oggetti con proprietà intermedie tra le due classi. Ciò nonostante, a mano a mano che nuovi studi vengono condotti sull'emissione delle magnetar, il modello necessità di essere affinato. Alcuni lavori recenti, ad esempio, suggeriscono o che le zone emittenti siano piccole e non coprano l'intera superficie della stella, oppure che siano presenti zone a diversa temperatura sulla superficie. In alcuni casi, il twist sembra essere confinato solo a delle porzioni della magnetosfera e/o il campo, su larga scala, sembra essere più complesso di un semplice dipolo.

Gli studi condotti si inseriscono in questo quadro e sono rivolti a generalizzare il modello esistente. L'idea che è stata seguita è quella di includere delle variazioni del campo su piccola scala considerando multipoli di ordini diversi. A differenza di quanto accade per campi generici, in questo caso il procedimento è complicato della non linearità delle equazioni che descrivono i campi twistati.

Il capitolo 1 descrive le Anomalous X-Ray Pulsars e i Soft Gamma Repeaters nel contesto delle stelle di neutroni isolate (INSs), introducendo anche alcune altre classi di INS che sono probabilmente collegate tra loro ed anche ai candidati magnetars. Questa descrizione fenomenologica è seguita da una breve descrizione del modello delle magnetars.

Il capitolo 2 tratta le proprietà dei campi di "force free" che sono una parte essenziale del modello e costituiscono il soggetto principale degli argomenti che seguono. Nei due capitoli successivi si descrive il lavoro svolto per ampliare il modello di dipolo assisimmetrico. In particolare, viene fatta distinzione tra due diversi aspetti: l'introduzione nel modello di multipoli ancora assisimmetrici, e quella invece di campi non assisimmetrici. In quest'ultima parte vangono presentate le equazioni ricavate in questo lavoro, e che descrivono il campo magnetico esterno delle magnetar, valide sia per descrivere campi intrinsecamente non assisimmetrici, che per campi il cui asse di simmetria sia orientato arbitrariamente rispetto ad una terna cartesiana. Le conclusioni di questo lavoro sono riportate nel capitolo 4.2.1.

Il secondo argomento di questa tesi riguarda l'assorbimento interstellare nella nostra Galassia. L'estinzione interstellare è oggetto di molti studi in quanto modifica la radiazione osservata proveniente dalle sorgenti celesti. Le polveri e le particelle interstellari non emettono radiazione, ad eccezione dell'emissione infrarossa, dovuta a silicati e idrocarburi policiclici aromatici, e dunque sono molto difficili da analizzare. Generalmente, il mezzo interstellare è visibile solo quando viene illuminato da altre sorgenti, quindi, ove possibile, viene misurato direttamente dalla radiazione emessa da oggetti lontani ed osservata sia analizzando righe spettroscopiche di bassa ionizzazione che da analisi fotometriche.

Questi metodi tuttavia, forniscono una misura dell'estinzione solo tra l' osservatore e alcuni oggetti, ma non coprono estensivamente tutto il cielo. Per ottenere misure di estinzione laddove le misure non sono presenti, generalmente viene impiegato un modello di distribuzione delle polveri nella Galassia. Alcuni di questi modelli sono descritti nel capitolo 5 insieme ad una breve introsuzione sull'estinzione interstellare.

Mentre i vantaggi riguardanti l'uso dei modelli di estinzione sono evidenti, dato che permettono di ricavare la quantità di estinzione anche in zone dove le misure sono assenti, lo svantaggio é dovuto alla necessitá di adottare delle assunzioni sulle proprietà delle stelle e/o sulle polveri della Galassia, che introducono ulteriori incertezze nel risultato finale. Un approccio differente è basato sull'analisi dell'emissione infrarossa delle polveri (Schlegel, Finkbeiner & Davis [106]) per mappare il mezzo interstellare. Purtroppo anche questo metodo ha delle limitazioni, in quanto fornisce informazioni solo sull'intera column density in una determinata direzione, senza la possibilitá di risolvere la struttura tridimensionale della distribuzione del mezzo interstellare.

In questo contesto il presente lavoro è rivolto alla realizzazione di un algoritmo utile ad interpolare le misure di estinzione disponibili in letteratura, senza dover ricorrere ad un modello per le componenti della Via Lattea. L'idea che è stata seguita è quella di raccogliere la maggior quantità possibile di dati di assorbimento, al fine di ottenere una mappa tridimensionale (seppur grossolana) dell'estinzione nella nostra Galassia, e interpolare questi dati per ricavare il valore di assorbimento in posizioni diverse da quelle già note.

Poiché l' estinzione è una misura cumulativa dell'assorbimento distribuito tra l'osservatore e la stella, prima di interpolare i dati è necessario effettuare fare una scomposizione degli assorbimenti misurati in valori locali di assorbimento. Lo strumento matematico usato è descritto nel capitolo 6 insieme ad alcuni risultati preliminari del codice che è stato sviluppato. Le conclusioni di questa seconda parte sono nel capitolo 6.3.3.

Preface

This thesis describes mainly two topics: the analysis of the external field of hypermagnetized neutron stars (magnetars), and the distribution of galactic interstellar absorption.

Magnetars have been introduced as a theoretical model to account for the peculiar characteristics of a limited group (~ 15 objects out of more than two thousands known) of isolated neutron stars. Though being so few, these objects are extensively studied due to their extreme properties. In the magnetar model, the emission of such sources is explained as energy released from the magnetic field (hence the name) rather than from rotational, gravitational or thermal energy as for the majority of the neutron stars. From measures of spin periods and their variations, the magnetic fields involved are estimate to be of order 10^{14-15} G (10^{10-11} T), making these stars the 'strongest magnets' of the Universe. In this frame the study of magnetars opens the possibility to analyze the effects of the magnetic fields on plasma under really extreme conditions. The magnetic fields we deal with exceed the quantum threshold $B_{QED} \sim 4 \cdot 10^{13}$ G ($4 \cdot 10^{9}$ T) and cause strong alterations of the properties of matter (for a review see Harding & Lai [59]). Not only such an intense field strongly interacts with the plasma and modify the atomic structure of matter, but it also modifies the properties of vacuum too. One of the more noticeable effectsis the vacuum polarization that alters the propagation of photons introducing ordinary and extraordinary modes.

The only tool to study these objects is the analysis of their emitted radiation. This is the reason why a great effort has been devoted to synthetically model the spectra of magnetars. The aim of these studies is to take into account the known effects of the field and indirectly derive, from the collected spectra, some constraint on the physical conditions in the emitting zones, both on the star surface and in the magnetosphere.

The magnetar model has been developed in different works, starting in 1992 with the one of Thompson and Duncan. In 2002, in a paper by Thompson, Lyutikov and Kulkarni, the external field of magnetars was described as a sheared dipole. In this model the torsion comes from the interior and gradually twist the crust, shearing, as a consequence, the external field too. The bursts are fueled by a sudden release of great amount of energy due to fractures of the crust occurring as the stress imparted from the field become too strong. Assuming this configuration of the field, the magnetar model is able to reproduce the spectral behaviour of the majority of the Anomalous X-Ray Pulsars and Soft Gamma Repeaters. Surprisingly, the magnetar model also suggested a link between these two classes that had become clearer only when a number of sources with intermediate properties between the

two has been discovered. Nevertheless, as more studies are conducted on magnetar spectra, the underlying model need to be refined. Some recent works suggest, for example, small emitting zones that do not cover the entire star, or the presence of different temperatures on the surface of the magnetars. In some cases there are indications that the twist may be confined only to a portion of the magnetosphere, and/or that the large scale field is more complex than a simple dipole.

The studies conducted in this work follow this researchline, and are intended to extend the preexisting model. The followed idea is to include field variations on small scales, achieved considering multipolar fields of various orders.

Chapter 1 describes Anomalous X-Ray Pulsars and Soft Gamma Repeaters in the context of isolated neutron stars (INSs), introducing some other, possibly related, classes of INSs. This phenomenological description is followed by an overview of the magnetar model.

Chapter 2 deals with the properties of "force free fields" as these are essential to the model and constitute the main subject of the subsequent discussions. In the two following chapters, the description of the efforts done to extend the axially symmetric dipolar model are reported. In particular efforts were devoted in developing two different aspects: the study of axially symmetric multipoles, and that of non-symmetric fields. In this last part, then, new equations are introduced, that are suited to describe both symmetric fields, whose axis of symmetry is arbitrarily oriented with respect to a Cartesian coordinate system, and fields that are intrinsically not symmetric. Conclusions of this work are drawn in Chapter 4.2.1.

The other subject of this work deals with interstellar absorption in our Galaxy. Interstellar extinction is the subject of many studies, as it modifies the radiation emitted by all the sources. As the dust and the interstellar particles are not emitting (with the exception of the infrared emission from silicates and polycyclic aromatic hydrocarbon (PAH) molecules), they are particularly difficult to analyze. Generally the interstellar absorbing medium is visible only when illuminated from starlight; therefore, when possible, it is directly measured by the collected radiation, both analyzing low-ionization lines in spectra, and from photometric analysis. These methods, though, give a measure of extinction only for a number of objects and cannot cover extensively the observed sky. To obtain a value for the extinction towards directions for which there are no available measures, it is common to use a model of the distribution of dust in the Galaxy. Some of these models are described in Chapter 5 together with a brief introduction on interstellar extinction.

While the advantages of an extinction models are evident, as they allow to infer absorption quantities even where there is a lack of measures, the disadvantage is the need to make assumptions on the stellar and/or dust components of the Galaxy. This introduces again other uncertainties on the final result. A different approach is based on the analysis of the dust infrared emission (Schlegel, Finkbeiner & Davis [106]) in order to map the interstellar medium. Unfortunately even this method has limitations, as it gives informations only on the total column density in each direction, without the possibility to resolve the three

dimensional structure of the distribution of interstellar medium.

In this context the work performed in this thesis aims at constructing an algorithm to interpolate the extinction measures available in literature, without recurring to a model of the Milky Way components. The idea followed is to collect the greater possible set of absorption data, in order to create a coarse-grained three dimensional map of the galactic extinction, and interpolate these data to infer the values between the known points. As extinction is a cumulative measure of the absorption occurring between the observer and the star, before interpolating the data, a deconvolution of these measured quantities into local values of absorption, is needed. The mathematical tool used is described in Chapter 6 together with some preliminary results obtained with the developed code. Conclusions are drawn in the final chapter (Chap. 6.3.3).

Part I

Chapter 1

Neutron Stars and Magnetars

As soon as the neutron was discovered in 1932, Baade & Zwicky [5] theorized that supernovae explosions may end up in the production of a star mainly composed of neutrons. In the modern picture, neutron stars are compact objects formed at the end of the evolution of massive stars (i.e. having masses approximately in the range 8–20 $M_{\odot}$). During its evolution the star burns progressively heavier elements, with rapidly decreasing time-scales, until silicon burning is reached. At this stage nuclear fusion produces iron, whose burning is an endothermic process and therefore cannot take place in the stellar core. The iron core cannot balance gravity; the core density increases and the electron degeneracy (any further compression going against Pauli exclusion principle) becomes responsible for the pressure that balances the gravitational force. Once the core mass exceeds the Chandrasekhar limit of $1.44M_{\odot}$, the degeneracy pressure can no longer support the star, the core implodes and its temperature drastically increases, producing γ-rays. The principal reactions at this stage (photodisintegration) are

$$
\begin{aligned}
{}^{56}Fe + \gamma &\rightarrow 13\,{}^{4}He + 4n \\
{}^{4}He + \gamma &\rightarrow 2p^{+} + 2n
\end{aligned}
$$

which cause the core to become richer and richer in free nucleons. As soon as the density becomes greater than $\sim 10^{7}$ g/cm^{3}, inverse β decay

$$
e^{-} + p^{+} \rightarrow n + \nu_{e} \tag{1.1}
$$

becomes energetically favorable, and consequently neutrons become stable. The energy released in the neutronization process produces a shock wave that is sufficient to eject the outer part of the star, igniting a core-collapse supernova explosion (SN II) on a timescale of milliseconds. As the core temperature decreases, a neutron star (or a black hole, whether the progenitor mass exceed $\sim 20M_{\odot}$) forms. Recent evidence has been found that the progenitors of ultramagnetized neutron stars had $M > 40M_{\odot}$ (e.g. [89]).

The observation of neutron stars began when in 1942 both Baade [4] and Minkowski [88] studied the Crab nebula, realizing that the bulk of the optical emission is due to the inner

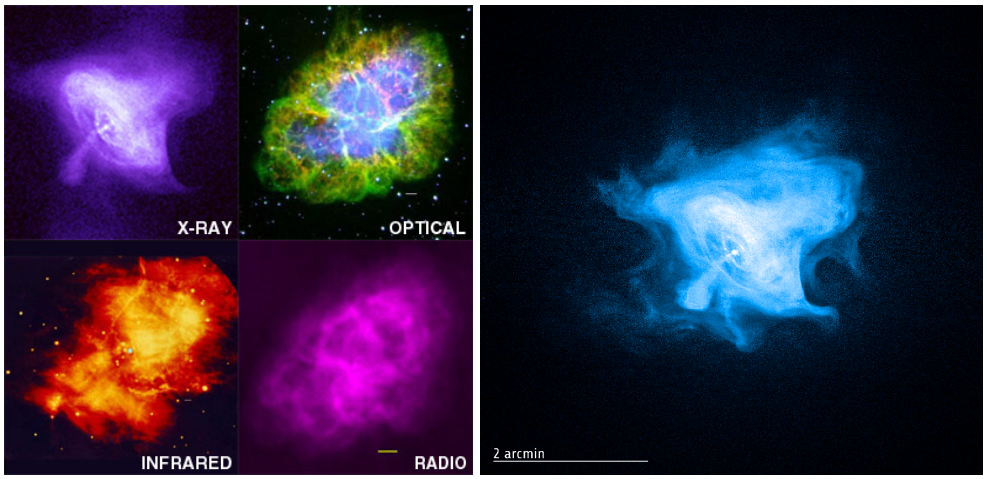

(a) *Various emitting mechanism and state of the plasma are visible at different wavelengths.*

(b) *Chandra X-Ray Telescope observation.*

Figure 1.1: *Crab nebula at different wavelengths. (a) Pictures of the Crab nebula at X-ray (Chandra), optical (Palomar), infrared (Keck), and radio (VLA) wavelengths, showing the different emitting regions and different processes. The central pulsar is directly visible only in the Chandra observations. (b) Observation of the Crab nebula, obtained with the Chandra X-Ray Telescope, reveal the central neutron star, the emitting jets and the inner flowing wind that likely is regulated by a toroidal magnetic field.*

part of the nebula. An estimate of mass and radius of the star responsible for the continuum emission lead to the identification of a very high density star at the center of the nebula, even if the idea of a neutron star was still to be accepted by astronomers. Later, the analysis of the Crab nebula at radio wavelengths triggered the explanation of the emission mechanism as synchrotron radiation due to the motion of relativistic electrons in a strongly magnetized region. Increasingly more insights on this object were obtained combining observation of the nebula at different wavelength (fig. 1.1a), opening the way to the neutron star identification and the current interpretation of the whole emission mechanism. The neutron star lurking in the center of the nebula is the object responsible for the constant feed of relativistic electrons. In 1968, after X and γ rays observations, the emission was recognized to be pulsed, proving that the star, with an estimated radius of nearly 25 km, is spinning with period of $3.3 \cdot 10^{-2}$ s with an increasing rate of $4.4 \cdot 10^{-13}$ s s^{-1}. The star besides is endowed with a strong magnetic field whose effects can be seen also in the surrounding plasma, thus being among the first observed pulsars (PSR B0531+21).

At the moment of the core collapse, neutron stars acquire great rotational speeds as a direct consequence of angular momentum conservation. Frequently thus, a newly born neutron star is spinning very fast, with $P \lesssim 10^{-2}$ s.

Pulsars are magnetized rotating neutron stars, emitting the bulk of the radiation into two beams expanding over the north and south magnetic poles, as it can be seen in X-ray images of the Crab pulsar (fig. 1.1b). The magnetic polar axis and the rotational axis are not aligned, causing the emitting regions to move with respect to the observer. The electromagnetic signal collected therefore shows a pulsation that is a signature of the rotational period of the star. Commonly observed periods are in the range $\sim 10^{-3} - 10$ s. The rate at which the neutron star looses its angular momentum is observed in the range $10^{-21} - 10^{-10}$ s s^{-1}. The

$P-\dot{P}$ diagram (fig. 1.2) for neutron stars is as important as the Hertzsprung-Russel diagram for ordinary stars.

Neutron stars, and pulsars as well, could be observed either as components of binary systems, or as isolated objects. In the first case often the source is powered by accretion of material from the companion that usually cause X-ray emission, while in the isolated cases generally the emission is sustained by rotational energy release. Of the known 1800 radio pulsars, approximately 1650 are isolated objects.

1.1 Isolated NSs

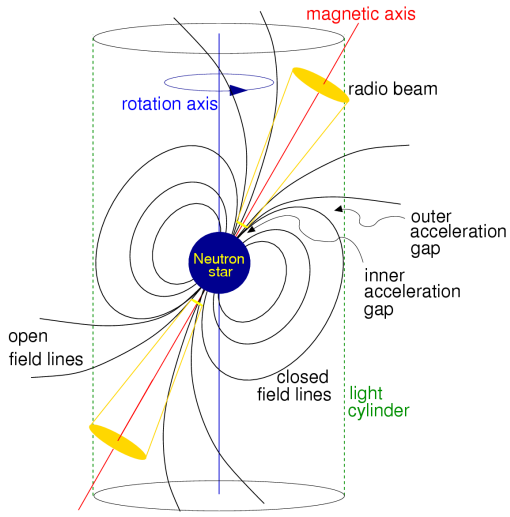

Figure 1.3: *Schematic representation of a pulsar.*

An isolated pulsar is sketched as an oblique rotator in vacuum, and its magnetic field, at a first order approximation, could be considered as a dipole (dipole model, Pacini 1967, see fig. 1.3). The total radiated power is given by the Larmor formula

$$\dot{E} = \frac{2\,\Omega^4\,|m|^2\sin^2\alpha}{3c^3}\ \mathrm{erg/s} \qquad (1.2)$$

where Ω is the rotational velocity, α is the angle between spin and magnetic axis, m is the magnetic dipole moment $|\vec{m}| = B\,r^3/2$ (with B the field intensity). Radiative losses spin down the star as the rotational energy decrease as

$$\begin{aligned}\dot{E} &= -\frac{\mathrm{d}}{\mathrm{d}t}\left(\frac{1}{2}I\Omega^2\right)\\ &= -I\Omega\dot{\Omega} \qquad (1.3)\\ &= 4\pi^2 I\frac{\dot{P}}{P^3} \sim 3.95\cdot 10^{46}\frac{\dot{P}}{P^3}\ \mathrm{erg/s}\end{aligned}$$

considering standard values for a neutron star, mass $M = 1.4\ M_\odot$, radius $r = 10$ km, and moment of inertia $I = kMr^2 = 10^{45}$ g/cm^2 (with k intermediate among $k = 2/5$ -solid sphere- and $k = 2/3$ -thin shell-).
Comparison of equation (1.2) and (1.3) gives the magnetic field strenght as a function of P and $\dot{P}$

$$B = \sqrt{\frac{3\,c^3 I}{2\pi^2\,r^6\sin^2\alpha}\,P\dot{P}} \sim 6.4\cdot 10^{19}\sqrt{P\dot{P}}\ \mathrm{G} \qquad (1.4)$$

Magnetic fields for classical radio pulsars, as inferred from the dipole formula, are in the range 10^{11-13} G. The spin-down luminosity, generally, takes account for the whole radio emission of classical radio pulsars as well as for the energy released through a relativistic wind.

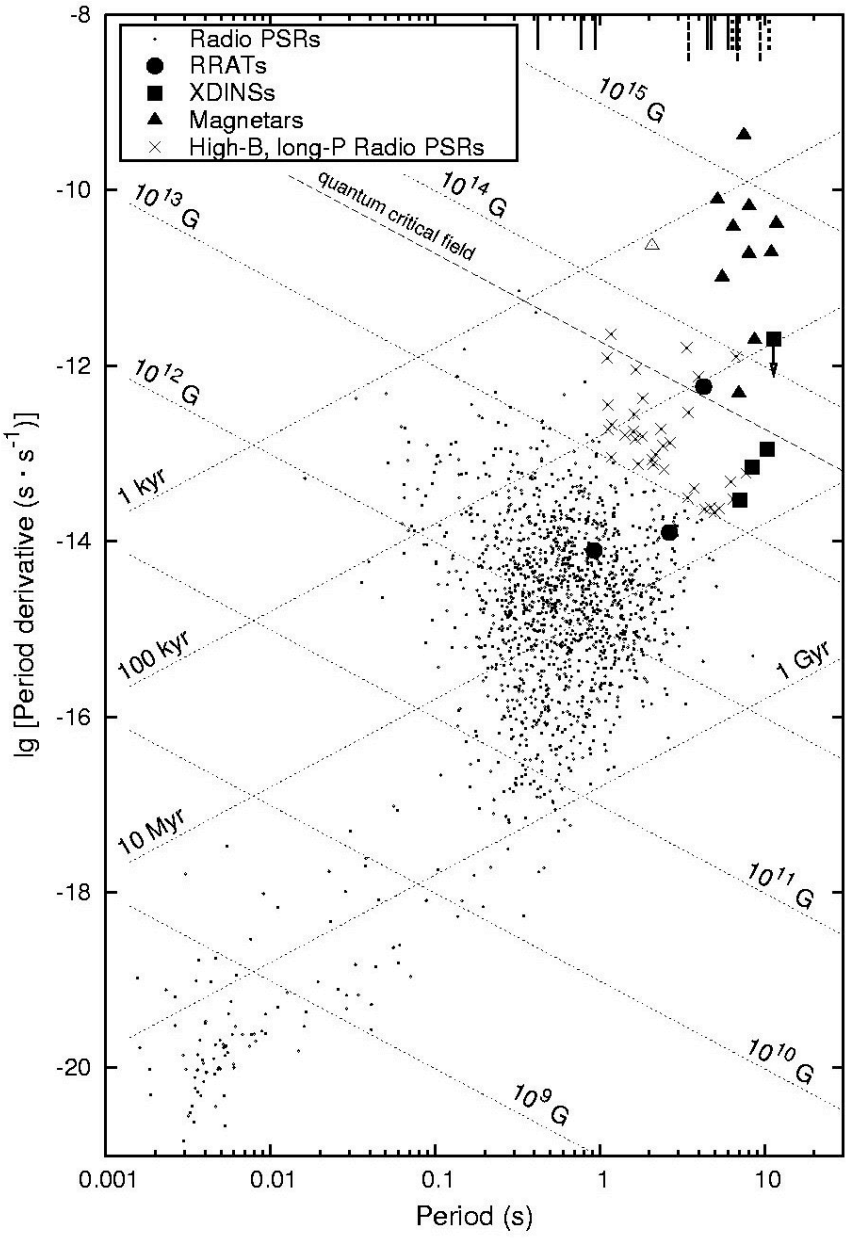

Figure 1.2: *Period- period derivative diagram for pulsars: in the lower-left corner there are millisecond pulsars (generally formed in binary systems), in the central part of the diagram the bulk of galactic radio pulsars, while magnetar candidates are in the upper right part. Also shown are the lines of constant magnetic field and characteristic age, obtained with eqn.s (1.4) and (1.6). The picture has been taken from Kondratiev et al. [66].*

From equation (1.4) in the case of constant magnetic field we obtain $P\dot{P} = \text{const}$; by integrating such expression it follows

$$\begin{aligned} P\dot{P} &= k \\ \int_{P_0}^{P} P \, \mathrm{d}P &= k \int_0^{\tau} \mathrm{d}t \\ \frac{1}{2}(P^2 - P_0^2) &= k\,\tau = P\dot{P}\,\tau \end{aligned} \tag{1.5}$$

Assuming a fast rotating progenitor, such that P_0 become negligible with respect to P (and can be assumed $P_0 = 0$), the expression for the characteristic age of pulsars is recovered

$$\tau = \frac{P}{2\,\dot{P}} \tag{1.6}$$

From the measures of periods, thus, both the magnetic field and the characteristic age of the pulsars can be inferred. In the cases of known epoch of the supernova explosion, particularly for Crab and Vela pulsars that are very young objects ($\tau \lesssim 10^3$ yr), the value found by means of this formula is in agreement with the true age of the neutron star. The estimates though fails for older objects.

While the majority of isolated neutron stars (INSs) are indeed classical radio pulsars, recently, particularly in the last decade, there had been X and γ rays, observations that revealed a number of different objects. These are classified as X-ray dim isolated neutron stars (XDINS), rotating radio transients (RRATs), central compact objects (CCOs), Soft Gamma Repeaters (SGRs) and Anomalous X-ray Pulsars (AXPs). All these objects are quite rare, each class counting $\lesssim 10$ sources. Nevertheless these sources exhibit very peculiar phenomenology. It is still not clear if these classes are representative of a variety of neutron star or if they are linked by some evolutionary path. For a review on all these classes see e.g. Popov [100].

1.1.1 X-ray Dim Isolated Neutron Stars

XDINS (also known as 'The Magnificent seven') are a class of seven close-by stars (with distances around a few hundred pc), the first of which (RX J1856-3754) has been discovered in 1995. This first object shows no features at all in the collected spectrum and low amplitude pulsations (Drake et al. [35], Burwitz et al. [15], Tiengo & Mereghetti [117]). Though considered as the prototype of the class, it results to depart from the other members. All other six objects indeed show broad spectral features, not fully understood yet. Possible explanations are proton cyclotron lines or atomic transitions in presence of magnetic fields greater then 10^{13} G. The presence/absence of the features might depend on the viewing geometry, thus leading to an homogeneous class again. They all are recognized to be isolated. Spin periods have been detected for six sources, and are in the range 3-12 s. All the members of the class show soft thermal spectra, meaning that the emission is produced by the cooling surface, with blackbody temperatures $k_B T \sim 40 - 110$ eV and X-ray luminosities

in the range 10^{30-32} erg/s. There are no detection of hard X-rays tails, very faint optical counterpart, and no known radio emissions, Phase-dependent spectra have been detected on two sources (RBS 1223 and RX J0720.4-3125). Given the small distance, the birth rate of XDINS seem to exceed that of common radio pulsars (Popov, Turolla & Possenti [101]).
The properties of the Magnificent Seven are still to be successfully modeled, nevertheless some association among XDINS and magnetar candidates (see § 1.1.4 and § 1.2) have been suggested (Castro-Tirado et al. [21]).

1.1.2 Rotating RAdio Transients

RRATs are eleven sources, discovered only in 2005 in the Parkes Multibeam Survey. They emit very short radio bursts, lasting 2-30 ms at intervals of minutes or hours. (McLaughlin et al. 2006 Nature). When detected, periods are in the range 0.4-7 s and period derivative around $10^{-13}\ s\ s^{-1}$, giving hints of high magnetic fields and causing RRATS and XDINS to occupy the same region in the $P - \dot{P}$ diagram. Though been very few in number they can be even more frequent than normal radio pulsars, with birth rates comparable to that of XDINS. One member has been detected as a thermal X-ray source by Chandra.

1.1.3 Central Compact Objects

CCOs are X-ray sources located very close to the center of supernova remnants (SNr), with no detected emission in radio and γ-ray waveband. The emission is thermally distributed, with slighter higher temperatures than XDINS, and luminosities of 10^{33-34} erg/s. In some cases emitting areas, as inferred from spectral fits, are lower than 2 km in radius, probably indicating that is only a fraction of the star surface. In one of the sources (RCW103) there is a detected period as long as 6.7 hours. The origin of such period is not clear; it could be ascribed at orbital motion, thus suggesting a system similar to a polar, or it could be interpreted as spin period in extremely magnetized neutron star ($B > 10^{15}$ G) slowed down by some propeller mechanism. Interestingly also a completely opposite model has been proposed to account for CCOs properties, and in this case they should be extremely weakly magnetized stars (Gotthelf & Halpern [53]).

1.1.4 AXPs and SGRs

SGRs form the class with fewer objects (only 5 confirmed sources: SGR 1900+14, SGR 1806-20, SGR 1627-41 in the Galaxy and SGR 0526-66 in the Large Magellanic Cloud, and the last SGR 0501+4516 discovered on 22 August 2008). The first X-ray burst was detected already on 5 March 1979 from a source that was initially associated to a Gamma Ray Burst. Later, because of the regular pulsations in the flare tail, it was recognized to be a compact object spinning at 8s, located in the Large Magellanic Cloud and associated with a SNr. Such association, together with the proximity to massive star clusters, suggests that these objects are young neutron stars.
The main characteristic of the class is the emission of strong X-ray bursts that activate with

no periodicity and last typically less than 1 s. The weaker bursts are also the more numerous, and have typical duration of 0.1 s and luminosities approximately of 10^{41} erg/s. These weak bursts tend to cluster around more energetic ones (10^{41-43} erg/s) in periods of stronger activity. In addition to these normal events, gigantic bursts have been observed from three of the five sources. These are the so called 'giant flares'; the first one occurred on 5 March 1979 from SGR 0526-66, followed by a flare on 27 August 1998 emitted by SGR 1900+14, and the least one on 27 December 2004 by SGR 1806-20. The emission of these burst is characterized by an initial spike which extend up to the MeV range and lasts only a fraction of a second, followed by a long tail lasting a few minutes, showing a strong periodical modulation due to the rotation of the neutron star (see fig. 1.4) at the same periodicity observed in the quiescent emission.
The energy released during the giant flares exceed 10^{44-45} erg and in the case of 27 December event, it was almost 2 orders of magnitude higher than the peak luminosity observed in the other two flares. In the 27 August 1998 flare, although not the more energetic one, many X-

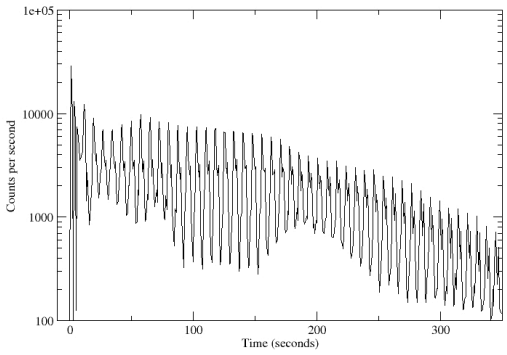

(a) *SGR 1806-20 on 27 December 2004.*

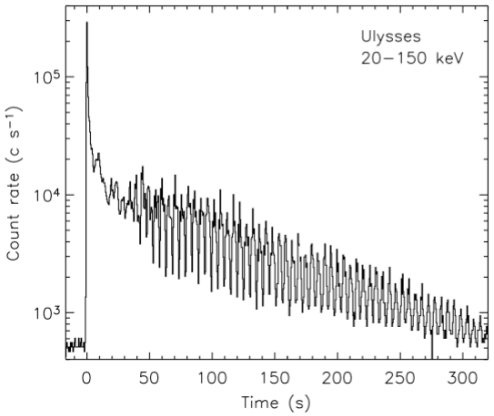

(b) *SGR 1900+14 on 27 August 1998.*

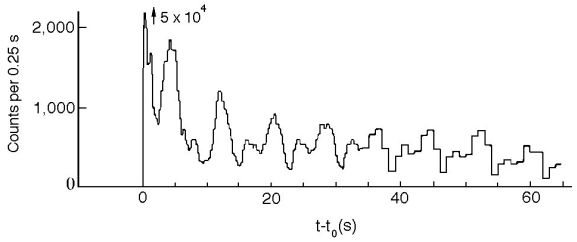

(c) *SGR 0526-66 on 5 March 1979.*

Figure 1.4: *Lightcurve of the three Giant Flares. Images from (a) Palmer et al. [96], (b) Woods & Thompson [129], (c) Mazets et al. [80].*

ray detectors saturated with the exception of Rossi X-ray Timing Explorer, that was pointing away from the burst region, and the geo-space detector Konus. Peak luminosity had been obtained from these data, and the γ-ray flux had sufficient intensity to ionize the Earth outer ionosphere.

Periods of SGRs are in the range 2.7-8 s. Together with the measured spin down rates, from equation (1.4) the inferred magnetic fields are as high as 10^{15} G.

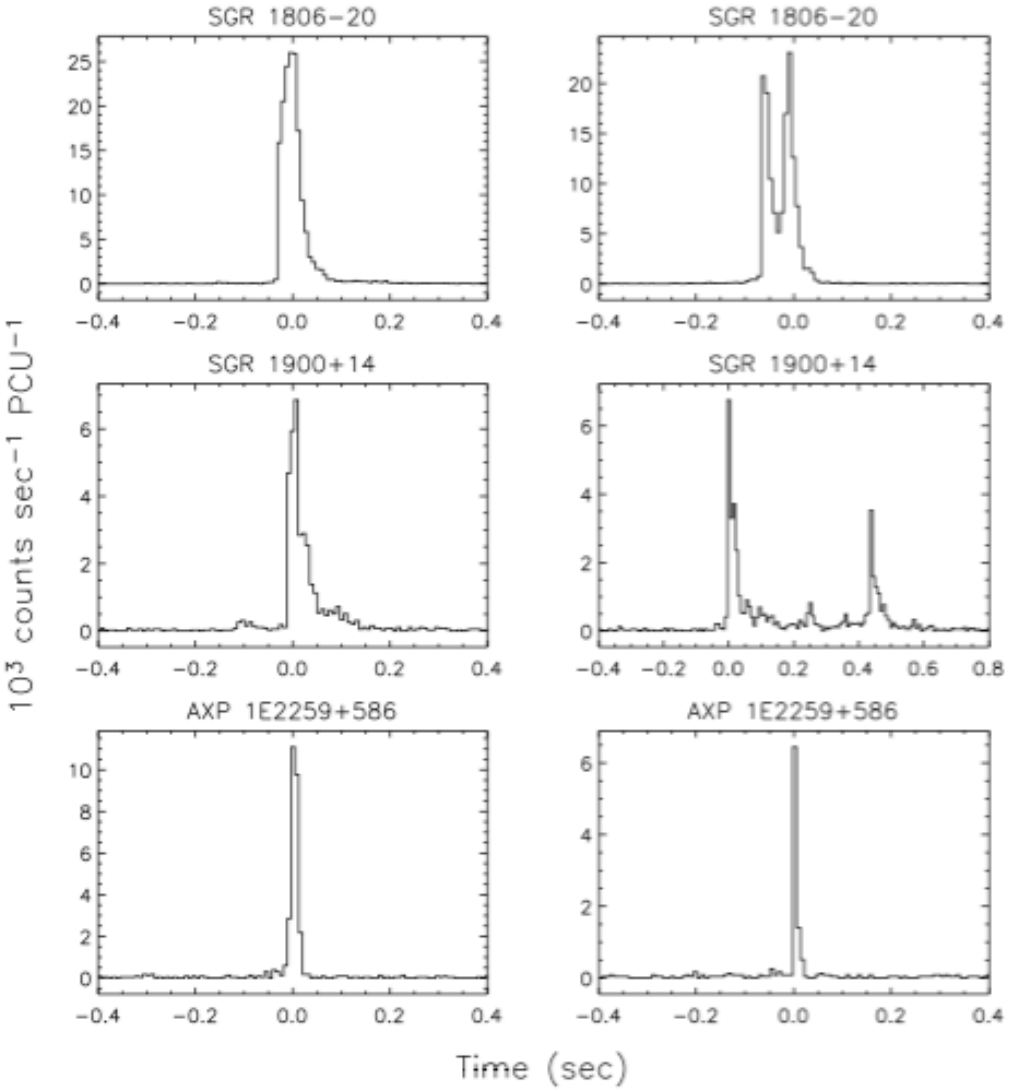

Figure 1.5: *Lightcurves of some typical bursts from SGRs and AXPs. Woods & Thompson [129]*

Recently one of the more interesting result was the reactivation of SGR1627-41 (Esposito et al. [42]) on 28 May 2008 after nearly a decade from the last period of activity.

AXPs are known sources but had been confused with normal X-ray accreting binary pulsars until 1995, when they had been recognized as independent class due to optical and IR observations that excluded the presence of companions. The persistent fluxes are of order 10^{34-36} erg/s. As more observations and X/γ-ray data became available, the similarities between SGRs and AXPs increased. These are rotational periods $P \sim 5$–12 s, absence of radio emission [up to now only the AXPs XTE J1810-197 and 1E 1557-54 have been detected in the radio, 19, 20] and persistent X-ray luminosities in the range $L \sim 10^{34}$–10^{36} erg/s. The spin down rates are similar too, but with AXPs values slightly lower, $\dot{P} \sim 10^{-10}$–10^{-11} s/s. Magnetic field intensities inferred from equation (1.4) are only slightly lower to those obtained for SGRs.

Though SGRs activity is higher, AXPs too show in some cases X/γ-ray bursts with peak luminosities, durations and morphologies similar to the SGR weak bursts (fig. 1.5). Thanks to *INTEGRAL* ISGRI and *RXTE* HEXTE, AXPs and SGRs are now known to be also persistent hard X-ray sources (e.g. Kuiper, Hermsen & Mendez [68], Kuiper et al. [69], Mereghetti et al. [82], Götz et al. [55]). Actually, their energy output in the $\sim$ 20–200 keV range may amount to as much as 50% of the total flux emitted above $\sim$ 1 keV. Recent, deeper *INTEGRAL* observations have shown that the hard X-ray emission is highly phase-dependent and probably results from the superposition of different spectral components [31, 32].

At variance with classical radio-pulsars, the persistent emission of SGRs/AXPs is $\sim$ 10–100 times higher than their rotational energy losses. This, together with the lack of detected stellar companions, indicates that the persistent emission of these sources is unlikely to be powered by rotation or accretion. The (dipolar) magnetic fields inferred from the spin-down measurements, $B \sim 10^{14} - 10^{15}$ G, largely in excess of the quantum critical field ($B_Q = 4.4 \times 10^{13}$ G), support the idea that SGRs and AXPs are ultra-magnetized NSs [or magnetars; 38, 112] and their (persistent and bursting) emission is sustained by the super-strong magnetic field. The discovery of a remnant disc around AXP 4U 0142+61 initially seemed to favor a scenario based on accretion from a debris disc left after the supernova event [e.g. 2, 40, 41], but the observed disk is likely to be a passive one, providing no contributions either to the spin-down or to the luminosity of the source, except in the IR.

During the last decade, not only the previous classes were discovered but also the region occupied by radio pulsar in the $P - \dot{P}$ diagram (fig. 1.2) has been extended. Thus a fraction of pulsars is now overlapping the region occupied by SGRs and AXPs. These sources, discovered by means of newer sensitive radio surveys, are the 'High field radio pulsars' (HBRP). Their presence is somehow puzzling, since the properties they display are very different from those of magnetars candidates, having smaller X-ray luminosity, no sign of bursts and being radio loud. The fields inferred from equation (1.4) are higher than the quantum threshold of $B_{QED} \sim 4.4 \cdot 10^{13}$ G (see § 1.2), thus suggesting that the dipolar external field intensity is not the only parameter discriminating between rotational and magnetar activity.
Another link between the two classes of sources has recently been found (Gavriil et al. [50]). The younger known pulsar PSR J1846-0258, with field strength of $4.9 \cdot 10^{13}$ G, originally was thought to be a classical rotationally-powered radio pulsar, but has now shown magnetar activity with a burst and enhanced flux and change in its timing behaviour.

1.2 The magnetar model

The magnetar model that has been widely used to account for the observational properties of SGRs and AXPs require these objects to be young neutron stars with extremely

intense magnetic fields, above the quantum threshold

$$B_{QED} = \frac{m^2 c^3}{\hbar e} \sim 4.4 \cdot 10^{13}\, G \tag{1.7}$$

at which the cyclotron energy equals the rest mass of the electrons. Such strong fields deeply modify the properties of plasma, as well as of atoms and of the vacuum itself. While atoms are distorted and elongated by the field, the vacuum behaves as a birefringent medium. One of the consequences is that photons propagate in two distinct modes, the ordinary and the extraordinary one. For a review on the physics in presence of extremely intense fields see e.g. Harding & Lai [59].

Both Soft Gamma Repeaters and Anomalous X-ray Pulsars are magnetar candidates. This is in part motivated by measures of P and $\dot{P}$ that lead to extremely intense magnetic field estimates, but also by their emission properties (particularly during the Giant Flares). The first argument supporting these fields is the energy needed to power the giant flares, with luminosities as high as 10^{46}erg/s, moreover Alfvén speed of magnetic instabilities is in accord with the short duration of the strong initial spike Schwartz et al. [107]. The magnetic energy reservoir indeed can sustain persistent X-ray emissions of $\sim 10^{35}$ erg/s for approximately 10^4 years. Another argument that favors the magnetar hypothesis is the strong (magnetic) braking that would have decelerate these sources to periods of a few seconds in a very short time. Both SGRs and AXPs are indeed thought to be young objects, because of the small height on the Galactic plane and the associations with region of stellar formations. The rapid spin down occurred on magnetars also explain why they are not detected at short rotational periods.

Thompson & Duncan [112] argued that fields as high as $3 \cdot 10^{17} \cdot (1\ \mathrm{ms}/P_0)$ G could be formed by turbulent dynamo amplification during the first few seconds of the formation of proto-neutron stars. The model requires very small initial periods, approximately of 1-2 ms, and the presence of convection. Under this scenario, because of the combination of strong fields and rapid rotation, magnetars are expected to have large spatial velocities (some 10^3 km/s). Moreover a strong initial magnetic braking should release $\sim 10^{52}$ erg, injecting additional energy on the expanding material around the proto-neutron star; high energetic supernova remnant are thus expected to be associated with these sources (Vink & Kuiper [124]). Unfortunately both these facts are not seen in magnetar candidates and, though this formation picture has not been completely ruled out, different mechanisms have been proposed.

One of these is the "fossil field" model (e.g. Kasumov & Allahverdiev [64], Braithwaite & Spruit [12], Ferrario...) based on magnetic flux conservation during the evolution and final collapse of the progenitor, that predicts the observed field distribution in neutron stars as a consequence of the properties of the progenitors. Magnetars thus would be the descendant of massive stars with the highest magnetic fields. Some evidences towards the association of magnetars with cluster of massive stars have already been found, as in the cases of SGR 1900+14 (DeLuca et al. [30]), SGR 1806-20 (Fuchs et al. [48]), CXO J164710.2-455216 (Muno

et al. [89]) and possibly 1E 1048.1-5937 (Gaensler et al. [49]). For the source CXO J164710.2-455216, associated with the cluster Westerlund 1, the initial mass of the progenitor would likely have been $M_i > 40 M_\odot$.

Persistent and bursting emission can both be explained in a quite natural way in the magnetar model. The magnetic field diffuse through the whole neutron star, towards the external layers, causing small-scale fractures in the (rigid) crust (Thompson & Duncan [114]) that seem to cause the X-ray bursts.

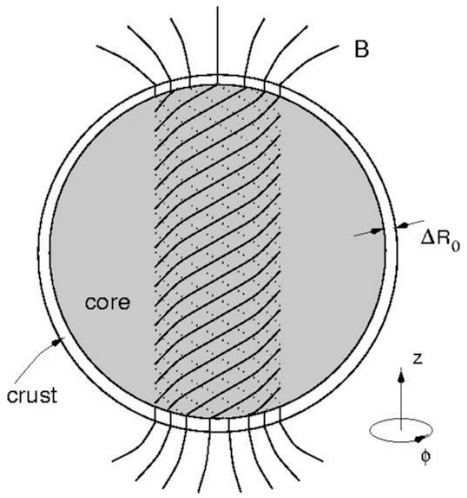

Figure 1.6: *Schematic representation of the internal field in a magnetar. The strong toroidal component causes a twist on the external field through footpoint motion (Thompson & Duncan [115]).*

The persistent emission is sustained by a twisting of the magnetosphere. Since the poloidal and toroidal components are expected to be in rough equipartition (see Thompson et al. [116] and references therein), the huge toroidal field stresses the crust, producing a deformation of the surface layers (see fig. 1.6). This, in turns, induces a rotation of the external field lines which are anchored to the star crust and leads to the appearance of an external toroidal component ($\boldsymbol{B}_\varphi \neq 0$). The properties of such a twisted magnetosphere have been investigated by Thompson et al. [116] by means of a model analogous to that for the solar magnetic field [e.g. 74, 127], under the assumptions of a static, dipolar, globally twisted field and enforcing, as in the solar models, the force-free condition. The twist of the crust provides the magnetosphere with electric currents, which are an additional source of heating for the stellar surface. These currents exceed by several orders of magnitude the intensity of Goldreich-Julian currents flowing along open field lines in canonical pulsars.

Currents flowing in the magnetosphere have a strong optical depth to Thomson scattering of the thermal photons emitted from the surface of the neutron star. As a result of these repeated scattering, the thermal spectrum is strongly modified, producing hard X-ray tails. The optical depth for such resonant cyclotron scattering is proportional to the twist of the magnetosphere, thus spectral hardening is expected in cases of increased twists. In magnetar candidates indeed spectral behaviour follows these predictions. Twisted magnetospheres produce even a stronger spin-down torque than the purely dipolar one, the twisted field decaying as r^{-p}, with a $p < p_{untwist} = 3$. A correlation between spin-down and spectral hardening has been reported already in 2001 by (Marsden & White [79]). Recently many efforts have been done to construct detailed 3-D Monte Carlo simulations [43, 93, 94] that can take into account the repeated scattering occurring in the magnetospheres. Partic-

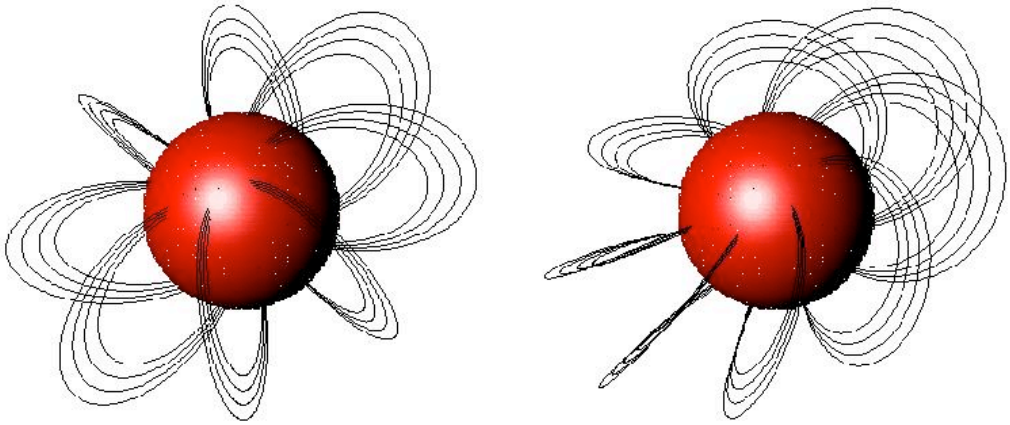

(a) *potential dipole.* **(b)** *twisted dipole.*

Figure 1.7: *Field lines in a pure (left) and twisted (right) dipolar magnetosphere. The twist angle between north and south polar caps in the right panel is* $\Delta\phi_{NS} = 1.8$ *rad.*

ularly the model by Nobili, Turolla & Zane [94] provides a detailed relativistic correction to the cross section of the flowing particles. In some cases this model had been successfully used to fit observed spectra Rea et al. [103] though more details seem to be needed in the field geometry.

The origin of the high-energy tails discovered with *INTEGRAL* is much less understood. Thompson & Beloborodov [111] analyzed different mechanisms within the magnetar model, and suggested that the hard X-rays may be produced either by thermal bremsstrahlung in the surface layers heated by returning currents, or by synchrotron emission from pairs created higher up in the magnetosphere. Quite interestingly, Baring & Harding [6] and Baring & Harding [7] have recently proposed a further possibility, according to which the soft gamma-rays may also originate from resonant up-scattering of seed photons, if a population of highly relativistic electrons is present in the magnetosphere [see also 94].

Since the conduction current in a sheared magnetosphere is $\propto \boldsymbol{\nabla} \times \boldsymbol{B}$, the particle density and hence the optical depth to resonant scattering depends on the shear (Thompson et al. [116]). Moreover, the global topology of the magnetic field influences scattering even for fixed shear. A globally twisted dipolar field will in general give rise to a different spectrum from that of a globally twisted quadrupolar field with the same twist angle. Because the spatial distribution of charges is not homogeneous [116], changes in shear and/or field topology are going to produce differences not only in the spectral shape, but also in the pulse shape of the received radiation. Some complicated pulse profiles from SGRs have already been explained by invoking higher order multipoles [e.g. 115, 44]. Moreover, recent data both for AXPs and SGRs seem to point towards the presence of a localized, rather than global, twist [e.g. 130, 98]. However, no investigation which includes multipolar components or localized twists have been presented up to now.

Chapter 2

Force Free Fields

The study of rarefied, static and highly magnetized plasmas lead, among other, to the analysis of the so called "force free" electromagnetic fields. These fields are important in many areas, from tokamak and other magnetic confinement devices (e.g. Rosenbluth & Bussac [105], Garcia de Andrade [51], Xie et al. [131]), to astrophysical plasma systems such as the solar corona or the sun active regions (e.g. Low [72], Low & Lou [74], Wolfson [127]), as well as the magnetosphere around pulsars (e.g. Mestel [86], Uzdensky [123], Goodwin et al. [52], Timokhin [118], Gruzinov [56]) and magnetars (e.g. Thompson et al. [116], Lyutikov [75], Mastrano & Melatos [78]).
The relative intensity between gravitational, pressure and magnetic forces acting on the plasma is characterized by the parameter $\beta = 8\pi n k_B T/B^2$, where n is the number density of particles, nk_BT is the plasma thermal energy density and $B^2/8\pi$ is the magnetic energy density. In all the mentioned examples the plasma is characterized by low β values ($\beta \ll 1$) meaning that the pressure gradients and gravitational effects can be neglected with respect to the magnetic forces. The standard set of magneto-hydro-dynamical (MHD) equations governing such a plasma are

$$\frac{\partial \rho}{\partial t} + \boldsymbol{\nabla} \cdot (\rho \boldsymbol{v}) = 0 \tag{2.1a}$$

$$\boldsymbol{\nabla} \times \boldsymbol{B} = \frac{1}{c}(4\pi \boldsymbol{j} + \frac{\partial \boldsymbol{E}}{\partial t}) \tag{2.1b}$$

$$\rho \frac{\partial \boldsymbol{v}}{\partial t} + \rho(\boldsymbol{v} \cdot \boldsymbol{\nabla})\boldsymbol{v} = -\boldsymbol{\nabla} p + \rho \boldsymbol{g} + \boldsymbol{j} \times \boldsymbol{B} \tag{2.1c}$$

where ρ is the plasma density, $\boldsymbol{v}$ the velocity, $\boldsymbol{j}$ is the current density, $\boldsymbol{E}$ and $\boldsymbol{B}$ are the electric and magnetic field respectively. When dealing with a static, low β plasma the velocity and gravity terms in equation (2.1c) can be neglected, and the (plasma) pressure force is small with respect to the Lorentz force $\boldsymbol{j} \times \boldsymbol{B}$. Thus equation (2.1c) reduces to

$$\boldsymbol{j} \times \boldsymbol{B} = 0\,. \tag{2.2}$$

Under these particular conditions there is no force acting on the plasma, and a magnetic field satisfying such equation is called a "force free field". The current density is expressed

by the electromagnetic field itself, rather than by the matter distribution, and result in each point of the space parallel to the magnetic field (or otherwise null). As a consequence the resulting system of equations is not linear any more.
Since we are interested in stationary configurations, the Ampére-Maxwell equation 2.1b simplifies to $\boldsymbol{\nabla} \times \boldsymbol{B} = (4\pi/c)\boldsymbol{j}$ and, using (2.2), the usual expression for the force-free equation is recovered

$$(\boldsymbol{\nabla} \times \boldsymbol{B}) \times \boldsymbol{B} = 0\,. \tag{2.3}$$

Alternatively, the previous condition could be expressed introducing a proportionality factor between the magnetic field and the current density

$$\boldsymbol{\nabla} \times \boldsymbol{B} = \alpha\, \boldsymbol{B} \tag{2.4}$$

where α is a scalar function of the coordinates $\alpha = \alpha(\boldsymbol{r})$. This expression for the force free condition together with $\boldsymbol{\nabla} \cdot \boldsymbol{B} = 0$ leads to

$$\boldsymbol{B} \cdot \boldsymbol{\nabla}\alpha = 0 \tag{2.5}$$

showing that the parameter α is constant along each field line.

The force free equation gives rise to potential, linear and non-linear fields, depending on α being respectively null, a constant or a generic function of the coordinates.

In order to obtain a general equations suitable for the subsequent applications to the magnetosphere around a neutron star, we consider here usual spherical coordinates (r, θ, ϕ), where the angles are defined as in fig. 2.1, though the problem is frequently analyzed in Cartesian or cylindrical coordinates as well.

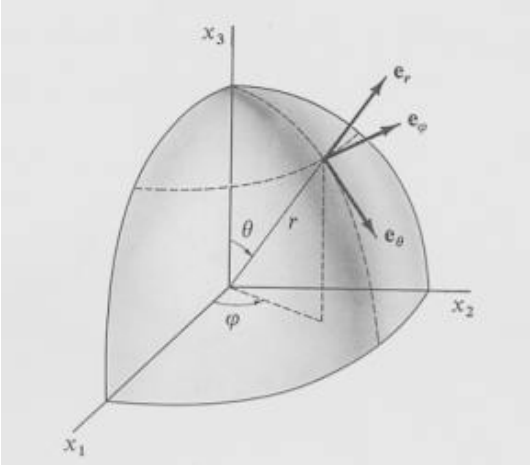

Figure 2.1: *Spherical coordinate system adopted here, in particular this plot illustrate the choice for θ, ϕ.*

2.1 Potential fields

In the case of null current, or equivalently for $\alpha \equiv 0$, the solution of equation 2.4 is a potential field. Such a magnetic field can be expressed in terms of the gradient of a (magnetic) scalar potential $\psi(r, \theta, \phi)$:

$$\boldsymbol{B} = -\boldsymbol{\nabla}\psi \tag{2.6}$$

Substituting this expression for the magnetic field into the force free condition, we obtain the Laplace equation

$$\boldsymbol{\nabla}^2\psi = 0 \tag{2.7}$$

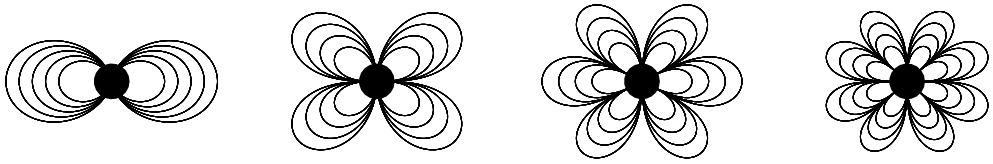

(a) *l=1 (dipole).* **(b)** *l=2 (quadrupole).* **(c)** *l=3 (octupole).* **(d)** *l=4.*

Figure 2.2: *Field lines of axially symmetric (m=0) potential multipoles. The order is indicated at bottom of each panel.*

from which the potential ψ, and thus the magnetic field itself, can be recovered.

Among potential fields a particular set of solutions are the multipolar fields, that can be expressed in terms either spherical harmonics in the more general (non-axisymmetric) case, or of Legendre polynomials, i.e. zonal harmonics, when dealing with axisymmetric fields (see figure 2.2).

The general form of the multipolar magnetic potential is (Bronzan [14])

$$\begin{aligned} \psi &= \sum_{l=1}^{\infty} \sum_{m=-l}^{l} \frac{4\pi}{2l+1} \frac{M_{l,m}}{r^{l+1}} Y_{l,m}(\theta,\phi) \\ M_{l,m} &= -\int \mathrm{d}^3x' \, Y^*_{l,m}(\theta',\phi') \cdot x'^l \frac{\boldsymbol{\nabla}' \cdot [x' \times \mathbf{J}(x')]}{(l+1)\, c} \end{aligned} \tag{2.8}$$

2.2 Linear fields

In the case of constant α it is possible to derive a general solution of the force free equation, as shown e.g. by Chandrasekhar & Kendall [23]. In this case, as in the previous one, solutions can be obtained for generic fields, without necessarily require axial symmetry. The fields obtained could be decomposed into a poloidal plus a toroidal vector field, and the most general solution is shown to be

$$\boldsymbol{B} = \frac{\boldsymbol{\nabla} \times (\boldsymbol{\nabla} \times \psi\, \hat{u})}{\alpha} + \boldsymbol{\nabla} \times (\psi\, \hat{u}) \tag{2.9}$$

where $\hat{u}$ is a generic unit vector and ψ a scalar function satisfying the Helmholtz equation

$$\boldsymbol{\nabla}^2 \psi + \alpha^2 \psi = 0\,. \tag{2.10}$$

In spherical coordinates, for later convenience, we choose $\hat{u} \equiv \hat{\boldsymbol{e}}_{\boldsymbol{\phi}}$. The equation is generally solved by separation of variables, and therefore lead to the introduction of two constants m, n. The solutions of order m and degree n then are

$$\psi_n^m = Z_n(\alpha r)\, P_n^m(\cos\theta)\, e^{im\phi} \tag{2.11}$$

where $Z_n(\alpha r)$ is a linear combination of the Bessel functions $J_{n+1/2},\ J_{-n-1/2}$ (Chandrasekhar & Kendall [23])

$$Z_n(\alpha r) = \left(\frac{\pi}{2\alpha r}\right)^{1/2} \left[J_{n+1/2}(\alpha r) + J_{-n-1/2}(\alpha r))\right]. \tag{2.12}$$

The global field is then decomposed as

$$\boldsymbol{B} = \sum_{n=0}^{\infty}\sum_{m=0}^{\infty} \lambda_{n,m}\, \boldsymbol{B}_{n,m} \tag{2.13}$$

with $\lambda_{n,m}$ complex constants, and each component $\boldsymbol{B}_{n,m}$ is obtained as prescribed in equation (2.9) from the corresponding potential ψ_n^m . Another feature of this fields, In the case of linear force free fields with spherical boundaries, the energy is stored equally in the poloidal and toroidal components.

The properties of linear force free fields have been studied also by Hudson & Wheatland [62] in comparison with other kinds of force free fields, obtained with the same boundary conditions. A major difficulty of the method used to solve the linear force free problem, is the recovery of the limiting case of vanishing α. The potential fields, indeed, can be obtained as a particular case of the more general force free fields, but not as a limit of $\alpha = \text{cost.} \to 0$.

2.3 Non-linear fields

The case of general α is the more difficult to solve, and there are no general methods to obtain such fields, unless in the presence of some symmetry. Nevertheless, non-linear fields are the more realistic ones, particularly in the case of large localized currents. Often the non-linear equation should be solved numerically, having no general solution.

2.3.1 Axisymmetric fields

As stated above, in the presence of symmetries, the solutions of the force free equation can be obtained analytically. In order to study symmetric fields, for later convenience, we choose the symmetric (polar) axis coincident with the z-axis. The case of interest is described by a field not depending on one coordinate variable (here either z in Cartesian coordinates or ϕ in spherical coordinates). The field can be obtained introducing a 2-D potential $\psi(r,\theta)$ and a general function $F(r,\theta)$ for the third component:

$$\begin{aligned}\boldsymbol{B} =& \frac{\boldsymbol{\nabla}\psi \times \hat{\boldsymbol{e}}_{\boldsymbol{\phi}} + F\,\hat{\boldsymbol{e}}_{\boldsymbol{\phi}}}{r\sin\theta} \\ =& \frac{1}{r\sin\theta}\left(\frac{1}{r}\frac{\partial\psi}{\partial\theta}\hat{\boldsymbol{e}}_{\boldsymbol{r}} - \frac{\partial\psi}{\partial r}\hat{\boldsymbol{e}}_{\boldsymbol{\theta}}\right) + \frac{F(r,\theta)}{r\sin\theta}\hat{\boldsymbol{e}}_{\boldsymbol{\phi}}\end{aligned} \tag{2.14}$$

where the factor $1/r\sin\theta$ is included only as a metric factor for the spherical coordinate system. By introducing this expression for the field into the force free equation, we obtain three

scalar equations (here and in the following $\mu \equiv \cos\theta$)

$$\frac{F}{\sin\theta}\frac{\partial F}{\partial r} + \left(\frac{\partial^2\psi}{\partial r^2} + \frac{\sin^2\theta}{r^2}\frac{\partial^2\psi}{\partial\mu^2}\right)\frac{\partial\psi}{\partial r} = 0 \tag{2.15a}$$

$$\left(\frac{\partial^2\psi}{\partial r^2} + \frac{\sin^2\theta}{r^2}\frac{\partial^2\psi}{\partial\mu^2}\right)\frac{\partial\psi}{\partial\mu} + \frac{F}{\sin\theta}\frac{\partial F}{\partial\mu} = 0 \tag{2.15b}$$

$$\frac{\partial\psi}{\partial r}\frac{\partial F}{\partial\mu} - \frac{\partial\psi}{\partial\mu}\frac{\partial F}{\partial r} = 0 \tag{2.15c}$$

If F is a function only of ψ, equation (2.15c) is automatically satisfied, while the first two equations (2.15) are not linearly independent, and combined together lead to the Grad-Schlüter-Shafranov (GSS) equation[1] (Choudhuri [25])

$$\frac{\partial^2\psi}{\partial r^2} + \frac{\sin^2\theta}{r^2}\frac{\partial^2\psi}{\partial\mu^2} + F(\psi)\frac{\mathrm{d}F}{\mathrm{d}\psi} = 0\,. \tag{2.16}$$

Solutions of these equation can be obtain numerically. By choosing an appropriate form for ψ and $F(\psi)$ it is possible to rearrange the GSS equation, obtaining a simpler or more easily tractable equation. Often in this case the solutions are obtained analytically as, for example, in the magnetosphere description of § 3.2.

2.3.2 Non-axisymmetric fields

As shown above, the solution of the non-linear force-free equation is relatively simple and extensively studied in the case of a field not depending on one of the coordinate variables. In the more general case, though, the situation is quite different. Nevertheless some general solution for non-linear non-axisymmetric fields could be find. Here we discuss two approaches, the first introduced by Cuperman & Ditkowski [26] and the other, more general, by Uchida [120, 121, 122]. In the first case a force free field is obtained analytically by exploiting the relation between $\boldsymbol{\nabla}\alpha$ and the magnetic field $\boldsymbol{B}$ and working in a suitable (curvilinear) coordinate system. The second method, instead, is based on a tensorial description of the electromagnetic field in terms of two scalar potentials, the "Euler potentials".

2.3.2.1 Cuperman & Ditkowski's method

The method is based, rather than on the construction of new solutions of equation (2.3), on the definition of a new coordinate system (u_i, i=1-3), in which the magnetic field depends only on two coordinates, thus leading again to the axisymmetric case. Once a solution is found in this new coordinates, the field in the original coordinate system can be recovered.

It is always possible to define a (curvilinear) coordinate system (u_i) with one variable along the direction of $\boldsymbol{\nabla}\alpha$ and the others chosen in order to have an orthogonal clockwise system. From relation 2.5 follows that the gradient of α is locally perpendicular to the magnetic field, thus with the change of coordinates ($x_i \rightarrow u_i,\ i = 1-3$) the two quantities, that

[1] also known as the pulsar equation and here written for a non-rotating star

in the older system depended on all the three coordinate variables, become

$$\alpha = \alpha(u_1) \tag{2.17a}$$

$$\boldsymbol{B} = \boldsymbol{B}(u_2, u_3)\,. \tag{2.17b}$$

We recall here some basic definitions that will be used later. Let us write the position of a point $P(x, y, z)$, in terms of some orthogonal curvilinear coordinates (u_1, u_2, u_3),

$$\boldsymbol{r} = x(u_1, u_2, u_3)\hat{\boldsymbol{e}}_{\boldsymbol{x}} + y(u_1, u_2, u_3)\hat{\boldsymbol{e}}_{\boldsymbol{y}} + z(u_1, u_2, u_3)\hat{\boldsymbol{e}}_{\boldsymbol{z}}\,. \tag{2.18}$$

The scaling factor of the coordinate system (u_i) are defined as:

$$h_i = \left| \frac{\partial \boldsymbol{r}}{\partial u_i} \right| \qquad i = 1 - 3\,. \tag{2.19}$$

The gradient operator applied to a scalar function $\alpha(u_1, u_2, u_3)$ is simply

$$\boldsymbol{\nabla}\alpha = \sum_{i=1}^{3} \frac{1}{h_i}\frac{\partial \alpha}{\partial u_i}\hat{\boldsymbol{e}}_{\boldsymbol{u_i}} \tag{2.20}$$

and the divergence and curl operators, applied to a vector
$\boldsymbol{f}(u_1, u_2, u_3) = (f_1\hat{\boldsymbol{e}}_{\boldsymbol{u_1}} + f_2\hat{\boldsymbol{e}}_{\boldsymbol{u_2}} + f_3\hat{\boldsymbol{e}}_{\boldsymbol{u_3}})$, are

$$\boldsymbol{\nabla}\cdot\boldsymbol{f} = \frac{1}{h_1h_2h_3}\left[\frac{\partial}{\partial u_1}(h_2h_3f_1) + \frac{\partial}{\partial u_2}(h_1h_3f_2) + \frac{\partial}{\partial u_3}(h_1h_2f_3)\right] \tag{2.21a}$$

$$\boldsymbol{\nabla}\times\boldsymbol{f} = \frac{1}{h_1h_2h_3}\begin{vmatrix} h_1\hat{\boldsymbol{e}}_{\boldsymbol{u_1}} & h_2\hat{\boldsymbol{e}}_{\boldsymbol{u_2}} & h_3\hat{\boldsymbol{e}}_{\boldsymbol{u_3}} \\ \frac{\partial}{\partial u_1} & \frac{\partial}{\partial u_2} & \frac{\partial}{\partial u_3} \\ h_1f_1 & h_2f_2 & h_3f_3 \end{vmatrix}\,. \tag{2.21b}$$

The governing equations for the field components $(B_2,\ B_3)$ are obtained from the solenoidal condition $\boldsymbol{\nabla}\cdot\boldsymbol{B} = 0$ together with the force-free equation (2.4), and are

$$\frac{\partial}{\partial u_2}(h_1h_3B_2) + \frac{\partial}{\partial u_3}(h_1h_2B_3) = 0 \tag{2.22a}$$

$$\frac{\partial}{\partial u_2}(h_3B_3) - \frac{\partial}{\partial u_3}(h_2B_2) = 0 \tag{2.22b}$$

$$-\frac{1}{h_1h_3}\frac{\partial}{\partial u_1}(h_3B_3) = \alpha B_2 \tag{2.22c}$$

$$\frac{1}{h_1h_2}\frac{\partial}{\partial u_1}(h_2B_2) = \alpha B_3\,. \tag{2.22d}$$

Equations (2.22a,b) contain terms in $u_2,\ u_3$ only, while equations (2.22c,d) depend only on u_1. Thus, it is possible to solve separately the two sets obtaining the dependence of the field on the different coordinates. The final dependence on all the three variables is obtained by combining together the two sets of solutions, as it is shown in the following example.

In order to illustrate the model, we consider (Cuperman & Ditkowski [26]) the case of $\alpha = \alpha(r)$, i.e.

$$\frac{\boldsymbol{\nabla}\alpha}{|\nabla\alpha|} = \hat{\boldsymbol{e}}_{\boldsymbol{r}}. \tag{2.23}$$

in usual spherical coordinates (r, θ, ϕ).
Scaling factors for this system of coordinates are $h_1 = 1,\ h_2 = r,\ h_3 = r\sin\theta$.
The magnetic field, that in Cartesian coordinates depends on all the three variables, once expressed in spherical coordinates is

$$\boldsymbol{B} = B_\theta \hat{\boldsymbol{e}}_{\boldsymbol{\theta}} + B_\phi \hat{\boldsymbol{e}}_{\boldsymbol{\phi}} \tag{2.24}$$

and lies on spherical surfaces of constant r. Once assumed a form for α, our task is to determine the expressions for B_θ, B_ϕ.
Defining the new quantities

$$\beta_2 = h_2 B_2 = r B_\theta \tag{2.25a}$$
$$\beta_3 = h_3 B_3 = r\sin\theta B_\phi \tag{2.25b}$$

equations (2.22) in this case become

$$\frac{\partial}{\partial\theta}(\sin\theta\beta_2) + \frac{\partial}{\partial\phi}(\frac{1}{\sin\theta}\beta_3) = 0 \tag{2.26a}$$
$$\frac{\partial\beta_3}{\partial\theta} - \frac{\partial\beta_2}{\partial\phi} = 0 \tag{2.26b}$$

$$-\frac{1}{\alpha\sin\theta}\frac{\partial\beta_3}{\partial r} = \beta_2 \tag{2.27a}$$
$$\frac{\sin\theta}{\alpha}\frac{\partial\beta_2}{\partial r} = \beta_3 \tag{2.27b}$$

Solving equations (2.26) we find the dependence of the field $\beta_{2,3} = \tilde{\beta}_{2,3}(\theta, \phi)$, while from equations (2.27) we obtain the radial dependence $\beta_{2,3} = \hat{\beta}_{2,3}(r)$.
In this last case the solutions should be in the form

$$\hat{\beta}_2 = b_1\cos Z + b_2\sin Z; \quad \hat{\beta}_3 = \sin\theta(b_2\cos Z - b_1\sin Z) \tag{2.28}$$

where function $Z(r)$ is defined by the relation $\alpha = \partial Z/\partial r$.

The entire dependence of the field is obtained, e.g., considering solutions of the kind

$$\beta_{2,3}(r, \theta\phi) = \hat{\beta}_{2,3}(r)\cdot g(\theta, \phi) \tag{2.29}$$

and inserting these expression in the two equations (2.26) to find the form of the unknown

function $g(\theta, \phi)$. The equations to be solved now read

$$\begin{aligned} \frac{\partial}{\partial\theta}\left[\sin\theta g(b_1\cos Z + b_2\sin Z)\right] + \frac{\partial}{\partial\phi}\left[g(b_2\cos Z - b_1\sin Z)\right] = 0 \\ \frac{\partial}{\partial\theta}\left[\sin\theta g(b_2\cos Z - b_1\sin Z)\right] - \frac{\partial}{\partial\phi}\left[g(b_1\cos Z + b_2\sin Z)\right] = 0\,. \end{aligned} \tag{2.30}$$

The parameters b_1, b_2 must not depend on the radial coordinate, but in general these are functions of (θ, ϕ). Equating the coefficients of $\cos Z$ and $\sin Z$ in equations (2.30), result

$$\begin{aligned} \frac{\partial}{\partial\theta}(b_1\sin\theta) + \frac{\partial b_2}{\partial\phi} = 0 \\ \frac{\partial}{\partial\theta}(b_2\sin\theta) - \frac{\partial b_1}{\partial\phi} = 0\,. \end{aligned} \tag{2.31}$$

From this second expression, it follows that b_1 and $b_2\sin\theta$ must be expressed in terms of the same function $F(\theta, \phi)$

$$b_1 = \frac{\partial F}{\partial\theta}; \quad b_2 = \frac{1}{\sin\theta}\frac{\partial F}{\partial\phi} \tag{2.32}$$

thus substituting these expressions in equation (2.26a), we obtain

$$\sin^2\theta\frac{\partial^2 F}{\partial\theta^2} + \sin\theta\cos\theta\frac{\partial F}{\partial\theta} + \frac{\partial^2 F}{\partial\phi^2} = 0\,. \tag{2.33}$$

With the substitution $\eta = -\ln(\tan\theta/2)$ this can be transformed into Laplace equation

$$\frac{\partial^2 F}{\partial\eta^2} + \frac{\partial^2 F}{\partial\phi^2} = 0 \tag{2.34}$$

and solved by separation of variables, introducing the parameter n

$$\frac{\partial^2 F}{\partial\eta^2} = n^2 = -\frac{\partial^2 F}{\partial\phi^2}\,. \tag{2.35}$$

The solution then depends on this parameter and is

$$F_n(\theta, \phi) = (a_{n1}\cos n\phi + a_{n2}\sin n\phi)(a_{n3}\cot^n\theta/2 + a_{n4}\tan^n\theta/2)\,. \tag{2.36}$$

Finally we obtain the coefficients $b_{1,2}$ in terms of the parameter n

$$\begin{aligned} b_{n1} = \frac{n}{\sin\theta}(a_{n1}\cos n\phi + a_{n2}\sin n\phi)(-a_{n3}\cot^n\theta/2 + a_{n4}\tan^n\theta/2) \\ b_{n2} = \frac{n}{\sin\theta}(-a_{n1}\sin n\phi + a_{n2}\cos n\phi)(a_{n3}\cot^n\theta/2 + a_{n4}\tan^n\theta/2) \end{aligned} \tag{2.37}$$

and the global dependence on the field is recovered

$$B_\theta = \frac{1}{r\ \sin\theta}\Bigg\{\Big[a_0 + \sum_{n=1}^{\infty} n(a_{n1}\cos n\phi + a_{n2}\sin n\phi)\cdot \\ (-a_{n3}\cot^n\theta/2 + a_{n4}\tan^n\theta/2)\Big]\cos Z + \\ + \Big[\sum_{n=1}^{\infty} n(-a_{n1}\sin n\phi + a_{n2}\cos n\phi)\cdot \\ (a_{n3}\cot^n\theta/2 + a_{n4}\tan^n\theta/2)\Big]\sin Z\Bigg\} \quad (2.38a)$$

$$B_\phi = \frac{1}{r\ \sin\theta}\Bigg\{\Big[a_0 + \sum_{n=1}^{\infty} n(-a_{n1}\sin n\phi + a_{n2}\cos n\phi)\cdot \\ (a_{n3}\cot^n\theta/2 + a_{n4}\tan^n\theta/2)\Big]\cos Z + \\ - \Big[a_0 + \sum_{n=1}^{\infty} n(a_{n1}\cos n\phi + a_{n2}\sin n\phi)\cdot \\ (-a_{n3}\cot^n\theta/2 + a_{n4}\tan^n\theta/2)\Big]\sin Z\Bigg\} \quad (2.38b)$$

All a_0, a_{ni} are arbitrary constants, determined by the form of the function F and the boundary conditions. The case of $a_{ni} \equiv 0$ lead to the axisymmetric field and is equivalent to the condition of $b_{1,2}$ not depending on (θ, ϕ).

More insights and examples are presented in Cuperman & Ditkowski [26], but we will not use this method to derive magnetars fields because it requires to know a priori the function $\alpha = \alpha(\boldsymbol{r})$ (or the function F). As we will see later, in the case of the magnetars this function has to be determined together with the field.

2.3.2.2 Uchida's method

This approach is useful to find both classical and relativistic solutions of the force free equation. Relativistic analysis is mainly used to study magnetospheres around black holes, neutron stars and in accretion disks. Here, though, we will use it to derive non -axisymmetric solutions in classical framework.
Introducing the electromagnetic tensor field $F_{\mu\nu}$ and the four-current J^μ, the set of equation that must be solved in order to find a force free field are the Maxwell equations (here $c = G = 1$, and ∇_μ denote derivation with respect to μ)

$$\begin{aligned} &\nabla_\lambda F_{\mu\nu} + \nabla_\mu F_{\nu\lambda} + \nabla_\nu F_{\lambda\mu} = 0 \\ &\nabla_\mu F^{\lambda\mu} = 4\pi J^\lambda \end{aligned} \quad (2.39)$$

together with the force free condition, that in this case become

$$F_{\mu\nu}J^{\nu} = 0 \tag{2.40}$$

Because of the last equation, necessarily we are dealing with a degenerate field, for which the electromagnetic tensor satisfy det$F_{\mu\nu} = 0$, i.e. $\boldsymbol{E}\cdot\boldsymbol{B} = 0$

As stated in Uchida [120], any degenerate field could be expressed in terms of two scalar functions $\psi_{1,2}(r,\theta,\phi)$, the Euler potentials[2]

$$F_{\mu\nu} = \partial_\mu\psi_1\,\partial_\nu\psi_2 - \partial_\mu\psi_2\,\partial_\nu\psi_1\,. \tag{2.41}$$

The basic equations of the force free field, involving the two unknown potentials, are obtained introducing this last expression for the field $F_{\mu\nu}$ into equations (2.39) and (2.40), and result in two nonlinear equations

$$\begin{aligned}\partial_\nu\psi_1\,\partial_\lambda\{\sqrt{-g}(\partial^\nu\psi_1\partial^\lambda\psi_2 - \partial^\nu\psi_2\partial^\lambda\psi_1)\} = 0\\ \partial_\nu\psi_2\,\partial_\lambda\{\sqrt{-g}(\partial^\nu\psi_1\partial^\lambda\psi_2 - \partial^\nu\psi_2\partial^\lambda\psi_1)\} = 0\end{aligned} \tag{2.42}$$

where g is the metric determinant.

As here we are interested only on a classical description of the magnetic field, we can express the fields in terms of the classical Euler potentials (from which the 4-potentials are derived)

$$\begin{aligned}\boldsymbol{B} &= \boldsymbol{\nabla}\psi_1\times\boldsymbol{\nabla}\psi_2\\ \boldsymbol{E} &= -\partial_t\psi_1\boldsymbol{\nabla}\psi_2 + \partial_t\psi_2\boldsymbol{\nabla}\psi_1\,.\end{aligned} \tag{2.43}$$

and we can simplify the equations considering expressions (4.11) in Uchida [122]

$$\nabla\psi_i\cdot\nabla\times[(1-r^2\sin^2\theta\,\Omega^2)\boldsymbol{B} + r^2\sin^2\theta\,\Omega^2 B_\phi\hat{\boldsymbol{e}}_{\boldsymbol{\phi}}] = 0 \quad \text{for i=1,2} \tag{2.44}$$

for a star with rotational velocity Ω.

In order to illustrate the method, we derive the equations for the case of a time-independent axisymmetric field and show how the Grad-Schlüter-Shafranov equation can be recovered.

Choosing for the potentials the form

$$\psi_1 = \mathscr{P}(r,\theta);\quad \psi_2 = \phi + \eta(r,\theta) \tag{2.45}$$

where ϕ is the azimuthal angle and $\mathscr{P},\eta$ are two generic functions, the magnetic field can be obtained as

$$\begin{aligned}\boldsymbol{B} =&\boldsymbol{\nabla}\psi_1\times\boldsymbol{\nabla}\psi_2 = \frac{\boldsymbol{\nabla}\mathscr{P}\times\hat{\boldsymbol{e}}_{\boldsymbol{\phi}}}{r\sin\theta} + \boldsymbol{\nabla}\mathscr{P}\times\boldsymbol{\nabla}\eta =\\ =&\frac{1}{r\sin\theta}\left(\frac{1}{r}\frac{\partial\mathscr{P}}{\partial\theta}\hat{\boldsymbol{e}}_{\boldsymbol{r}} - \frac{\partial\mathscr{P}}{\partial r}\hat{\boldsymbol{e}}_{\boldsymbol{\theta}}\right) + \frac{1}{r}\left(\frac{\partial\mathscr{P}}{\partial r}\frac{\partial\eta}{\partial\theta} - \frac{\partial\mathscr{P}}{\partial\theta}\frac{\partial\eta}{\partial r}\right)\hat{\boldsymbol{e}}_{\boldsymbol{\phi}}\end{aligned} \tag{2.46}$$

[2]The Euler potentials are also referred to as Clebsch variables

in terms of a poloidal ($\boldsymbol{\nabla}\mathscr{P} \times \hat{\boldsymbol{e}}_{\boldsymbol{\phi}}$) and a toroidal component ($\boldsymbol{\nabla}\mathscr{P} \times \boldsymbol{\nabla}\eta$). The third component of the field can be denoted as $F(r, \theta)$ and, as previously done in § 2.3.1, from the three scalar equations we derive two independent equations in the unknown quantities $\mathscr{P}, F(\mathscr{P})$. The equations to be solved derives from equations (2.44) with $\Omega = 0$ and are

$$\begin{aligned} \boldsymbol{\nabla}\psi_1 \cdot \boldsymbol{\nabla} \times \boldsymbol{B} &= 0 \\ \boldsymbol{\nabla}\psi_2 \cdot \boldsymbol{\nabla} \times \boldsymbol{B} &= 0 \, . \end{aligned} \tag{2.47}$$

These equations lead to equation (5.14) in Uchida [122]

$$\nabla \cdot \left[(1 - r^2 \sin^2\theta \Omega^2) \frac{\nabla \mathscr{P}}{r^2 \sin^2\theta} \right] + \frac{B_\phi}{r \sin\theta} \frac{\mathrm{d}B_\phi}{\mathrm{d}\mathscr{P}} + \Omega \frac{\mathrm{d}\Omega}{\mathrm{d}\mathscr{P}} |\nabla \mathscr{P}|^2 = 0 \, . \tag{2.48}$$

This, in the case $\Omega = 0$, is equivalent to the GSS equation.

Different field topologies are constructed choosing different forms of the Euler potentials, and in the general case, the system of equations to be solved can be obtained from the force free condition (2.3). As in the previous cases, only two of the three scalar equations are linear independent, and generally must be solved together.

Chapter 3

Topology of magnetars external field. Axially symmetric fields

In this Chapter, adapted from Pavan et al. [97], external fields around magnetars are described. The magnetospheres of these objects deeply interact with the thermal radiation emitted by the source, leaving a trace of their topology in the collected spectra. Following the model of Thompson, Lyutikov & Kulkarni, all the fields considered here are symmetric about the magnetic axis.

3.1 Introduction

There is an increasing theoretical and observational evidence that the external magnetic field of magnetars may contain a toroidal component, likely of the same order of the poloidal one. Such "twisted magnetospheres" are threaded by currents flowing along the closed field lines which can efficiently interact with soft thermal photons via resonant cyclotron scatterings (RCS). Actually, RCS spectral models proved quite successful in explaining the persistent $\sim$ 1–10 keV emission from the magnetar candidates, the soft γ-ray repeaters (SGRs) and the anomalous X-ray pulsars (AXPs). Moreover, it has been proposed that, in presence of highly relativistic electrons, the same process can give rise to the observed hard X-ray spectral tails extending up to ~ 200 keV.

Spectral calculations have been restricted up to now to the case of a globally twisted dipolar magnetosphere, although there are indications that the twist may be confined only to a portion of the magnetosphere, and/or that the large scale field is more complex than a simple dipole. In this chapter we investigate multipolar, force-free magnetospheres of ultra-magnetized neutron stars. We first discuss a general method to generate multipolar solutions of the Grad-Schlüter-Shafranov equation, and analyze in detail dipolar, quadrupolar and octupolar fields. The spectra and lightcurves for these multipolar, globally twisted fields are then computed using a Monte Carlo code and compared with those of a purely dipolar configuration. Finally the phase-resolved spectra and energy-dependent lightcurves obtained with a simple model of a locally sheared field are confronted with the *INTEGRAL*

observations of the AXPs 1RXS J1708-4009 and 4U 0142+61. Results support a picture in which the field in these two sources is not globally twisted.

We will discuss how globally twisted magnetostatic equilibria can be derived in the case of higher order, axially symmetric multipolar fields. In particular, explicit (numerical) solutions for quadrupolar and octupolar fields are presented. We use the Monte Carlo code developed by Nobili, Turolla & Zane [93] to investigate the properties of the emerging spectrum and pulse profiles for higher order multipolar fields.

3.2 Globally-twisted axisymmetric models

A feature of (non-potential) force-free fields is the presence of supporting currents. As first suggested by Thompson et al. [116], thermal photons emitted by the star surface can scatter at the cyclotron resonance on the charges flowing in the magnetosphere, and this can drastically alter the primary spectrum. Recent, detailed calculations [76, 43, 93] of scattering onto mildly relativistic electrons confirmed this picture. Typical synthetic spectra exhibit a high-energy tail, superimposed to a thermal bump and closely resemble the (empirical) "blackbody+power-law" model which has been routinely used to describe the magnetars quiescent emission in the ~ 0.5–10 keV band [see again 129, 83, for a summary of observational results]. This model has been successfully applied to the X-ray spectra of several AXPs/SGRs by [103, see also], providing direct support to the twisted magnetosphere scenario.

In this section we present the basic equations that we use to derive globally-twisted magnetospheric models. We follow closely the approach outlined in Wolfson [127] and Thompson et al. [116] (hereafter W95 and TLK, respectively), who considered the global twist of a dipolar field. As we show below, the same approach can be used to compute twisted fields for multipoles of arbitrary order. As in W95 and TLK, we restrict to magnetostatic, force-free equilibria.

In the magnetar scenario the shear of the field modify the cross-section and the optical-depth to resonant scattering (Thompson et al. [116]). Any sheared field, hence, produce different spectra and light curves from the object. Not only the amount of shear, but the topology too, modify the radiation reaching the observer. Some complicated pulse profile from SGRs has already been explained with the presence of higher multipoles (e.g. Thompson & Duncan [115], Feroci et al. [44], Page & Sarmiento [95]). Moreover other recent data both for AXPs and SGRs seem to point toward the idea of a localized, rather than global, twist (e.g. Woods et al. [130], Perna & Gotthelf [98])

Our aim is to construct an axisymmetric, force-free field by adding a defined amount of shear to a potential field. In accordance with both TLK and W95, we choose to use the flux function $\mathscr{P}$ to express the poloidal component of the field. Axisymmetry is enforced choosing a function independent of the azimuth ϕ (we use a spherical coordinate system with the polar axis along the magnetic moment vector). Thus, the general expression for an

axisymmetric field is:

$$\boldsymbol{B} = \frac{\boldsymbol{\nabla}\mathscr{P}(r,\theta)\times\hat{\boldsymbol{e}}_{\boldsymbol{\phi}}}{r\sin\theta} + B_\phi(r,\theta)\hat{\boldsymbol{e}}_{\boldsymbol{\phi}}. \tag{3.1}$$

where $\hat{\boldsymbol{e}}_{\boldsymbol{\phi}}$ is the unit vector in the ϕ direction.

By inserting the previous expression into the force-free condition (equation [2.3]) one obtains two independent scalar equations for the flux function, $\mathscr{P}$, and the toroidal component of the field, B_ϕ. The former requires B_ϕ to be a function of $\mathscr{P}$ only [74], thus we can write

$$B_\phi(r,\theta) = \frac{1}{r\sin\theta}F(\mathscr{P}) \tag{3.2}$$

where F is an arbitrary function. Introducing the previous expression into the second scalar equation leads to the Grad-Schlüter-Shafranov (GSS) equation

$$\frac{\partial^2\mathscr{P}}{\partial r^2} + \frac{1-\mu^2}{r^2}\frac{\partial^2\mathscr{P}}{\partial\mu^2} + F(\mathscr{P})\frac{\mathrm{d}F}{\mathrm{d}\mathscr{P}} = 0 \tag{3.3}$$

(here and in the following $\mu \equiv \cos\theta$).

The GSS equation can be reduced to an ordinary differential equation by making suitable assumptions on the dependence of $\mathscr{P}$ on the coordinates. Following a classical approach to this problem [e.g. 74, W95, TLK], we assume separation of variables and choose the flux function $\mathscr{P}$ in the form

$$\mathscr{P} = \mathscr{P}_0\left(\frac{r}{R_{NS}}\right)^{-p} f(\mu) \tag{3.4}$$

where $f(\mu)$ is a function of the colatitude θ, R_{NS} is the stellar radius and $\mathscr{P}_0 = B_{\rm pole}R_{NS}^2/2$, as in TLK. The requirement that all the components of $\boldsymbol{B}$ have the same radial dependence implies that

$$F(\mathscr{P}) = \sqrt{\frac{C}{p(1+p)}}\,\mathscr{P}^{1+1/p} \tag{3.5}$$

where, for later convenience, we have expressed the multiplicative constant in terms of a parameter C and of the radial exponent p. Recalling equation (4.23), one can explicitly write the magnetic field as a function of f

$$\boldsymbol{B} = \frac{B_{pole}}{2}\left(\frac{r}{R_{NS}}\right)^{-p-2}\left[-f', \frac{pf}{\sin\theta}, \sqrt{\frac{C\,p}{p+1}}\frac{f^{1+1/p}}{\sin\theta}\right] \tag{3.6}$$

where a prime denotes derivation with respect to μ. Finally, taking into account equations (3.4) and (3.5), the GSS equation becomes for the case at hand

$$(1-\mu^2)f'' + p\,(p+1)f + Cf^{1+2/p} = 0 \tag{3.7}$$

which is a second order ordinary differential equation for the angular part of the flux function. Its solution, once a suitable set of boundary conditions has been supplied (see § 3.2.1), completely specifies the external magnetic field.

Besides controlling the radial decay, the parameter p also fixes the amount of shear of the field. In fact, recalling the definition of shear angle (W95, TLK)

$$\begin{aligned}\Delta\phi_{NS} &= \int_{\text{field line}} \frac{B_\phi}{(1-\mu^2)B_\theta}\mathrm{d}\mu \\ &= \left[\frac{C}{p\,(1+p)}\right]^{1/2} \int_{\text{field line}} \frac{f^{1/p}}{1-\mu^2}\mathrm{d}\mu\,,\end{aligned} \tag{3.8}$$

it is immediate to see that different values of p correspond to fields with different shear. Actually, as it will be discussed later on, the effect of decreasing p is to increase B_ϕ with respect to the other components, and consequently to increase the shear.

As it is apparent from equation (3.6), the limiting case $p \to 0$ results in a purely radial field whose field lines are directed either outwards or inwards (whence the name of split monopole). The directions of the field lines divide the sphere (i.e. the star) into several zones, and we can imagine field lines of opposite directions connecting at radial infinity (W95). Split monopole fields obtained for different multipolar orders differ from one another in the number of zones into which the sphere is split.

3.2.1 Boundary conditions

In order to solve equation (3.7) we need to provide a suitable set of boundary conditions. For a dipolar field there are just two poles and the star is divided into two hemispheres, i.e. the portions of the surface $0 \leq \theta \leq \pi/2$, $\pi/2 \leq \theta \leq \pi$, respectively, and $0 \leq \phi \leq 2\pi$. Higher order multipoles have in addition degenerate poles, which are loci of constant colatitude, and correspond to circles on the surface (see Fig. 3.1). For the quadrupole, for example, there are two poles on the magnetic axis and the equator is a degenerate pole. In the case of a generic multipolar field, the magnetic hemispheres of the dipole are replaced by a number of regions, each limited by two consecutive values of the colatitude, θ_i, θ_{i+1}, for which the field is purely radial (the pole) and has vanishing radial component (the magnetic "equator"), i.e. $B_\theta(\theta_i) = 0$ and $B_r(\theta_{i+1}) = 0$. We refer to these zones as to regions of unipolar B_r.

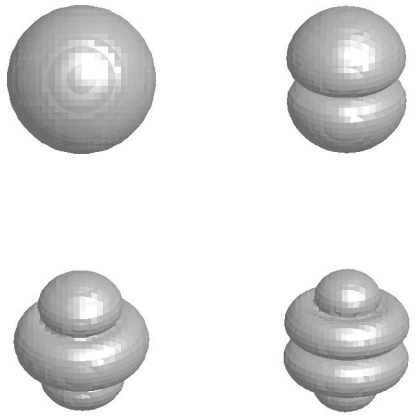

Figure 3.1: *Zonal harmonics are used to visualize multipolar field topologies. From top left to bottom right: multipoles with order from one to four. The positions of the degenerate poles are evident.*

Because of the north-south symmetry of unsheared multipolar fields, which is assumed to hold also for their twisted counterparts, the integration domain is restricted to $0 \leq \mu \leq 1$. In analogy with the "composite magnetic fields" of Low & Lou [74], integration is performed

piecewise, going from one pole to the next one. In each interval, the boundary conditions for equation (3.7) are determined by the requirements that: i) $\boldsymbol{B}$ is purely radial at each pole, and ii) the intensity is not modified by the shear. The latter condition can be enforced either by assigning the field strength at one pole, or the magnetic flux out of each region of unipolar B_r; in both cases the value must not change with the shear. For multipoles of odd order (dipole, octupole, ...) the first sub-domain starts at the geometrical equator, $\mu = 0$, which is not a pole. In these cases the boundary condition at $\mu = 0$ reflects the N-S symmetry of the field and translates into $f'(0) = 0$ (TLK).

The magnetic field in the entire interval ($0 \leq \mu \leq 1$) is then obtained by assembling the solutions computed in the various sub-domains with the same value of p, to ensure that the radial dependence of $\boldsymbol{B}$ is the same at all co-latitudes. Since the GSS equation is a second order ODE, imposing three boundary conditions implies that the parameter C is an eigenvalue of the problem and depends on the radial index p, $C = C(p)$. Each multipolar potential term satisfies the GSS equation with $C = 0$ and is associated to an integer radial index p_0; it is $p_0 = 1$ for the dipole, $p_0 = 2$ for the quadrupole and so on. In this particular case, the equation is linear and admits analytical solutions of the form (W95)

$$f_{p_0}(\mu) \propto \sqrt{1-\mu^2}\, P^1_{p_0}(\mu), \tag{3.9}$$

where $P^1_p(\mu)$ is the associated Legendre function of the first kind Abramowitz & Stegun, 1972 [1]).

Having established a set of boundary conditions, the GSS equation can be solved for different values of p, building a sequence of models characterized by a varying shear. As shown by Low & Lou [74], such a sequence share the same topology, i.e. the same number and position of poles. The only permitted values of the radial index are $p \leq p_0$.

3.2.2 Dipolar fields

The generating function of a pure dipole is

$$f_{p_0=1} = 1 - \mu^2, \tag{3.10}$$

thus from equation (3.6) it follows that the condition at the pole $\mu = 1$ is $f(1) = 0$, to which the symmetry condition $f'(0) = 0$ must be added. The third condition is set either specifying the field strength at one pole, $f'(1) = 1$ (as in TLK), or requiring a constant flux, $f(0) = 1$ (W95). The sequence of sheared dipoles has radial index $0 \leq p \leq 1$.

Sheared dipole fields have been discussed by W95 and TLK. These investigations, however, used a different boundary condition (see above) and we verified that the numerical solution of equation (3.7) produces quite different results for $f(\mu;\, p)$ and even more diverse eigenvalues $C(p)$ in the two cases (see Fig. 3.2). Still, one expects the magnetic field to be the same in both cases, since the two boundary conditions are physically equivalent. Actually, a direct comparison of the numerical solutions shows that $f_{TLK}/f_{W95} \simeq f'_{TLK}/f'_{W95} \simeq \mathrm{constant}$ for each p. Denoting by $\lambda(p)$ this constant ratio, one can write the expression of the

p	C_{TLK}	C_{W95}	λ
0.97	0.13	0.11	1.02
0.89	0.41	0.45	1.06
0.82	0.63	0.79	1.10
0.74	0.78	1.14	1.15
0.67	0.86	1.51	1.21
0.59	0.86	1.91	1.26
0.52	0.79	2.35	1.33
0.45	0.64	2.87	1.39
0.38	0.43	3.52	1.47
0.30	0.22	4.41	1.56
0.22	0.06	5.80	1.65
0.15	3.9×10^{-3}	8.52	1.75
0.07	4.3×10^{-7}	17.48	1.88
0.02	1.55×10^{-25}	89.78	1.97

Table 3.1: *The eigenvalues $C(p)$ for the two different sets of boundary conditions and the ratio $\lambda = f_{TLK}/f_{W95}$ for $0 < p < 1$.*

field in the two cases using equation (3.6)

$$\begin{aligned} \boldsymbol{B}_{W95} &\propto \left[-f', \frac{p}{\sin\theta} f, \left(C_{W95}\, \frac{p}{p+1} \right)^{1/2} \frac{f^{1+1/p}}{\sin\theta} \right] \\ \boldsymbol{B}_{TLK} &\propto \left[-\lambda f', \lambda \frac{p}{\sin\theta} f, \left(C_{TLK}\, \frac{p}{p+1} \right)^{1/2} \frac{(\lambda\, f)^{1+1/p}}{\sin\theta} \right] \end{aligned} \tag{3.11}$$

where the radial dependence has been omitted. The two fields have the same topology if and only if

$$\lambda^{1+1/p}\, \sqrt{C_{TLK}} = \lambda\, \sqrt{C_{W95}}. \tag{3.12}$$

We checked that the previous condition is indeed satisfied by our numerical solutions with a relative accuracy $\sim$ 2% for nearly all values of p [1]. The eingevalues and the ratio λ for different values of p are reported in table 3.1.

The magnetic field, then, has the same topology in both cases, and the two solutions differ only for a multiplicative factor (which changes with p); i.e., it is $\boldsymbol{B}_{TLK} = \lambda \boldsymbol{B}_{W95}$, with $1 \leq \lambda \leq 2$. The great diversity in the eigenvalues, especially for $p \to 0$ is in fact balanced by the different behavior of the function $f(\mu)$. While for constant B_{pole}, it is $1 \leq \max f \leq 2$, in the case of constant flux $\max f = 1$ for any p. In the limit $p \to 0$ the proportionality of the two solutions for f can be recovered analytically. In fact, it can be shown that in the split-monopole limit the generating functions are

$$\begin{aligned} f(\mu) &= 1 - |\mu| \qquad \text{for constant flux} \\ f(\mu) &= 2\,(1 - |\mu|) \qquad \text{for constant } B_{\text{pole}} \end{aligned} \tag{3.13}$$

[1] The error becomes larger for $p \sim p_0$ because $\lambda\, \sqrt{C_{W95}} \to 0$

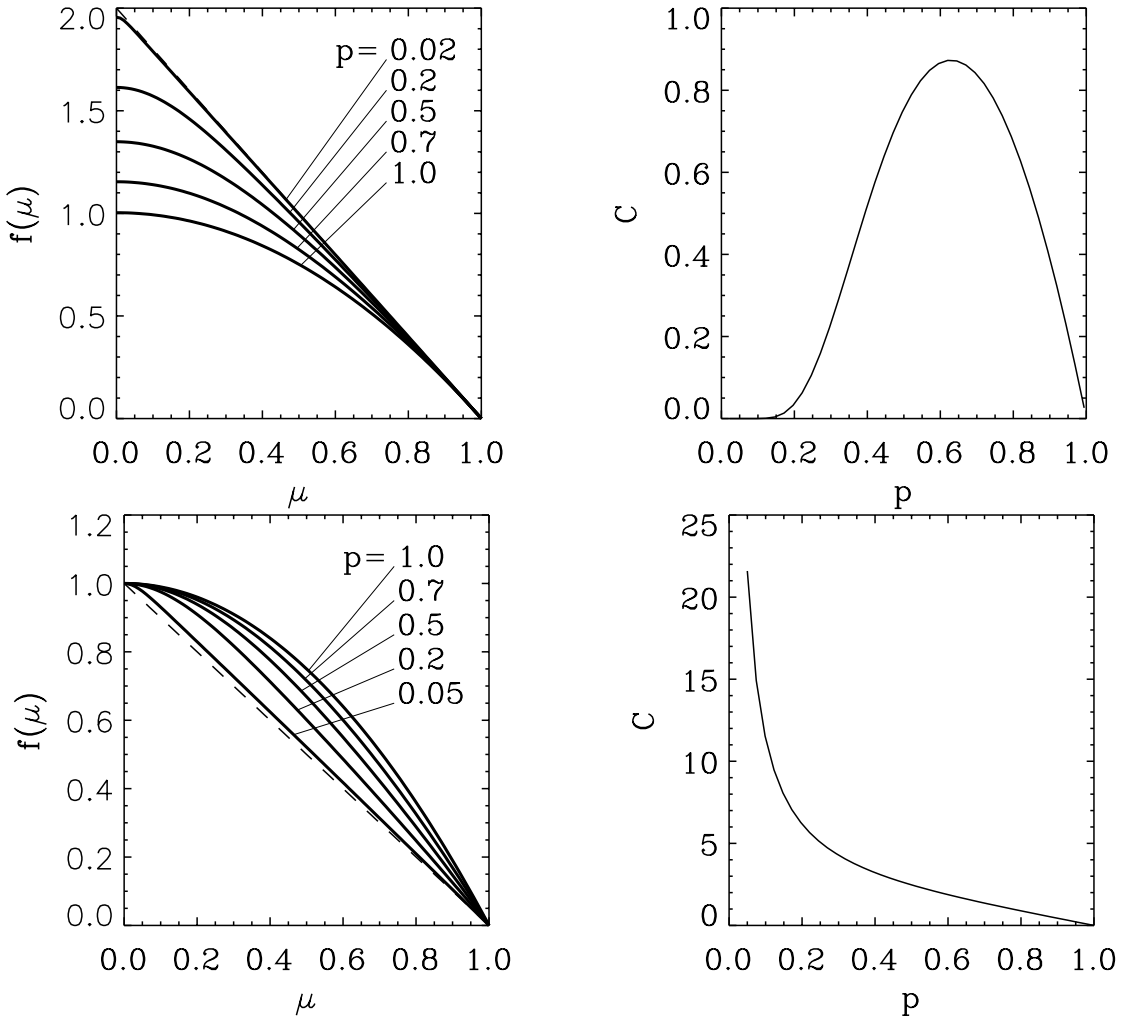

Figure 3.2: *Upper panels: the function $f(\mu)$ and the eigenvalue C for different values of p with the prescription of constant B_{pole} (the dashed line in the left panel is the analytical solution for $p \to 0$). Lower panels: same, but for constant flux.*

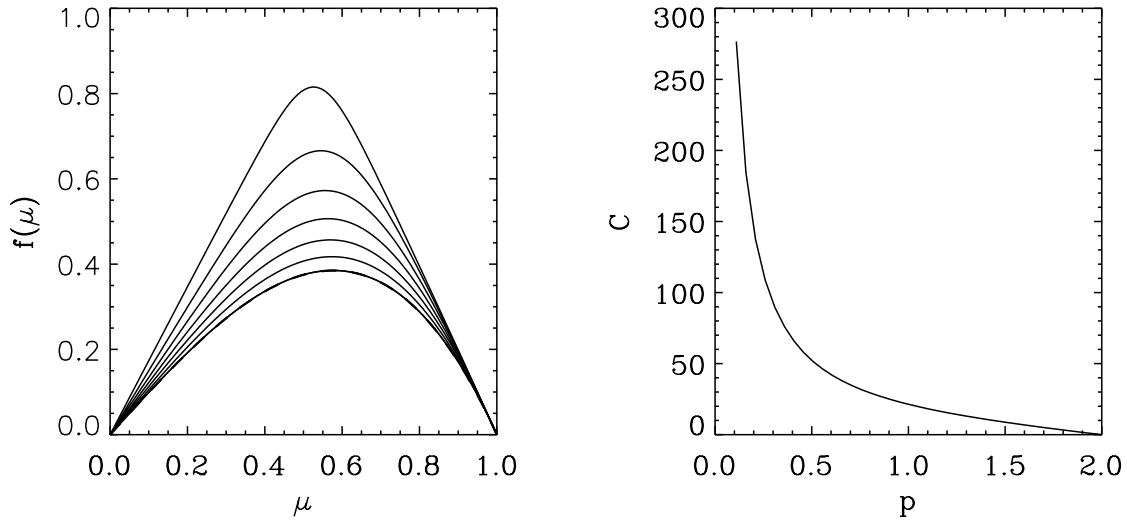

Figure 3.3: *Generating functions and eigenvalues for quadrupolar fields. Different curves correspond to different values of p from $p = 2$ (lower curve) to $p = 0.2$ (upper curve).*

which gives $\lambda(0) = 2$, in agreement with the numerical result (see again table 3.1).

3.2.3 Higher order multipoles

Since equation (3.7) is the force-free condition for a generic axisymmetric field (as given by equation [4.23]), axisymmetric globally-twisted multipoles can be found solving again equation (3.7), subject to the boundary conditions discussed in § 3.2.1.

For an untwisted quadrupolar field the generating function is

$$f_{p_0=2} = \mu\,(1-\mu^2). \tag{3.14}$$

Within our integration domain $0 \leq \mu \leq 1$, the poles are located at $\mu = 0$ (degenerate) and $\mu = 1$. The boundary conditions are then

$$\begin{aligned} f(1) &= 0 \\ f(0) &= 0 \\ f'(1) = -2 \quad &\text{or} \quad f\left(\frac{1}{\sqrt{3}}\right) = \frac{2}{3\sqrt{3}}; \end{aligned} \tag{3.15}$$

the latter two conditions enforce either constant field strength at the pole or constant flux, and, as discussed in the previous section are equivalent. However, on a numerical ground, we found that for higher order multipoles the constant flux boundary condition is highly preferable and has been used in the calculations presented here. The field in $-1 \leq \mu \leq 0$ is obtained by symmetry. The quadrupolar angular functions $f(\mu)$ and eigenvalues $C(p)$ are shown in Fig. 3.3 for different values of p.

The shear angle as a function of p, equation (3.8), is shown in Fig. 3.4 (middle curve).

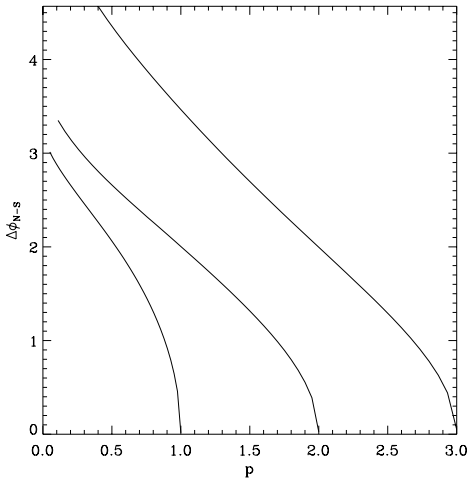

Figure 3.4: *The shear angle $\Delta\phi_{NS}$ as a function of p. The three curves correspond to dipolar quadrupolar and octupolar fields (from left to right).*

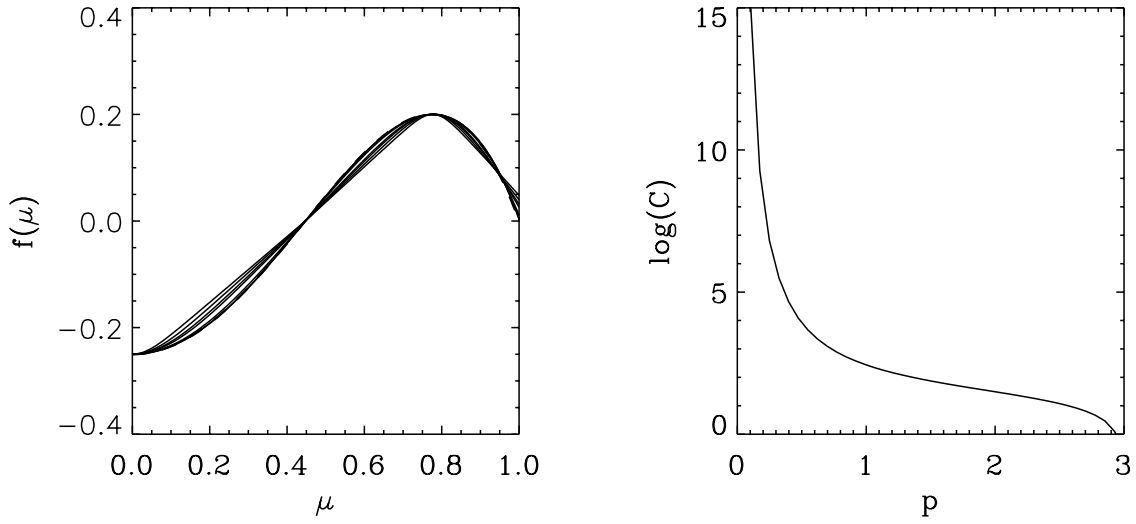

Figure 3.5: *Same as Fig. 3.3 but for octupolar fields; here p is in the range $[0.2, 3]$.*

In the case of an untwisted octupole, instead, the generating function is

$$f_{p_0=3} = \frac{1}{4}(1-\mu^2)(5\mu^2-1) \tag{3.16}$$

and the poles are located at $\mu = 1, 1/\sqrt{5}$ (again restricting to the range $0 \leq \mu \leq 1$). In order to compute the sheared field, equation (3.7) needs to be solved in two separate intervals, $0 \leq \mu \leq 1/\sqrt{5}$ and $1/\sqrt{5} \leq \mu \leq 1$. Taking into account that $\mu = 0$ is not a pole in the present case, the boundary conditions are

$$\begin{aligned} f(1/\sqrt{5}) &= 0 \\ f'(0) &= 0 \\ f'(1/\sqrt{5}) = \frac{2}{\sqrt{5}} \quad &\text{or} \quad f(0) = -\frac{1}{4} \end{aligned} \tag{3.17}$$

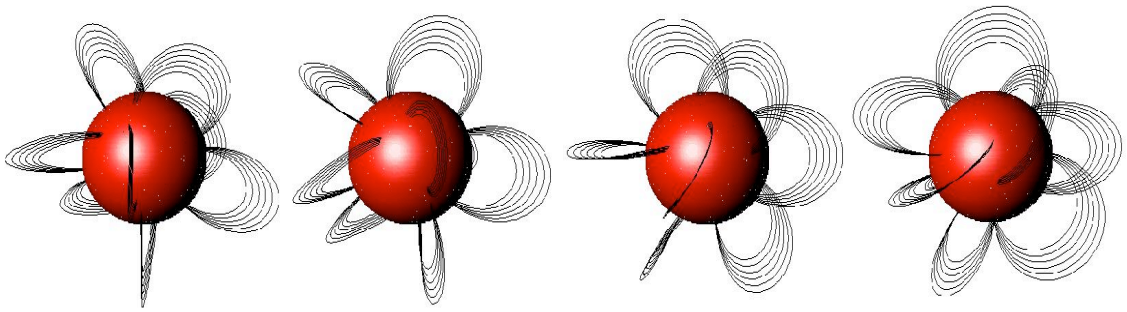

(a) $\Delta\phi_{NS} = 0.4$ *rad.* **(b)** $\Delta\phi_{NS} = 1.3$ *rad.* **(c)** $\Delta\phi_{NS} = 2$ *rad.* **(d)** $\Delta\phi_{NS} = 2.7$ *rad.*

Figure 3.6: *Field lines in a (twisted) quadrupolar magnetosphere. The twist angle between north and south polar caps is reported at the bottom of each panel.*

in the range $0 \leq \mu \leq 1/\sqrt{5}$ and

$$\begin{aligned} f(1) &= 0 \\ f(1/\sqrt{5}) &= 0 \\ f'(1) &= -2 \quad \text{or} \quad f\left(\sqrt{\frac{3}{5}}\right) = \frac{1}{5} \end{aligned} \tag{3.18}$$

in the range $1/\sqrt{5} \leq \mu \leq 1$. The numerical solutions are shown in Fig. 3.5 and the dependence of the shear angle on p can be read from Fig. 3.4 (rightmost curve).

Despite the numerical solution of equation (3.7) poses no problems, having analytical expressions for the twisted field components may prove handy in some applications. In Appendix 3.4 we derive approximated analytical expressions for the generating function $f(\mu)$ for dipolar and quadrupolar configurations valid for small shear ($p_0 - p \ll 1$), compare them with the exact numerical solutions and discuss their ranges of validity. The field lines of twisted multipoles are displayed in figure 3.6 and 3.7. All the multipoles tend to the radial field in the split monopole limit, but in the figures we have changed the scaling factor with the shear angle to better visualize the effects on the field lines.

3.3 Spectra and lightcurves

In this section we use the numerical code described in [93, NTZ in the following] to explore the effects of different sheared multipolar fields on the emergent spectra and lightcurves of magnetars. We base our model on the scenario envisaged by TLK [see also 76, 43, 93, for more detailed calculations], according to which thermal photons originating at the star surface undergo repeated scatterings with the charge carriers (electrons, ions and possibly pairs; see also Beloborodov & Thompson [8]) flowing along the field lines. These investigations were based on non-relativistic computations, and therefore necessarily restricted to the low-energy ($\lesssim 10$ keV) emission. Furthermore, they were based on the dipolar, globally-

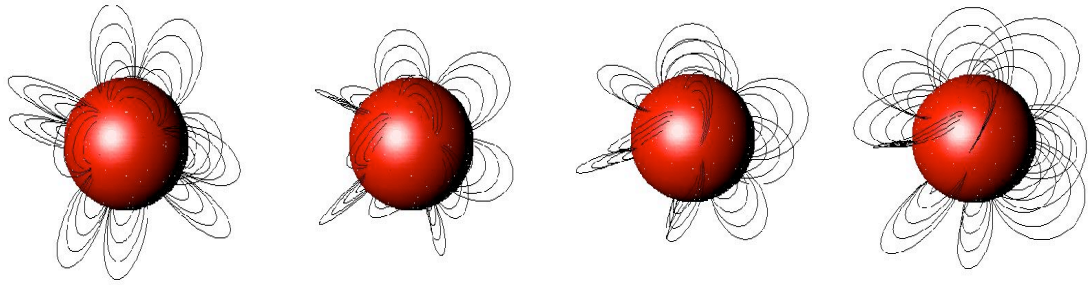

(a) $\Delta\phi_{NS} = 0.4$ *rad.* **(b)** $\Delta\phi_{NS} = 1.5$ *rad.* **(c)** $\Delta\phi_{NS} = 2.5$ *rad.* **(d)** $\Delta\phi_{NS} = 3.5$ *rad.*

Figure 3.7: *Field lines in a (twisted) octupolar magnetosphere. The twist angle between north and south polar caps is reported at the bottom of each panel.*

twisted magnetosphere of TLK [2].

3.3.1 Globally twisted multipoles

In order to gain some insight on the properties in the emitted spectra when the magnetosphere is threaded by twisted, higher order multipoles, we plot in Figs. 3.8a and 3.8b the optical depth τ_{res} to resonant scattering corresponding to quadrupolar and octupolar fields. This is given by

$$\left(\frac{v}{c}\right)\tau_{res} \sim \frac{\pi}{4}(1+\cos^2\theta_{kB})\left[\frac{C(1+p)}{p}\right]^{1/2}\frac{f^{1/p}}{2+p} \tag{3.19}$$

where v is the charge velocity and θ_{kB} is the angle between the primary photon (assumed to move radially) and the magnetic field at the scattering radius (TLK). Since $v \sim c$, $(v/c)\tau_{res} \sim \tau_{res}$ and we make no further distinction between these two quantities. By comparing these curves to those in Fig. 3.8 we can clearly see that the optical depth for higher order multipoles is sensibly different from that of a dipolar configuration, implying that the overall spectral properties, and in particular those of the pulse phase emission, may be significantly affected.

To further investigate this, we calculated a number of synthetic spectra and lightcurves by using the non-relativistic Monte Carlo code by NTZ. A comparison among spectra produced by a globally twisted dipolar, quadrupolar and octupolar magnetosphere is shown in Fig. 3.9. Spectra have been computed for the same values of model parameters (blackbody temperature $kT_\gamma = 0.5$ keV, temperature and bulk velocity of the magnetospheric electrons $T_{el} = 30$ keV, $\beta_{bulk} = 0.5$, polar magnetic field strength $B_{pole} = 10^{14}$ G), and for the same shear angle ($\Delta\phi_{NS} = 1.2$ rad, which corresponds to $p = 0.8, 1.6, 2.5$ for the dipole, the quadrupole and the octupole, respectively). Spectra have been computed by collecting photons over the entire observer's sky (i.e. by angle-averaging over all viewing directions). The most prominent feature in Fig. 3.9 is the higher comptonization degree induced by the quadrupolar (and dipolar) field with respect to the octupolar one. This can be understood in

[2]The simplified, analytical model of Lyutikov & Gavriil [76] did not assume a precise topology for the magnetic field.

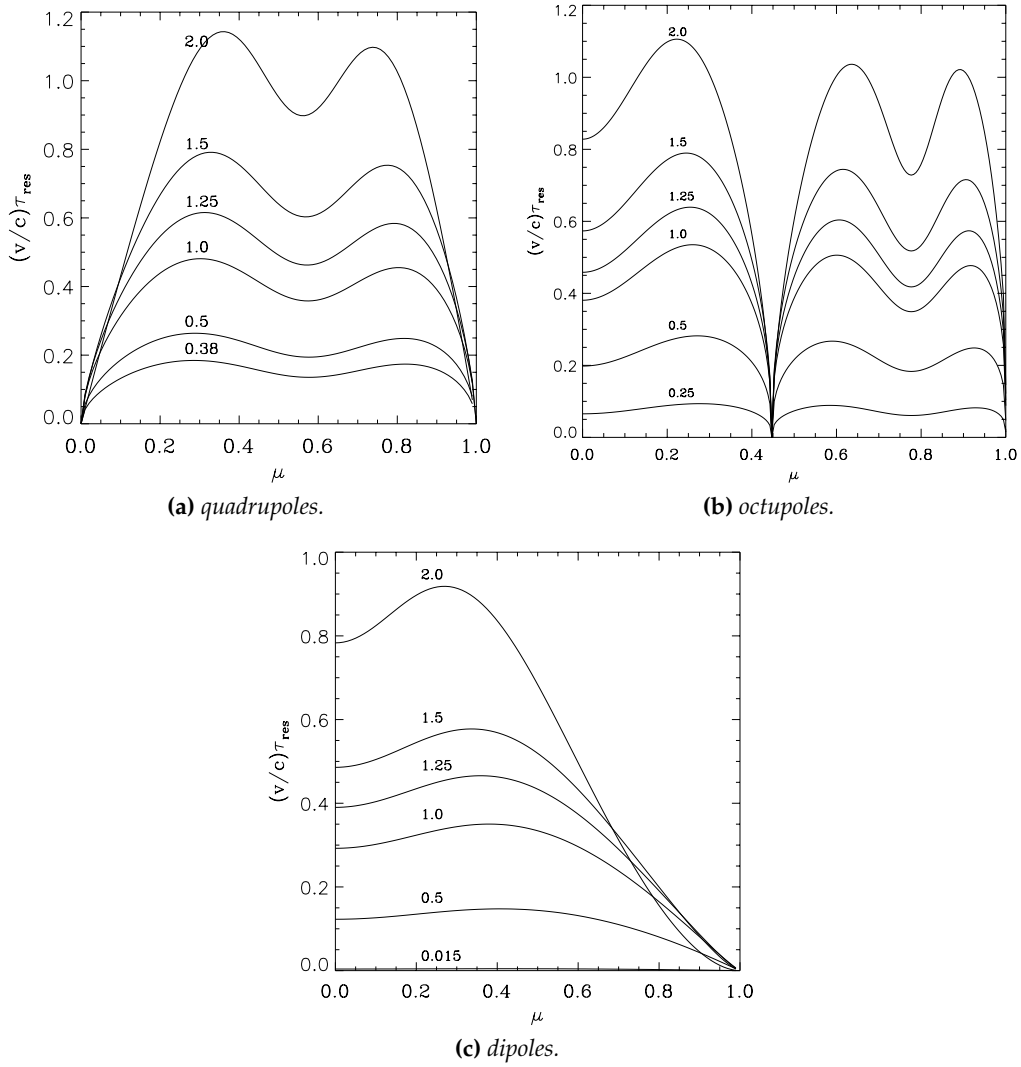

(a) *quadrupoles.*

(b) *octupoles.*

(c) *dipoles.*

Figure 3.8: *Optical depth to resonant cyclotron scattering at the resonant radius as a function of the colatitude for multipolar configurations; each curve is labelled by the value of the shear angle* $\Delta\phi_{NS}$.

terms of the different spatial distribution of the scattering particles (see Figs. 3.8a, 3.8b, 3.8c) and of the different efficiency of scatterings, the latter depending on the (average) angle between the photon direction and that of the flowing currents. Upscattering is more efficient in regions where the currents move towards the star, i.e. close to the magnetic south pole(s), because collisions tend to occur more head-on (see also NTZ). For a dipolar field the more favourable situation (i.e. large optical depth and currents flowing towards the star) arises for $\mu \sim -0.3$ (compare with the spectra at different viewing angles in Fig. 1 of NTZ; the one at $\Theta_S = 116^\circ$ is the more comptonized). For the quadrupole returning currents are localized around $\mu \sim 0$ (the geographical equator which is a degenerate south pole) and there are two regions with large optical depth in $0 \leq \mu \leq 1$ (see fig. 3.8a). The one at $\mu \sim 0.3$ is closer to the south pole ($\mu = 0$) than in the case of the dipole, for which it occurs at $\mu \sim -0.3$ while the south pole is at $\mu = -1$. The reason for which octupolar twisted fields produce less efficient upscattering is that, despite there are two maxima of the optical depth located quite

close to the south pole (at $\mu \sim 0.2,\ 0.6$, the south pole is at $\mu = 1/\sqrt{5} \sim 0.45$), the relatively large curvature of the field lines makes the angular extent of the region where currents are inflowing narrow. As a consequence most photons scatter with electrons moving at large angles and this results in steeper spectra.

3.3.2 A simple localized twist model

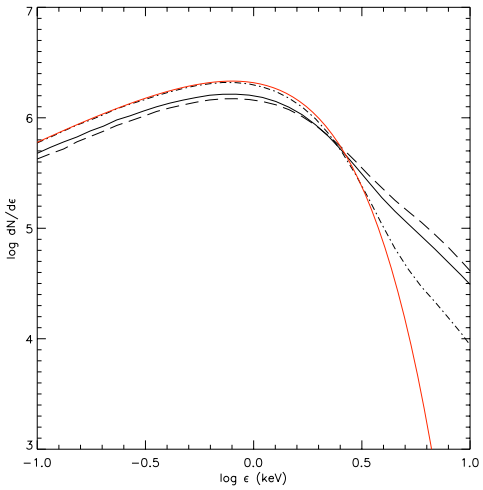

Figure 3.9: *Monte Carlo spectra for globally twisted dipolar (solid line), quadrupolar (dashed line), octupolar (dash-dotted line) force free magnetospheres; the shear angle is the same in all three cases ($\Delta\phi_{NS}$=1.2 rad). The solid red line is the seed blackbody spectrum. The total number of photons is $\sim 4 \times 10^6$ in all the simulations.*

There is now observational evidence that, at least in some cases, the magnetospheric twist in both SGRs and AXPs could be localized in restricted regions of the magnetosphere. For instance, Woods et al. [130] found a certain degree of hysteresis in the long-term evolution of SGR 1806-20 prior the emission of the giant flare in December 2004, with a non trivial correlation between spectral and timing properties that may be interpreted if only a small bundle of magnetic field lines is affected by the shear. A further case is provided by the spectral evolution of the transient AXP XTE J1810-197 [98, 9] which seems to require a twist concentrated towards the magnetic axis, giving rise to a polar hot region, possibly with a meridional temperature gradient.

Motivated by this, we investigated the possibility to model a localized twist, by constructing a solution in which the shear changes with the magnetic colatitude of the field line foot point. Although the configurations presented in the previous sections are globally twisted, the octupolar solution, which requires piecewise integration in two domains (see § 3.2.3), can be used to construct a field with a non-vanishing twist at low magnetic co-latitudes. This is done by superimposing a sheared octupole for $0 \leq \mu \leq 1/\sqrt{5}$ to a potential one in $1/\sqrt{5} \leq \mu \leq 1$ and is equivalent to solve equation (3.7) in the entire domain with $p(\mu) = p^* H(\mu - 1/\sqrt{5})$, where H is the Heaviside step function and p^* a given constant. We note that, although not physically self-consistent, such a field is force-free (see the discussion in Chapter 4.2.1).

The Monte Carlo spectra for different viewing angles are shown in Fig. 3.10 in the case in which the field has equatorial symmetry, i.e. the shear $\Delta\phi_{NS} = 1.5$ rad ($p = 2.3$) is applied on both polar lobes while the equatorial zone is permeated by a potential octupole. The spectra for the more interesting case in which the same shear is confined only around one pole are plotted in Fig. 3.10b.

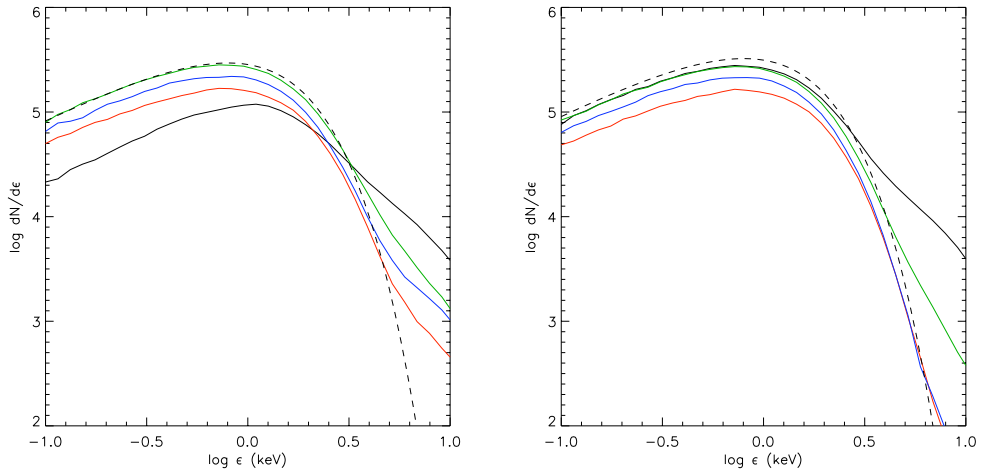

(a) *Shear equally distributed on both polar lobes and potential field in the equatorial zone.*

(b) *Shear localized only at upper north pole and potential field elsewhere.*

Figure 3.10: *Spectra obtained with the Monte Carlo code for locally twisted ($\Delta\phi_{NS} = 1.5$ rad, $p = 2.3$) octupolar force-free magnetospheres. Different curves correspond to different viewing angles (blue $\Theta_S = 0°$, red $\Theta_S = 60°$, green $\Theta_S = 104.5°$, black $\Theta_S = 180°$; the dashed line is the seed blackbody spectrum.*

3.3.3 Timing and spectral properties of magnetars high-energy emission

Spectral models which account for different magnetospheric configurations hold the potential to reproduce not only the gross features of the observed spectra but also the subtler properties which are revealed by the combination of very high-quality spectral and timing data. While a complete application is beyond our scope, here we consider our results in the context of the spectacular phase-dependence which has been recently discovered in the the hard X-ray tails of the two AXPs 1RXS J1708-4009 and 4U 0142+61 [31, 32]. These deep *INTEGRAL* observations have shown that, in both these sources, there are several different pulse components (at least three) with genuinely different spectra. The hard X-ray spectrum gradually changes with phase from a soft to an hard power law, the latter being significantly detected over a phase interval covering $\sim 1/3$, or more, of the period.

In order to see how these features can, at least qualitatively, be explained by our models, let us consider the locally twisted configurations discussed in § 3.3.2 which, among those presented so far, provide the most significant variations of the magnetic topology with the colatitude. Let us introduce two angles, χ and ξ, which give, respectively, the inclination of the LOS and of the magnetic axis with respect to the star spin axis. This allows us to take into account for the star rotation and hence derive pulse profiles and phase-resolved spectra. Because of the lack of north-south symmetry, it is $0 \leq \chi \leq \pi$, while ξ spans the interval $[0, \pi/2]$ (see NTZ for further details). For each viewing geometry, and for different values of the shear, we can now compute the optical depth (equation [3.19]) as a function the rotational phase γ ($0 \leq \gamma \leq 2\pi$). A few examples are shown in Fig. 3.11 for the case in which the twist is localized on two polar caps.

In connection with the spectral evolution with phase observed in 1RXS J1708-4009 and

4U 0142+61, the more favourable cases are those in which it is $(v/c)\tau_{res} > 1$ for roughly one third of the period. This is because resonant scattering over a population of (relativistic) electrons is then expected to be most efficient in producing a hard tail over the right phase interval, while the decrease of the depth at other phases results in a softening of the spectrum. A complete exploration of the parameter space aimed at searching for all configurations for which the previous condition is met is beyond the purposes of this thesis. Just for illustrative purpose, let us consider one of those, i.e. an octupolar field with shear $\Delta\phi_{N-S} = 1.5$. By assuming this value and taking $\xi = 32^\circ$ $\chi = 140^\circ$, we then computed phase resolved spectra and energy dependent lightcurves by using our Monte Carlo code. Since we are dealing with photon energies ≈ 100 keV, at which electron recoil and relativistic effects may become important, we performed the runs using a relativistic version of the code [94, Nobili, Turolla & Zane, in preparation]. Results are reported in Figs. 3.12 and 3.14. Again in the spirit of probing the potentialities of our model, rather than a presenting a detailed fit, the parameter values in the Monte Carlo runs are chosen somehow arbitrarily, and are the same as those adopted in § 3.3.2, $B_{\rm pole} = 10^{14}$ G, $\beta_{bulk} = 0.5$, $T_{el} = 30$ keV and $T_\gamma = 0.5$ keV.

As it can be seen from Fig. 3.12, for a magnetic configuration with the shear concentrated in a single lobe, resonant comptonization gives rise to a hard tail which is quite pronounced at the peak of the pulse while it is depressed by almost an order of magnitude at pulse phases close to the minimum of the hard X-ray lightcurve. This is similar to what observed in AXP 1RXS J1708-4009 and AXP 4U0142+61 [31, 32]. This model also predicts a considerable variation of the pulsed fraction with energy, ranging from a few percent below 2 keV, to a few tens of percent from 2 to 10 keV and up to 90% in the harder part of the spectrum. The comparison between modelled and observed phase-resolved spectra is beyond the scope of the present investigation.

For comparison we show in Fig. 3.13 the same results computed by assuming a globally twisted dipolar magnetosphere, with the same shear and taking the same parameters for the viewing geometry and the Monte Carlo run. It is clear that the pulse resolved spectra and lightcurves obtained in this case are completely different and cannot reproduce those observed from the two AXPs. In this case, the hard part of the spectrum show very little variation with the rotational phase and the lightcurve dependence on the energy is opposite to that shown in Fig. 3.12, with a larger pulsed fraction expected in the soft band. Spectra and lightcurves obtained with a local twist applied at both polar regions produce results which, again, are not in agreement with observations (see Fig. 3.14).

3.4 Analytical approximations

We start by expressing both the generating function and the eigenvalue C in terms of a series expansion around the corresponding known untwisted quantities (labelled again

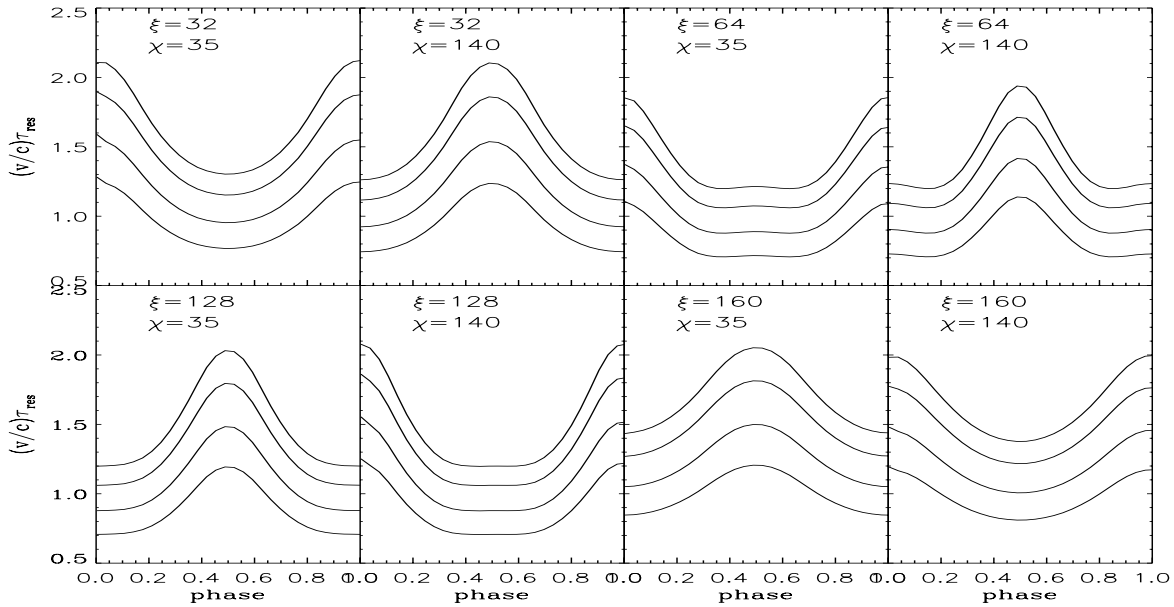

Figure 3.11: *The depth $(v/c)\tau_{res}$ versus rotational phase for an octupolar field with twist located on the two polar caps. Each panel refer to different values of the geometrical angles χ and ξ (see text for details). The curves in each panel are for $\Delta\phi_{N-S} = 1.22, 1.50, 1.78, 1.96$ from bottom to top.*

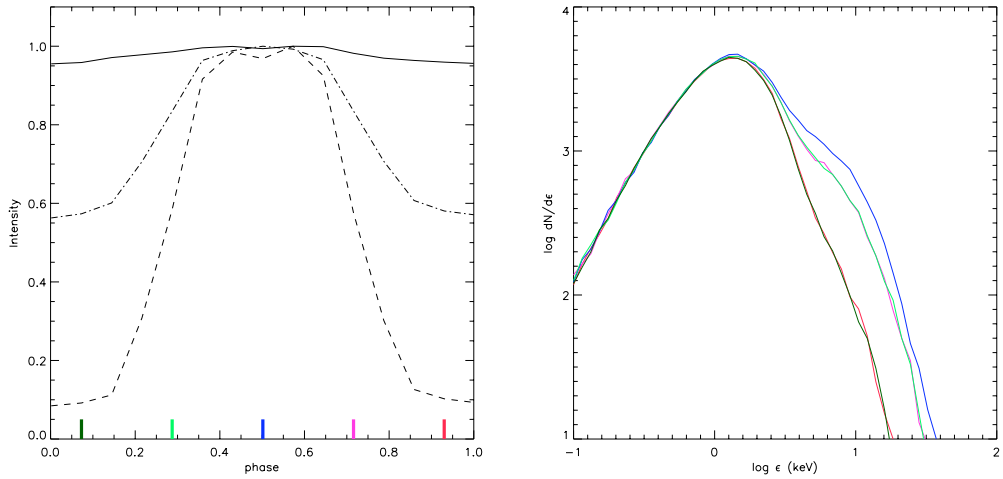

Figure 3.12: *Synthetic lightcurves (upper panel) and phase-resolved spectra (lower panel) for a twisted magnetosphere with shear applied only to one polar lobe of an octupolar field (see text for details). In the upper panel the solid, dash-dotted and dashed lines refer to the pulse profiles in the 0.5–2, 2–10 and 10–100 keV bands respectively. In the lower panel curves with different colors give the spectra at various phases; the color code can be read at the bottom of the upper panel.*

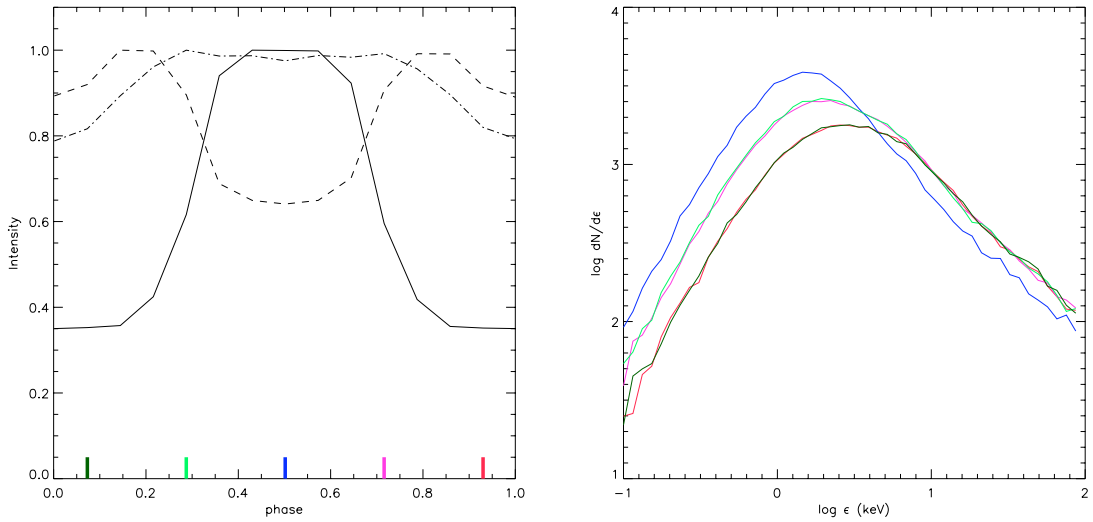

Figure 3.13: *Same as Fig. 3.12, here for a globally twisted dipolar field.*

with the index 0)

$$\begin{aligned} C &= C_0 + \left(\frac{\mathrm{d}C}{\mathrm{d}p}\right)_{p_0} \Delta p + \dots \\ f(\mu) &= f_0(\mu) + f_1(\mu)\Delta p + \dots \end{aligned} \tag{3.20}$$

where $\Delta p \equiv p - p_0$. By substituting the previous expressions into equation (3.7), we obtain, to first order in Δp,

$$(1-\mu^2) f_1''(\mu) + p_0(1+p_0) f_1(\mu) + (1+2p_0) f_0 + \left(\frac{\mathrm{d}C}{\mathrm{d}p}\right)_{p_0} f_0^{1+2/p_0} = 0\,. \tag{3.21}$$

It can be easily seen that equation (3.21) admits analytical solutions only for integer values of the exponent $2/p_0$, i.e. for dipoles and quadrupoles for which $2/p_0 = 2$ and 1, respectively. Since f_0 is itself a solution of the GSS equation, it satisfies the same boundary conditions we need to impose on f. This implies that the conditions on f_1 are, in the case of a dipolar field, $f_1(1) = f_1'(0) = 0$, supplemented by either $f_1'(1) = 0$ or $f_1(0) = 0$. The two solutions that obey the previous two sets of conditions are

$$\begin{aligned} f_1(\mu) &= f_0 \frac{-17 + 22\mu^2 - 5\mu^4}{32} \\ \left(\frac{\mathrm{d}C}{\mathrm{d}p}\right)_{p_0} &= -\frac{35}{8} \end{aligned} \tag{3.22}$$

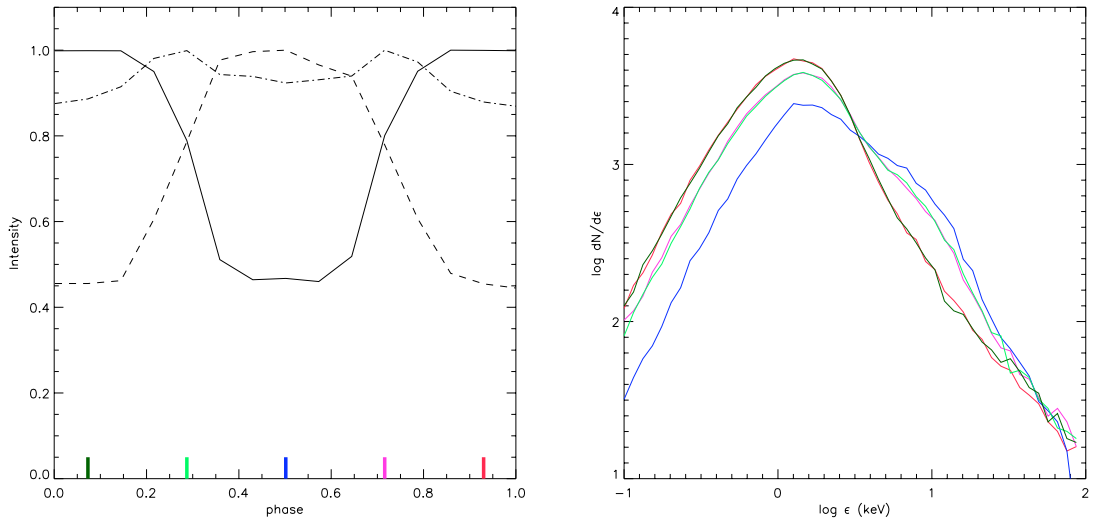

Figure 3.14: *Same as Fig. 3.12, here for the case in which the shear is applied to both polar regions.*

and

$$f_1(\mu) = f_0 \frac{22\mu^2 - 5\mu^4}{32}$$
$$\left(\frac{\mathrm{d}C}{\mathrm{d}p}\right)_{p_0} = -\frac{35}{8}, \tag{3.23}$$

respectively, where $f_0(\mu) = 1 - \mu^2$. The complete expressions for the two generating functions are then

$$f_{W95} \sim f_0 \left(1 + \frac{5f_0 + 17}{32}\mu^2 \Delta p\right)$$
$$f_{TLK} \sim f_{W95} - \frac{17}{32} f_0 \Delta p; \tag{3.24}$$

since $\Delta p < 0$, it is $f_{W95} < f_{TLK}$ for any value of the parameter in accordance with numerical results. A comparison of the first order approximations with the exact numerical solutions is shown in Fig. 3.15. We find that the agreement between the two is satisfactory (relative error $\lesssim 8\%$) up to $\Delta\phi_{NS} = 0.2$ in the case of fixed intensity and $\Delta\phi_{NS} = 0.4$ in the case of constant flux. The ratio $\lambda = f_{TLK}/f_{W95}$ introduced in § 3.2.2 can be expanded as

$$\lambda(p) = 1 - \frac{17}{32}\Delta p. \tag{3.25}$$

By applying the same procedure, one can derive the analytic first order expansion for quadrupolar fields. For $f_1(1) = f_1(0) = f_1'(1) = 0$, the first two terms in the expansion of f

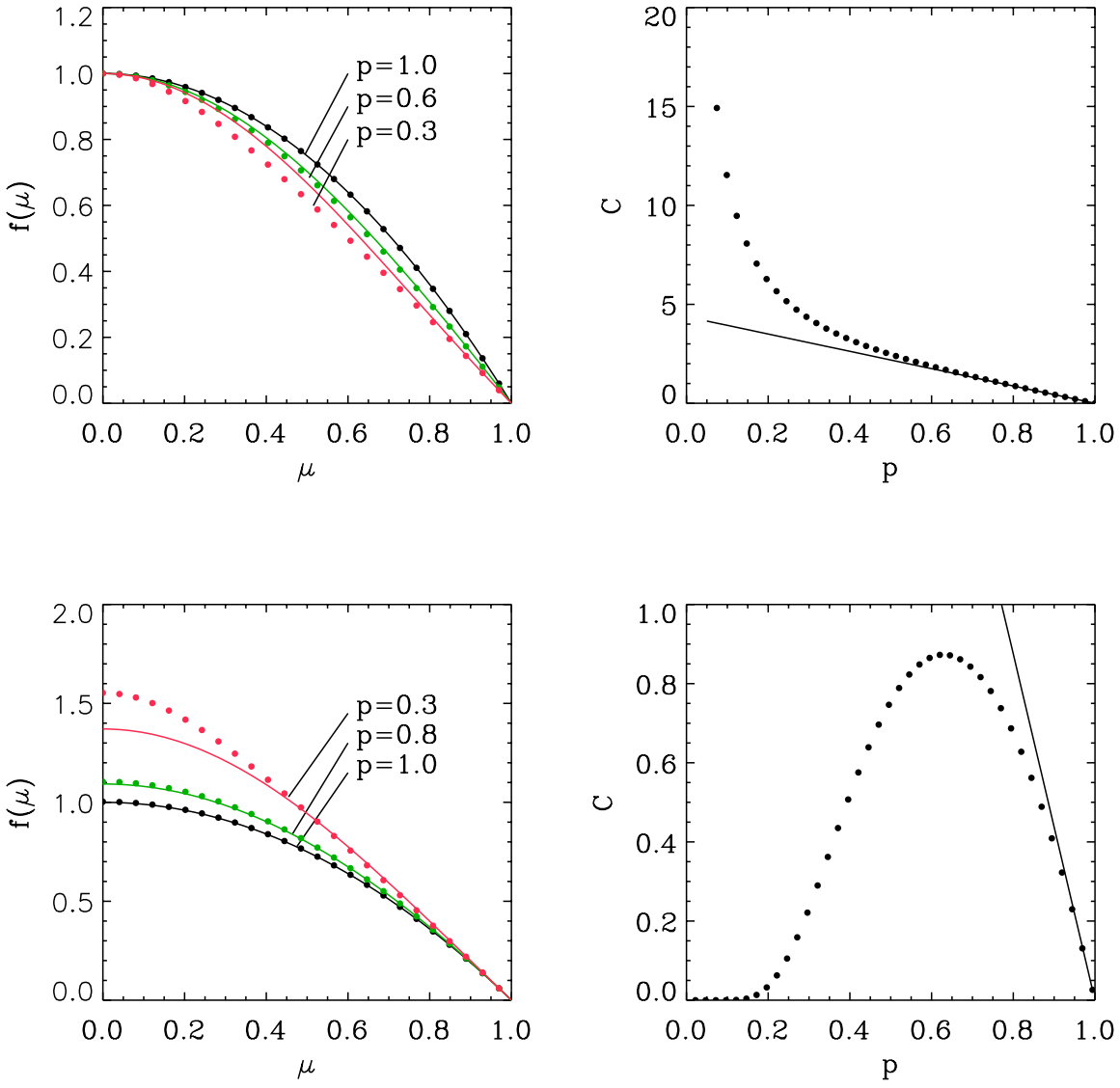

Figure 3.15: *Dipolar angular functions $f(\mu)$ and eigenvalues $C(p)$ obtained with fixed flux (upper panels) and fixed B_{pole} (lower panels). Solid lines represent the analytical first order approximation, while the dots are the numerical solutions of equation (3.7).*

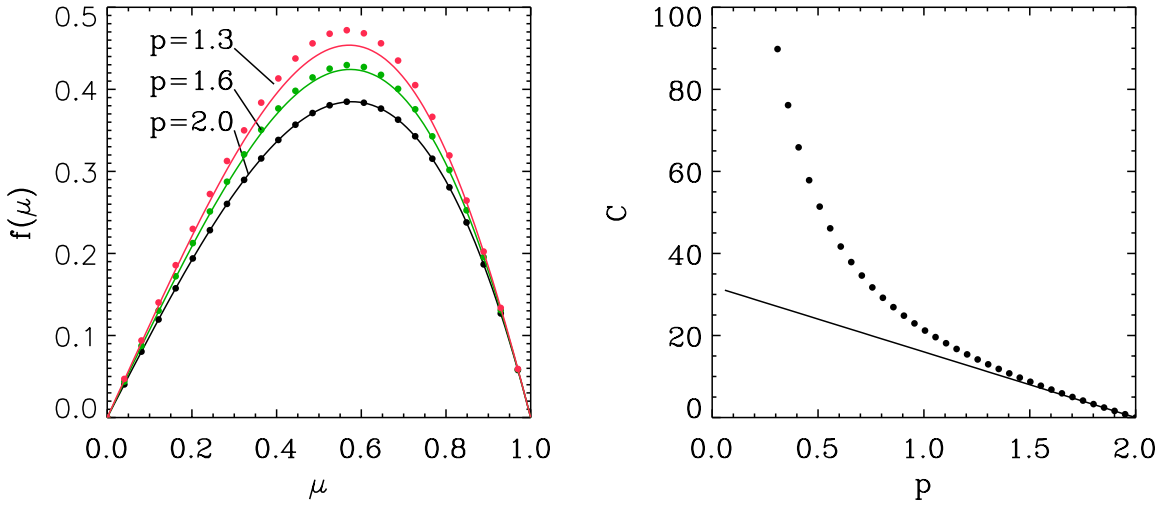

Figure 3.16: *Same as in Fig. 3.15 for the quadrupolar field.*

turn out to be

$$f_0(\mu) = \mu(1-\mu^2)$$
$$f_1(\mu) = f_0\left[\frac{3(1-\mu)-8\mu^2}{6(1+\mu)} + \frac{2}{3}\mu^3 + \ln(1+\mu) - \ln 2\right] \tag{3.26}$$

together with

$$\left(\frac{\mathrm{d}C}{\mathrm{d}p}\right)_{p_0} = -16\,.$$

The generating function f and $C(p)$ are shown, together with the numerical solutions, in Fig. 3.16.

3.5 Composition of mutipoles

In order to describe a general field, one of the possibilities is to represent the field as a composition of multipoles. As previously stated, a field obtained by the superposition of twisted multipoles does not represent a global force free field, unless the shear applied to the fields is quite null. A different approach to the problem is to decompose a field into a number of multipoles, assuming that the dominating one follow the usual force free equations, and derive the equations that must be satisfied by the other components in order to produce a total force free field.

As an example of this approach, we can decompose the global field into only two multipoles, e.g. a dipole and a quadrupole. The field, as well as the two components, can be

expressed again as a poloidal plus a toroidal part

$$\boldsymbol{B}_{TOT} = \boldsymbol{B}_1 + \boldsymbol{B}_2 = \boldsymbol{B}_{TOT_{pol}} + \boldsymbol{B}_{TOT_\phi} \tag{3.27}$$

where the poloidal part is

$$\begin{aligned} \boldsymbol{B}_{TOT_{pol}} &= \boldsymbol{B}_{1_{pol}} + \boldsymbol{B}_{2_{pol}} \\ &= \frac{\nabla \mathscr{P} \times \hat{\boldsymbol{e}}_{\boldsymbol{\phi}}}{r \sin\theta} \\ &= \frac{\nabla \mathscr{P}_1 \times \hat{\boldsymbol{e}}_{\boldsymbol{\phi}}}{r \sin\theta} + \frac{\nabla \mathscr{P}_2 \times \hat{\boldsymbol{e}}_{\boldsymbol{\phi}}}{r \sin\theta} \, . \end{aligned} \tag{3.28}$$

The flux function therefore should be in the form $\mathscr{P} = \mathscr{P}_1 + \mathscr{P}_2$, and the toroidal component, analogously, should be a function $F(\mathscr{P}) = F_1(\mathscr{P}_1) + F_2(\mathscr{P}_2)$.

The main hypothesis is that the dipolar component and the total field are force free fields, and thus follow the same general equations of § 3.2, that are

$$\frac{\partial \mathscr{P}}{\partial r}\frac{\partial F}{\partial \mu} - \frac{\partial \mathscr{P}}{\partial \mu}\frac{\partial F}{\partial r} = 0 \tag{3.29a}$$

$$\frac{\partial^2 \mathscr{P}}{\partial r^2} + \frac{1-\mu^2}{r^2}\frac{\partial^2 \mathscr{P}}{\partial \mu^2} + F\frac{\partial F}{\partial \mathscr{P}} = 0 \, . \tag{3.29b}$$

The other component (here the quadrupole) is not, a priori, a force free fields. Function $F_2(\mathscr{P}_2)$ thus is unknown and has to be determined by the final equations.

The difference between the dipolar component and the global field is expressed by the form chosen for the flux function. For the dipole, as usual, the functions (denoted here with the suffix 1) are

$$\begin{aligned} \mathscr{P}_1 &= r^{-p} f_1(\mu) \\ F_1(\mathscr{P}_1) &= \lambda \, \mathscr{P}_1^{1+1/p} \\ &= \lambda \, r^{-(p+1)} \, f_1^{1+1/p} \end{aligned} \tag{3.30}$$

where this particular choice of $F_1(\mathscr{P}_1)$ satisfy the former of equations (3.29a), while the latter, as usual, becomes

$$(1-\mu^2) f_1" + p(p+1) f_1 + \lambda \, \frac{p+1}{p} f_1^{1+2/p} = 0 \tag{3.31}$$

for the global field, instead, the flux function is chosen as

$$\mathscr{P} = \mathscr{P}_1 + \mathscr{P}_2 = r^{-p} f_1(\mu) + r^{-q} f_2(\mu) \, . \tag{3.32}$$

Substituting into equations (3.29a) the expressions for $\mathscr{P}_1, \; F_1, \text{and} \mathscr{P}$ the equations be-

come

$$\frac{\partial(\mathscr{P}_1+\mathscr{P}_2)}{\partial r}\frac{\partial(F_1+F_2)}{\partial \mu}-\frac{\partial(\mathscr{P}_1+\mathscr{P}_2)}{\partial \mu}\frac{\partial(F_1+F_2)}{\partial r}=0 \tag{3.33a}$$

$$\frac{\partial^2(\mathscr{P}_1+\mathscr{P}_2)}{\partial r^2}+\frac{1-\mu^2}{r^2}\frac{\partial^2(\mathscr{P}_1+\mathscr{P}_2)}{\partial \mu^2}+(F_1+F_2)\frac{\partial(F_1+F_2)}{\partial \mathscr{P}}=0 \tag{3.33b}$$

The term $\partial(F_1+F_2)/\partial\mathscr{P}$ can be decomposed in $\partial F_1/\partial\mathscr{P}+\partial F_2/\partial\mathscr{P}$ and, as each function is supposed to depend only on one of the flux functions, this expression result in $\partial F_1/\partial\mathscr{P}_1+\partial F_2/\partial\mathscr{P}_2$. Expanding and taking into account equation (3.31), with the ansatz $F_2(\mathscr{P}_2)=x\mathscr{P}_2^{1+1/q}=x\,r^{-(q+1)}\,f_2^{1+1/q}$ (useful to eliminate the radial dependence on the first equation), the expressions can be simplified into

$$\lambda(1+p)f_1^{1+1/p}f_2'+x(1+q)f_2^{1+1/q}f_1'-\lambda\frac{q\,(1+p)}{p}f_2\,f_1^{1/p}\,f_1'+ \\ -x\frac{p\,(1+q)}{q}f_1\,f_2^{1/q}f_2'=0 \tag{3.34a}$$

$$(1-\mu^2)f_2\text{"}+q(q+1)f_2+x^2\frac{1+q}{q}f_2^{1+2/q}+ \\ +\lambda x\left(\frac{1+p}{p}f_2+\frac{1+q}{q}\,r^{q-p}\,f_1\right)f_1^{1/p}f_2^{1/q}=0 \tag{3.34b}$$

Thus the equations to be solved in order to find the multipolar components of the field are (3.31) for B_1 and (3.34) for B_2. Once imposed the boundary conditions as discussed in § 3.2.1 for B_1,for each value of p the function $f_1(\mu)$ and the parameter $\lambda(p)$ are determined in the usual way. Thus, in equations (3.34), the unknown functions are $f_2(\mu)$ and the parameter $x(q)$. These are calculated for each value of q. The boundary conditions are determined again requiring a radial field B_2 on each of its (degenerate) poles and a fixed flux intensity of the total field $\boldsymbol{B}=\boldsymbol{B}_1+\boldsymbol{B}_2$ emerging from the north geometrical pole.

Chapter 4

Topology of magnetars external field. Non axisymmetric fields

In this chapter a further refinement of the describing model of the external field of magnetars will be performed. Until now we considered two major approximations in the description of the magnetosphere: force free condition and axial symmetry. Whereas the first one has great consequences on the properties of the field and can hardly be abandoned without modify the magnetar model, the condition of symmetry instead can be relaxed. We want to describe, therefore, the effects of the shear applied on a non-symmetric magnetosphere. While axisymmetric fields are described by a three dimensional vector, depending only on two coordinates $\boldsymbol{B} = [B_r(r,\theta), B_\theta(r,\theta), B_\phi(r,\theta)]$, the fields considered here depends on all three variables.
This last characteristic is common both to fields without any axis of symmetry, and to fields whose axis of symmetry is not the z-axis. As an example, a dipole referred to the z-axis is written as

$$\boldsymbol{B}_{dip_z} = \boldsymbol{B}_0 r^{-3} \left[2\cos\theta, \sin\theta, 0\right] \tag{4.1}$$

or, equivalently, in terms of the magnetic potential ψ

$$\boldsymbol{B}_{dip_z} = -\boldsymbol{\nabla}\psi_{dip_z} \tag{4.2a}$$

$$\psi_{dip_z} = B_0 \frac{\cos\theta}{r^2} \ . \tag{4.2b}$$

After a rotation denoted by the angles (Θ, Φ), the dipole's potential becomes

$$\psi_{dip} = \frac{B_0}{r^2}(\sin\theta\cos\phi\sin\Theta\cos\Phi + \sin\theta\sin\phi\sin\Theta\sin\Phi + \cos\theta\cos\Theta) \tag{4.3}$$

thus a rotation of $(\Theta = \pi/2, \Phi = 0)$, that cause the polar axis to coincide with the x-axis, produce

$$\psi_{dip_x} = B_0 \frac{\sin\theta\cos\phi}{r^2} \tag{4.4a}$$

$$\boldsymbol{B}_{dip_x} = -\boldsymbol{\nabla}\psi_{dip_z} = B_0 r^{-3}[2\sin\theta\cos\phi, -\cos\theta\cos\phi, \sin\phi] \; . \tag{4.4b}$$

This field, as well as the pure dipole referred to the y-axis, depends on all three coordinate variables, and therefore is not tractable with the equations developed in Chapter 3. We note here also that a pure dipole referred to a generic axis is obtained by a linear combination of the dipoles referred to the three coordinate axes.
The potentials of the pure multipoles are expressed, as already mentioned in § 2.1, in terms of spherical harmonics $Y_{\ell,m}(\theta,\phi)$,

$$\psi_\ell \propto \frac{1}{r^{\ell+1}} \sum_{m=-\ell}^{m=+\ell} Y_{\ell,m}(\theta,\phi) \; . \tag{4.5}$$

where the $m = 0$ case produce, for every order ℓ, multipoles referred to the vertical axis (and with no dependence on ϕ).
This expression, in the case $\ell = 2$ become

$$\begin{aligned}\psi_{quadr} = \frac{B_0}{4r^3} \big(3(&\sin^2\theta\sin 2\phi\sin^2\Theta\sin 2\Phi + \sin 2\theta\sin\phi\sin 2\Theta\sin\Phi \\ &+ \sin 2\theta\cos\phi\sin 2\Theta\cos\Phi + \sin^2\theta\cos 2\phi\sin^2\Theta\cos 2\Phi) \\ &+ (3\cos^2\theta - 1)(3\cos^2\Theta - 1)\big)\end{aligned} \tag{4.6}$$

and the corresponding field is a linear combination of five terms, where the coefficients (Q_i) are determined by the angles (Θ, Φ) identifying the polar axis

$$\boldsymbol{B}_{quadr} = \frac{B_0}{r^4} \sum_{i=0}^{4} Q_i b_i \tag{4.7a}$$

$$b_0 = 1/2\;[3\cos^2\theta - 1,\; \sin 2\theta,\; 0] \tag{4.7b}$$

$$b_1 = [\sin 2\theta\sin\phi,\; -2/3\cos 2\theta\sin\phi,\; -2/3\cos\theta\cos\phi] \tag{4.7c}$$

$$b_2 = [-\sin 2\theta\cos\phi,\; 2/3\cos 2\theta\cos\phi,\; -2/3\cos\theta\sin\phi] \tag{4.7d}$$

$$b_3 = [-\sin^2\theta\sin 2\phi,\; 1/3\sin 2\theta\sin 2\phi,\; 2/3\sin\theta\cos 2\phi] \tag{4.7e}$$

$$b_4 = [\sin^2\theta\cos 2\phi,\; -1/3\sin 2\theta\cos 2\phi,\; 2/3\sin\theta\sin 2\phi] \; . \tag{4.7f}$$

When solving the force free equation (2.3) we introduce a shear acting on the field perpendicularly to the z-axis. As shown in fig. 4.1, a field sheared perpendicularly to the z-axis (panel *a*) is intrinsically different from the same field subject to a shear perpendicular to a different direction (panel *b*). This last case, in turns, is equivalent to an inclined field subject to a shear again perpendicular to the z-axis (panel *c*). In this section we deal with this last

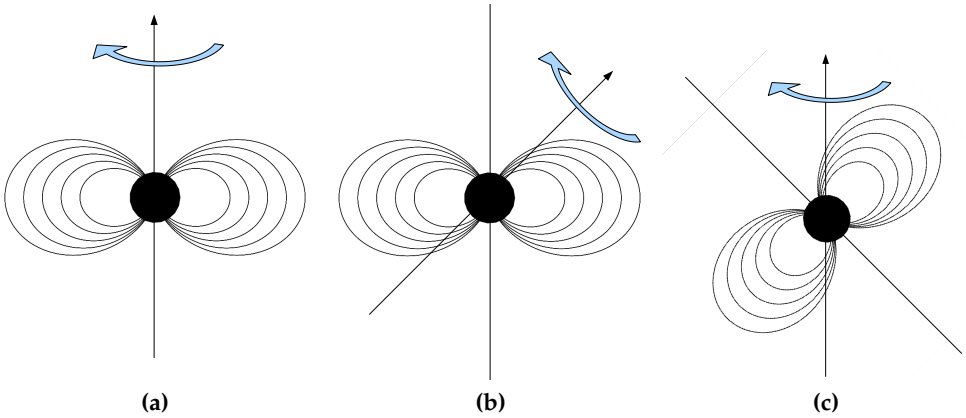

Figure 4.1: *Schematic view of the shear applied from different directions to a potential dipole. (a) The dipole, whose polar axis coincide with the z-axis, is subject to a shear deforming the field in a direction perpendicular to the axis. This case correspond to the solutions described in Chapter 3. (b) The same dipole is deformed by a shear acting on a direction not coincident with the axis of symmetry. This case produce different deformations to the field, and produce non symmetric sheared fields. This case is equivalent to case (c) of a shear perpendicular to the z-axis applied to a dipole referred to an inclined symmetric axis, and can be described by the formalism presented in this section.*

case, and, upon specification of the direction (Θ, Φ) of the polar axis, we can produce a vast case of sheared magnetospheres. The deformations that can be modelled, then, are intrinsically different from the ones described in Chapter 3, even when dealing with the same multipoles.

As we already discussed in § 2.3.2, in order to introduce the non-axisymmetric equations, we need to describe a generic magnetic field by means of two Euler potentials, and then to require the fulfillment of the force free condition (2.3).
Recalling the equations of that section, the field is expressed as

$$\boldsymbol{B} = \boldsymbol{\nabla}\psi_1 \times \boldsymbol{\nabla}\psi_2 \ .$$

The application of the force free condition lead to two equations

$$\boldsymbol{\nabla}\psi_1 \cdot \boldsymbol{\nabla} \times \boldsymbol{B} = 0 \tag{4.8a}$$

$$\boldsymbol{\nabla}\psi_2 \cdot \boldsymbol{\nabla} \times \boldsymbol{B} = 0 \, . \tag{4.8b}$$

These formulas holds both in the case of an intrinsically non-symmetric field and for one whose axis of symmetry is arbitrarily oriented. The difference between the two cases is introduced by the choice of the potentials and of the boundary conditions. In the rest of the chapter we will refer to the last case, assuming that the axis of symmetry is oriented in a generic direction (Θ, Φ).

Separation of variables is applied to the potentials, in order to find some convenient expression for equations (4.8). The results are shown in the following sections.

4.1 Reduction to the axisymmetric case

In section § 2.3.2, we have shown that equations (4.8) can lead to the GSS equation, when choosing the potentials in the form

$$\begin{aligned} \psi_1 &= \mathscr{P}(r,\theta) \\ \psi_2 &= \phi + \eta(r,\theta) \end{aligned} \tag{4.9}$$

with $\mathscr{P}$ is the usual poloidal flux function, ϕ the azimuthal angle and η an arbitrary function of r and θ. The field then becomes:

$$\boldsymbol{B} = \boldsymbol{\nabla}\mathscr{P} \times \frac{\hat{\boldsymbol{e}}_{\boldsymbol{\phi}}}{r\sin\theta} + \boldsymbol{\nabla}\mathscr{P} \times \boldsymbol{\nabla}\eta\,. \tag{4.10}$$

where the third component of the field is function only of the flux function $\mathscr{P}$:

$$\boldsymbol{\nabla}\mathscr{P} \times \boldsymbol{\nabla}\eta = \frac{1}{r\sin\theta} F(\mathscr{P})\hat{\boldsymbol{e}}_{\boldsymbol{\phi}} \tag{4.11}$$

For later convenience we introduce the function

$$X_\theta \equiv \frac{1}{r\sin\theta} F(\mathscr{P})\,. \tag{4.12}$$

Equations for $\mathscr{P}$ and $X_\theta = X_\theta(\mathscr{P})$ follow from equations (4.8) and are partial differential equations. Therefore, as in § 3.2, we introduce separation of variables for $\mathscr{P}$ to reduce them to ordinary differential equations. The flux function is therefore written in the form

$$\mathscr{P} = \mathscr{P}_0 r^{-p} f(\theta) \tag{4.13}$$

and the field becomes

$$\boldsymbol{B} = B_0\, r^{-(p+2)} \left[-f'(\mu),\ \frac{p f(\mu)}{\sin\theta},\ X_\theta\right]\,. \tag{4.14}$$

The two scalar equations obtained from the force free condition are the Grad Schlüter Shafranov, and the relation

$$\frac{\mathrm{d}(\sin\theta X_\theta)}{\mathrm{d}\mu}\frac{1}{\sin\theta X_\theta} = \frac{p+1}{p}\frac{1}{f(\mu)}\frac{\mathrm{d}f}{\mathrm{d}\mu} \tag{4.15}$$

which, once integrated, results in

$$\sin\theta X_\theta = \lambda f^{1+1/p}\,. \tag{4.16}$$

Once the expression for X_θ is introduced into the GSS equation, we obtain

$$(1-\mu^2)f''(\mu) + p(p+1)f(\mu) + \lambda^2\left(\frac{p+1}{p}\right) f^{1+2/p} = 0 \tag{4.17}$$

that is the master equation for the generating function and correspond to equation (3.7) upon the substitution $C = \lambda\sqrt{1+1/p}$.

The Euler potentials are not uniquely determined, and the same axisymmetric field can be obtained from different expressions of $\psi_{1,2}$.
Another set of Euler potentials that lead again to the axisymmetric field is obtained, as an example, requiring a separated-variables form

$$\begin{aligned}\psi_1 &= K_1\, r^{-p_1} f_1(\theta)\, e^{iA\phi} \\ \psi_2 &= K_2\, r^{-p_2} f_2(\theta)\, e^{-iA\phi}\end{aligned} \tag{4.18}$$

where the exponential $e^{-iA\phi}$ in ψ_2 is determined by the requirement of a resulting field not depending on ϕ. In this case the poloidal function becomes

$$\mathscr{P} = \psi_1 \cdot \psi_2 = \mathscr{P}_0\, r^{-p} f(\theta) \tag{4.19}$$

and introducing the notations:

$$\begin{aligned}p &= p_1 + p_2 \\ f(\theta) &= f_1(\theta) \cdot f_2(\theta) \\ X_\theta &= p_2\, f_2(\theta) f_1'(\theta) - p_1\, f_1(\theta) f_2'(\theta)\end{aligned} \tag{4.20}$$

we obtain again the field in equation (4.14) and consequently to equation (4.17).

This second form of the potentials lead naturally to the construction of non symmetric fields, thus contributing to create a unique algorithm useful both for the axisymmetric and for the generic case.

4.2 Non-axisymmetric fields

In order to obtain a non-axisymmetric force-free field a different choice of the Euler potentials with respect to those in equation. (4.9) or equation. (4.18) is needed.
When requiring separation of variables for the potentials themselves, rather than for the flux function, we can choose

$$\begin{aligned}\psi_1 &= K_1\, r^{-p_1} f_1(\theta)\, e^{iA\phi} \\ \psi_2 &= K_2\, r^{-p_2} f_2(\theta)\, e^{iB\phi}\end{aligned} \tag{4.21}$$

In addiction to the notations (4.20) we define two parameters, Q and M as

$$\begin{aligned}Q &= Bp_1 - Ap_2 \\ M &= A + B\end{aligned} \tag{4.22}$$

The resulting field therefore is

$$\boldsymbol{B} = B_0\, r^{-(p+2)} e^{iM\phi} \left[\frac{i(Qf' + MX_\theta)}{p\sin\theta},\ \frac{iQf}{\sin\theta},\ X_\theta\right] \tag{4.23}$$

where the term $e^{iM\phi}$ causes the field to be non-axisymmetric.

Once this field is introduced into the force-free condition, we obtain two independent equations:

$$\begin{aligned}\frac{\mathrm{d}(\sin\theta X_\theta)}{\mathrm{d}\mu}\frac{1}{\sin\theta X_\theta} - \frac{1+p}{p}\frac{f'}{f} + \\ + M\left[\frac{Q}{\sin^2\theta X_\theta}\left(f + \frac{f'^2}{p^2 f}\right) + \frac{2M}{p^2}\frac{f'}{\sin^2\theta\, f} + \right. \\ \left. - \frac{1+p}{p\,Q}X_\theta + \frac{M^2}{p^2 Q}\frac{X_\theta}{\sin^2\theta f}\right] = 0\end{aligned} \tag{4.24a}$$

$$\begin{aligned}(1-\mu^2)\frac{Q}{p}f'' + Q(p+1)f - \frac{p+1}{Q}\frac{\sin^2\theta\, X_\theta^2}{f} + \\ + \frac{M}{p}\left[X_\theta' + \frac{X_\theta}{Qf}(Qf' + MX_\theta)\right] = 0\end{aligned} \tag{4.24b}$$

At variance with the axisymmetric case, the simultaneous resolution of both equations is now needed.

A particular case of these equations is obtained when $B = -A$, that corresponds to the Euler potentials (4.18) and therefore should conduce again to the axisymmetric case. The parameters become $M = 0,\ Q = -ip$ and the equations, as expected, reduce to

$$(1-\mu^2)f'' + p(p+1)f + \frac{p+1}{p}\frac{\sin^2\theta\, X_\theta^2}{f} = 0 \tag{4.25}$$

$$\frac{\mathrm{d}(\sin\theta X_\theta)}{\mathrm{d}\mu}\frac{1}{\sin\theta X_\theta} - \frac{1+p}{p}\frac{f'}{f} = 0\,. \tag{4.26}$$

The system (4.24) then is effectively a generalization of the master equation for the axisymmetric case.

4.2.1 Boundary conditions

The unknown quantities that have to be found when solving the set of equations (4.25), are the functions f, X_θ (that in the axisymmetric case was $X_\theta = f^{1+1/p}$), and the parameters Q, M. Being a second order differential system, five boundary conditions are needed in order to solve the aforementioned equations are needed. These are set based on the same physical requirements used in the axisymmetric case, that are a purely radial field on both poles of the integration domain and a constant field intensity out of an hemisphere.

As an example, for the dipolar case, the boundary conditions are set as follows. Let the north magnetic pole be located, on the stellar surface, at (Θ, Φ) (with the south pole,

consequently, located at $(\pi - \Theta, \pi + \Phi)$). Then the conditions become

$$\begin{aligned} B_\theta(\Theta, \Phi) = B_\phi(\Theta, \Phi) = 0 \\ B_\theta(\pi - \Theta, \pi + \Phi) = B_\phi(\pi - \Theta, \pi + \Phi) = 0 \\ B_r(\Theta, \Phi) = \text{const.}\ \forall p \end{aligned} \tag{4.27}$$

For higher order multipoles, as in the axisymmetric case, the domain is divided into intervals bounded by successive poles. Thus the previous boundary conditions become

$$\begin{aligned} B_\theta(\Theta_N, \Phi_N) = B_\phi(\Theta_N, \Phi_N) = 0 \\ B_\theta(\Theta_S, \Phi_s) = B_\phi(\Theta_S, \Phi_S) = 0 \\ B_r(\Theta_N, \Phi_N) = \text{const.}\ \forall p \end{aligned} \tag{4.28}$$

where the consecutive poles are located at (Θ_N, Φ_N), for the north magnetic pole, and (Θ_S, Φ_S), for the south magnetic one.

At present, the equations for the non-axisymmetric case have not yet been solved numerically. Nevertheless, the solutions, once found, could give more insights on the qualitative analysis of the spectra collected from magnetars.

Conclusions

As first discussed by Thompson et al. [116], the external magnetic field of a magnetar likely possesses comparable poloidal and toroidal components. Twisted magnetospheres around ultra-magnetized neutron stars have been shown to play a crucial role in shaping the emergent spectrum of SGRs/AXPs quiescent emission through efficient resonant scattering of thermal photons onto the charge carriers flowing along the field lines [76, 43, 93].

In this first part of this work we tackled the problem of constructing sheared magnetic equilibria more general than a dipole. We have show how sheared multipolar fields of arbitrary order can be computed by generalizing previous results by Wolfson [127] and Thompson et al. [116]. In order to assess the effects of different external field topologies on the emitted spectrum and pulse profiles we run a number of Monte Carlo simulations, using the code of Nobili, Turolla & Zane [93], and compared the results to those of a sheared dipolar field. Not surprisingly, the overall spectral shape does not change in going from a dipole to higher order multipoles and can be always described in terms of a "blackbody plus power-law". There are, however, quite substantial differences among the multipoles in the spectra viewed at different angles. These are mainly due to the different particle distribution in the magnetosphere which is directly related to the assumed field topology.

The case of an octupolar field has a special interest because it can be used to mimic a twist localized in a region close to the magnetic pole(s), and hence to investigate the properties of spectra produced in locally twisted magnetospheres. We have computed model spectra and lightcurves for the cases in which the twist is confined to one or both polar regions (each region has semi-aperture $\theta \sim 60^\circ$), by assuming that only the polar lobes have a non-vanishing shear while the equatorial belt is potential. Quite interestingly, a twist confined to a single lobe is the only configuration, among those we have explored, that is able to reproduce the main features of the high-energy ($\sim$ 10–200 keV) emission observed with *INTEGRAL* from the AXPs 1RXS J1708-4009 and 4U 0142+61, in particular the large variation in the pulsed fraction at different energy bands [31, 32].

All magnetic equilibria we discussed in chapter 3 are globally twisted, axially symmetric multipolar fields. Of course, these configurations are far from being general and, even restricting to axial symmetry, represent only a subset of the solutions of the force-free equation. The magnetic field of a magnetar is likely to be quite complex. Modelling it in terms of single multipolar components offers a way of gaining insight on the general properties of the magnetosphere but is far from providing a realistic picture of these sources. A major obstacle in obtaining more complete models for the sheared field is non-linearity of the force-free

equation. Given two force field-free fields, $\boldsymbol{B}_1$ and $\boldsymbol{B}_2$, the linear combination $a\boldsymbol{B}_1 + b\boldsymbol{B}_2$ (with a and b two constants) is itself force-free only if $(\boldsymbol{\nabla} \times \boldsymbol{B}_1) \times \boldsymbol{B}_2 + (\boldsymbol{\nabla} \times \boldsymbol{B}_2) \times \boldsymbol{B}_1 = 0$. This implies that a generic sheared field cannot be expressed as an expansion of sheared multipoles, or, conversely, that the superposition of twisted multipoles is not a force-free field. An obvious case in which the previous condition is satisfied is that of potential fields. Since sheared fields depart smoothly from potential multipoles for $p \sim p_0$, for small enough twists a linear combination of force-free twisted multipoles (all with the same twist angle) may provide an approximate force-free field.

Despite many efforts have been devoted to develop techniques for solving the force-free equation, $\nabla \times \boldsymbol{B} = \alpha(\boldsymbol{x})\boldsymbol{B}$, no general, affordable method has been presented so far. The case of α a constant has been discussed long ago by Chandrasekhar & Kendall [23] and more recently by Mastrano & Melatos [78], in connection with magnetars. If α is a known function of position, Cuperman & Ditkowski [26] presented an analytical method for solving the force-free equation also in the non-axisymmetric case. However, this is of little use for the problem of constructing self-consistent force-free magnetospheres since prescribing α is tantamount to assign the currents which sustain the field, while for the case at hand the field and the supporting currents depend on each other. A completely general, analytical technique has been proposed by Uchida [120, 121]. This is based on a relativistic (tensor) description of the electromagnetic field and on the introduction of two scalar potentials which are the analogues of the classical Euler potentials. It has been shown to be workable in the axisymmetric case [a non-aligned rotator, 122] and, for the particular case of a non-rotating, aligned magnetosphere, in Chapter 4 equation (3.7) has been recovered. In the general case the description of the field by means of the two Euler potentials, leads to a system of differential equations describing the force free condition. The possible choice for the boundary conditions have been described for the generic case. Further work on this topic is in progress and will be the subject of a subsequent paper (Pavan et al., in preparation).

Part II

Chapter 5

Interstellar Absorption

Interstellar absorption still represents an obstacle in many observations and studies, both inside and outside our Galaxy. It modifies stellar luminosity dimming the source as well as reddening it. In any stellar study, therefore, this effect has to be considered. Modifying the apparent magnitude, interstellar extinction plays an important role in the determination of objects distances too.
A consistent portion of the Galaxy is composed of interstellar dust and gas. These, absorbing and scattering light coming from luminous sources, strongly modify the signals we receive. About 30% (Bernstein, Freedman & Madore [10]) of the energy emitted from the stars in all the Universe is absorbed and re-emitted in the infrared range.
Interstellar absorption, historically, has been introduced in a series of papers by Trumpler in the thirties, in which he analyzed the distribution of galactic open clusters. In order to calculate the distance of 100 galactic clusters, he followed two different methods. In a first case the magnitudes and spectral types of the individual members of each cluster had been considered, and their "photometric distance" was extracted. The second measure, instead, was derived from a classification of the clusters based on the stellar concentration towards the center and with the total number of stars contained. Not surprisingly the linear diameters were found to be correlated to both these parameters. What Trumpler called the "diameter distance" of the clusters, then, was obtained from a comparison of the apparent angular diameter with the mean linear diameter of the related subclass. Plotting the photometric distances and the diameter ones, he observed a systematic difference between the two measures (see figure 5.1), that were increasing with photometric distances. As no bias due to errors of observations or selection effects was found to account for this, such a discrepancy could only be explained assuming that the light was absorbed along its path towards us, and that this effect was greater for longer distances.

Interstellar extinction at the wavelength λ is given by

$$A_\lambda = -2.5 \log_{10} \left(\frac{F_\lambda}{F_\lambda^0} \right) \tag{5.1}$$

where F_λ is the absorbed flux, while F_λ^0 is the unabsorbed one. Often absorption is normal-

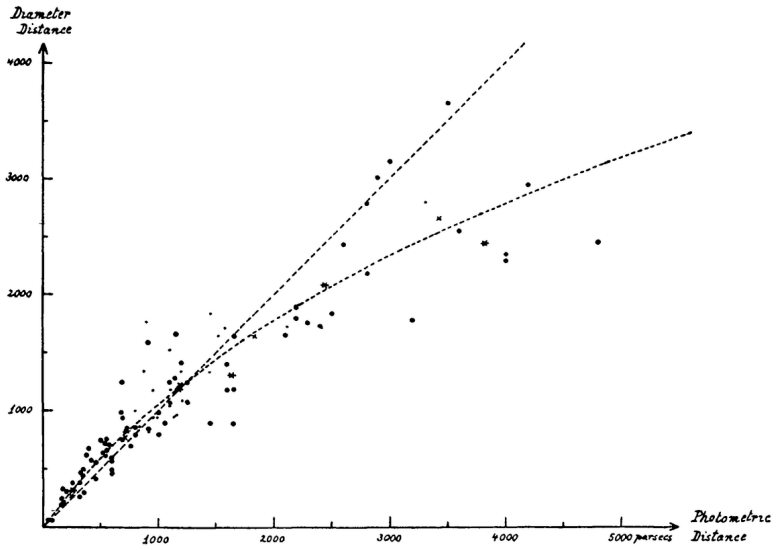

Figure 5.1: *Distance obtained from spectral type classification and apparent magnitude (abscissas) vs. those obtained from angular diameter measures (ordinates) for 100 galactic open clusters. The straight line sign equivalent distances, while the dotted one is calculated assuming a uniform trend of 0.7 mag/Kpc. Original figure extracted from Trumpler [119].*

ized to the V-band, giving the colour excess

$$E_{\lambda-V} = A_\lambda - A_V = -2.5 \log_{10} \left(\frac{F_\lambda}{F_V} \frac{F_V^0}{F_\lambda^0} \right) \tag{5.2}$$

and this can be again normalized as a function of E_{B-V}

$$\frac{E_{\lambda-V}}{E_{B-V}} = \frac{A_\lambda}{E_{B-V}} - \frac{A_V}{E_{B-V}} = \frac{A_\lambda}{E_{B-V}} - R_V \ . \tag{5.3}$$

The total-to-selective visual extinction $R_V = A_V/E_{B-V}$ is approximately in the range $2-5.5$, with a mean typical value of $R_V = 3.1$.

5.1 Measures of extinction, absorption and reddening

The methods used to determine the interstellar extinction can be classified mainly into photometric and spectroscopic ones. In the first case the absorption measure is derived from a photometric classification of the objects. This method gives the colour excess $E_{(\lambda-V)}$, rather than a direct measure of the absorption A_λ. In the second case, absorption is derived from measures of low ionization lines observed in the stellar spectra. These lines are due to dust and gas located between the source and the observer, thus the measured quantity is the column density of the absorbing particles. This quantity is expressed in terms of the equivalent amount of hydrogen N_H, i.e. the number of hydrogen atoms in a 1 cm^2 column that produces the same extinction. In order to compare the measures obtained with the

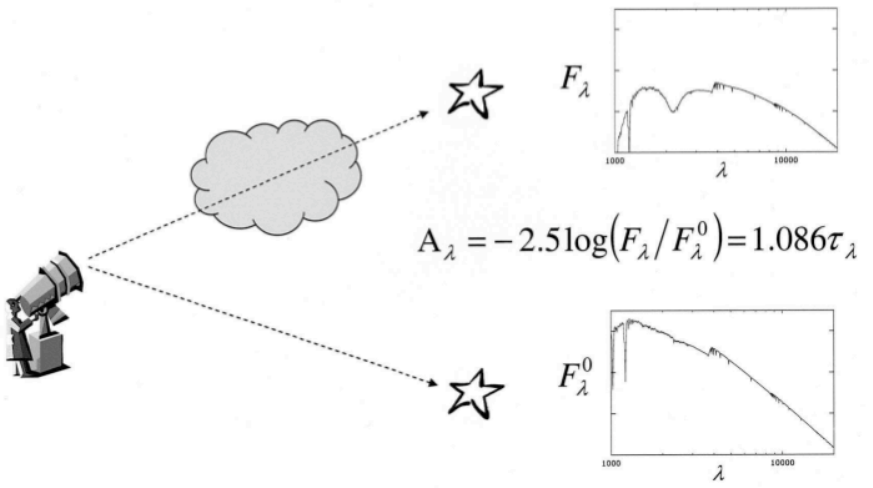

Figure 5.2: *Schematic explanation of the "pair method". Image extracted from Fitzpatrick [46]. See text for more details.*

different methods, the gas-to-dust ratio (e.g. Bohlin, Savage & Drake [11], Predehl & Schmitt [102] and references therein) is used

$$\frac{N_H}{A_V} \sim 1.8 \cdot 10^{21} \text{atoms cm}^{-2} \text{ mag}^{-1} \ . \tag{5.4}$$

One of the spectroscopic methods used to determine galactic absorption at different wavelengths, is the so called "pair method" (see figure 5.2). This method is based on the comparison of spectra of two stars of equal spectral class, one lightly and the other strongly absorbed. This permits an observer to obtain the extinction curve of the absorbing zone as a function of wavelength. The method, in order to be precise, would require the comparison between two identical stars, located at the same distance from the observer. Extinction curves obtained from different directions (figure 5.3a.), intercept different absorbing zones, or equivalently different R_V values. The curves display similarities among each other, and an important common feature is the correlation between the optical/IR and the UV part of the same curve, with curves corresponding to zones of higher R_V displaying lower UV absorptions. This characteristic allows to create synthetic curves as a parametric family (hereafter denoted as "CCM relations"), where each curve is labelled by a different value of R_V (Cardelli, Clayton & Mathis [22], see figure 5.3b.).

In figure 5.3c. we have reported the curve referred to the mean value of $R_V = 3.1$. The main feature of this curve, and any other curve of the family, is the absorption peak located at 2175 Åfirst studied by Stecher in 1969, and still argument of many papers. This bump displays mildly variation on its centroid. Though great efforts have been done (see for example the series of papers by Fitzpatrick, published from 1986 to 2005), the physical process that give rise to the bump is not fully understood yet. The more accredited explanation is that the bump itself is due to coatings on the graphite grains in the interstellar medium, while the

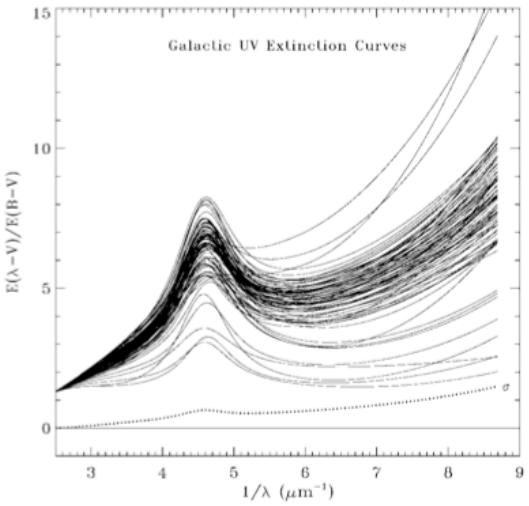

(a) *Measured galactic extinction curves.*

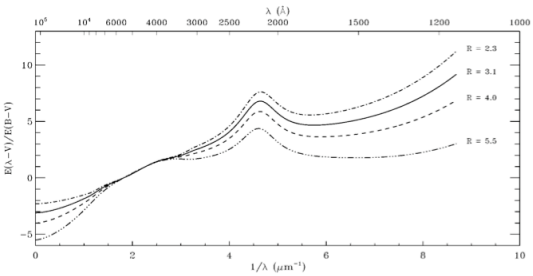

(b) *CCM parametric curves.*

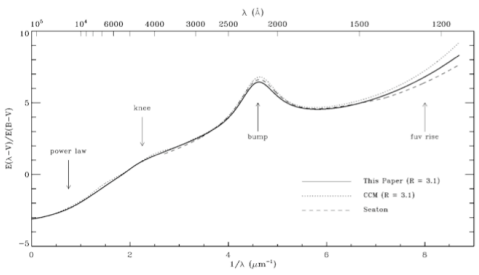

(c) *Mean extinction curve in the Galaxy.*

Figure 5.3: *(a) Observed extinction curves at different galactic directions, corresponding to different R_V values. (b) CCM parametric curves, modelling the observed ones. The different curves correspond to different values of the parameter R_V. (c) Mean extinction curve in the Galaxy, for a value of $R_V = 3.1$, showing the principal features of the curve.Images from Fitzpatrick [45].*

variations of the center of the feature and its Full Width at Half Maximum (FWHM) occur when observing through diverse environments.

Fitting the peak with a lorentzian (Seaton 1979), and measuring its intensity, it is possible to determine the dust abundance towards the source. Another feature is the power-law shape at infrared wavelengths ($\lambda = 1.2\mu m$), i.e. $E_{\lambda-V}/E_{B-V} \propto \lambda^{-1.84}$. This trend is quite constant at any direction. As the extinction is greater at shorter wavelengths, the absorption is also commonly referred to as "reddening".

The extinction curves obtained for external galaxies lead to a comprehension of dust properties and permit a comparison of the absorption effects produced by different environments. Gordon et al. [54] studied extinction in the Magellanic Clouds (figure 5.4). Some of the curves are very similar to that obtained in the Milky Way, and could be fitted with the same CCM relation, thus giving a determination of the parameter R_V for the Magellanic Clouds. In many cases, though, the CCM model does not reproduce these curves. It is clear that the relation used in the model should take into account a greater number of parameters including, as an example, a variable N_H/A_V.

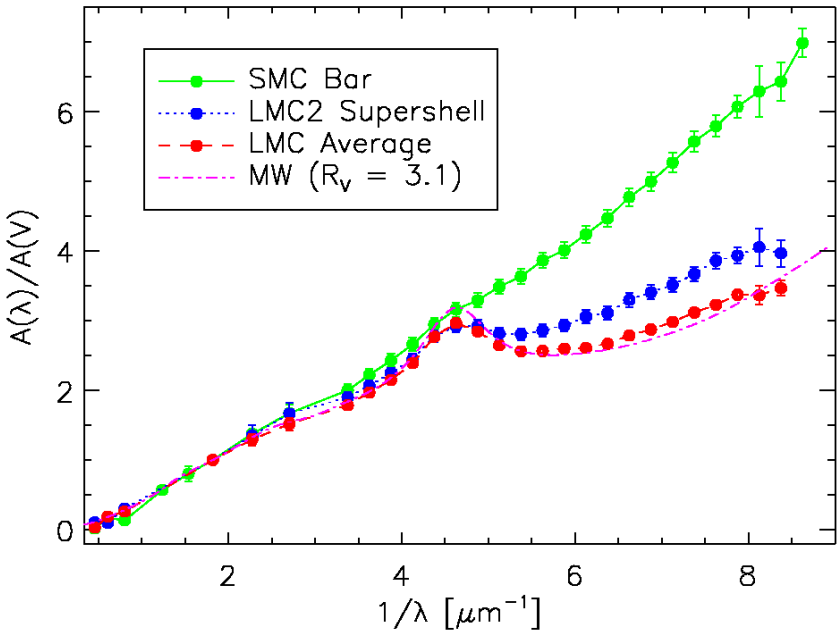

Figure 5.4: *Extinction curves obtained for SMC, LMC, and the mean Milky Way ($R_V = 3.1$) for comparison. Image taken from Gordon et al. [54]*

The various extinction curves provide insights on the large scale distribution of the interstellar matter. This appear to be highly irregularly distributed down to small scales, with an overall concentration in the Galactic plane and towards the Galactic Center. It varies as a function of both longitude and latitude, and distinct opaque clouds of various dimensions are also present. The properties of clouds at high latitudes are different form those in the Galactic plane, with the former ones being smaller, less massive and organized in less complex structures.

5.2 Galactic absorption models

In some cases it is not possible to evaluate absorption or extinction along some lines of sight, for example when we lack suitable data. In such cases it is useful to derive the reddening from a galactic extinction model, where the distribution of the dust and the interstellar absorption is reproduced. Such models are useful for statistical analysis, although they might fail to estimate absorption observed in some individual stars.

Several studies have been done on the distribution of the extinction in our Galaxy. Most of them provide a two dimensional projection map of extinction, giving either the total or the mean extinction along each line of sight. More interesting is the class of models that provide the three dimensional distribution of the interstellar absorption, as these can be used for the analysis of galactic sources.

5.2.1 3D models

Among the three-dimensional models, we particularly analyze those proposed by Hakkila et al. [58], Drimmel et al. [36], and the one provided by Marshall et al. [77]. While the first of these models is given by a collection of maps from different authors and is accurate up to a distance of approximately 2 Kpc, the Drimmel's model is based on a Galactic dust distribution and can be used up to distances of 8 Kpc. The last model is based on the Two Micron All Sky Survey and furnishes information towards more than 64000 line of sights towards the inner regions of the Galaxy.

5.2.1.1 Hakkila et al. model

The model provided by Hakkila et al. [58] is based on a collection of several three-dimensional maps of the interstellar extinction in the Galaxy, produced by several authors, and covering different various regions of the sky. These different maps are conveniently overlapped so to obtain a global distribution. The maps utilized for the Galactic disk and intermediate latitudes are those of Neckel & Klare [92], FitzGerald (1968) and Arenou, Grenon & Gómez (1992) and the analytical law for A_V as a function of the coordinates are given by Berdonikov & Pavloskaya (1991). All these studies have been extended over their formal distance limits, assuming a statistical differential extinction value of 1.5 ± 0.5 mag/Kpc for all directions.
Finally, for the coverage of high latitudes there are a number of maps describing only individual clouds, which at these high latitudes are rare enough. Amongst these works we recall those of Penprase (1992), Magnani et al. (1985), Keto & Myers (1986) Désert et al.(1988) and Odenwald (1988).

High-extinction cloud complexes at various latitudes have been also included. Some of them are the complex associated with the Gould's belt, the Lupus clouds and those in Taurus and Perseus, and the complexes in Corona Australis , Ophiuchus/Scorpio and Orion. The clouds contours have been defined combining HI, CO and IRAS 100 μm observations and stellar counts. The extinction has been considered constant inside each one of these cloud complexes.

The model is computed in a Fortran code that provides a value of A_V once a set of three coordinates, defining a position in the Galaxy (long, lat, dist), is given. .Visual absorption is obtained after interpolation of the available data along the closest directions. This model provides accurate data up to distances of 2 Kpc approximately.

5.2.1.2 Drimmel et al. model

Three dimensional Galactic models based on optical data cannot describe accurately extinction for distances greater than $\sim 2Kpc$, due to the strong dimming of the sources. At infrared wavelengths, although, due to the fact that the extinction is approximately one tenth of that in the visible light, much greater distances can be reached. The model developed by Drimmel et al. [36] is based on near infrared (NIR) colour-magnitude diagrams, which

allow to obtain accurate extinction information up to distances of approximately 8 Kpc , corresponding to the distance between the Sun and the center of the Milky Way. This work is based, rather than on empirical measures, on a three-dimensional model of the distribution of the dust in the Galaxy. Once the dust distribution $\rho_d(\boldsymbol{r})$ is obtained through this model, the extinction along the line of sight is calculated by the following equation

$$A_V(\boldsymbol{r}) = 1.086\,\kappa_V \int_0^r \rho_d \mathrm{d}s\ . \tag{5.5}$$

The parameter κ_V is obtained modelling the extinction observed at NIR wavelengths with the Diffuse Infrared Background Experiment (DIRBE) on board the Cosmic Background Explorer (COBE) satellite.

The used three dimensional model for the dust, is described in Drimmel & Spergel [37]. It is modelled on data obtained in far infrared observations by COBE/DIRBE and is organized in the following three components: the warped disk, spiral arms (mapped by known HII regions) and a local Orion-Cygnus arm segment (see fig. 5.5).

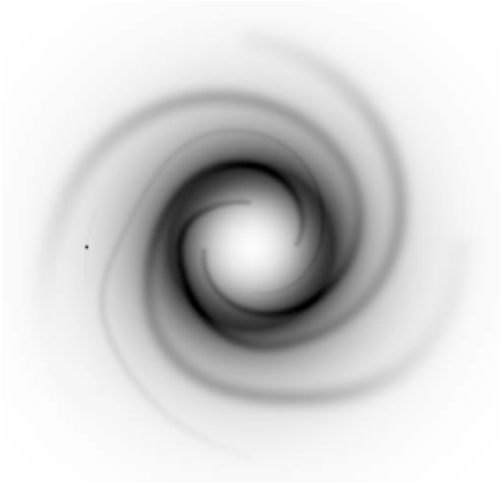

Figure 5.5: *Dust surface density as obtained from the model by Drimmel & Spergel [37], based on far-IR data from COBE/DIRBE satellite. The Sun is indicated by the point at center-left. Image from Drimmel et al. [36].*

The code supplied along with the model is organized on a (dense) three dimensional grid and the extinction values are computed on the grid nodes. In order to provide the absorption in a required position, the algorithm computes an interpolation among the four nearer points on the grid. There are three different grids available along with the code: the first is a global one, covering all the Galaxy, while the others are two local grids centered on the Sun and with a denser distribution of points, thus providing a higher accuracy. It is possible to take into account a "rescaling factor" based on the residuals between DIRBE 240 μm data and the emission predicted by the dust model. The obtained effect is to correct the dust column density resulting from the (smooth) model, by adding small scales structures not explicitly described. In order to check the accuracy, the results of the model have been compared to O and B type stars absorption data, as catalogued in Neckel & Klare [92].

Finally it is worth mentioning that the model has finite angular resolution, due to the COBE/DIRBE pixel size that, approximately, can be considered as $0.35^\circ \times 0.35^\circ$.

5.2.1.3 Marshall et al. model

The model discussed in Marshall et al. [77] is based on infrared data, as the Drimmel's one, since these allows to obtain extinction information on the densest parts of the Galaxy.

Even if this model do provide the distribution of the diffuse interstellar extinction, it is focused only on the inner part of the Galaxy, at latitudes $|b| \leq 10^{\circ}$ and longitudes $|\ell| \leq 100^{\circ}$.

The Point Source Catalogue (PSC) of the Two Micron All Sky Survey (2MASS) data, providing accurate photometry and astrometry on observed stars, together with the Besançon Stellar Population Synthesis Model of the Galaxy, are used to create the extinction model over more than 64000 lines of sight, 15′ apart one from the other.

The Besançon model (Robin et al. [104]) provide samples of simulated star counts at optical and near-infrared wavelengths and at different directions, modelling four distinct components of the Galaxy: the thin and the thick disc, with the stellar warp, the outer bulge and the spheroid, but it does not include the spiral structure. Based on theoretical grounds it is nevertheless, constrained by observations. It generates simulated catalogues, by producing, for each star, a variety of information such as magnitude, colour, distance as well as kinematic parameters, making it ideal for comparison with observations. The model is able to simulate interstellar extinction considered both as diffuse extinction and individual clouds. The former one is approximated generally with a trend of 0.7 mag/kpc. For the latter, any number of clouds can be added along the line of sight, defined by their distance and visual extinction. A cloud covers the entire field of view and therefore affects all the stars at distances greater than it. Details on the population model, as well as on the selection criteria applied on the Point Source Catalogue are explained in Marshall et al. [77].

The idea followed in this case is to map the reddening of the stars. This is achieved by comparison of the unreddened stars simulated by the Besançon model with the reddened ones catalogued in the PSC, assuming that the synthesis model successfully reproduces the average distances and intrinsic colours of the stars. The differences among the predicted and observed colours then should be due entirely to the interstellar absorption.

The procedure followed to calculate the reddening along a line of sight begins by assuming the extinction law provided by the Besançon model itself, and applying it to the simulated stars. This generated reddened stars are cut at the faint magnitude limit for the 2MASS observations in the considered field of view. Both the synthetic and observed stars are ordered in $J - K_S$ colours, that, assuming that redder stars are located at greater distances, corresponds to sort the two samples by increasing distances. The generated stars then are grouped into bins, such that the median distance in each successive bin increases. Once this is achieved, the observed stars are also grouped into bins containing the same number of stars as the simulated ones, in order to create a correspondence between the two binned samples. At this point, considering that the modelled stars have already been corrected for extinction, two groups are available, one of generated and the other of observed reddened stars, supposed to lay at the same distance and composed of the same number of stars. Then, the difference in observed $\overline{(J - K_S)}_{sim}$ and simulated $\overline{(J - K_S)}_{obs}$ extinction is computed bin by bin. The calculated extinction is associated with the median distance of the bin. Finally a χ^2 test is conducted on the observed and calculated extinction distribution.

The overall method is repeated, now substituting the initial extinction law obtained by the Besançon model with the one obtained at the end of the procedure. This steps are re-

peated iteratively until the χ^2 statistic reaches a minimum.

The extinction map, obtained this way for the various line of sights, has been projected in two dimensional planes and compared to other extinctions maps and CO surveys, obtaining good agreement in the overall distribution.

5.2.2 Schlegel et al. maps

Schlegel et al. maps (Schlegel, Finkbeiner & Davis [106]) differ significantly from the previously described models. These maps provide a bi-dimensional Galactic dust distribution along various lines of sight covering the full sky. In this case the dust distribution is not obtained with the aid of a synthetic model, but on the contrary, it is based on the observed dust emission at infrared bands. The maps are a reprocessing of the COBE/DIRBE and IRAS Sky Survey Atlas (ISSA) data.

The Infrared Astronomical Satellite (IRAS) all-sky survey was the firsts (in 1983) to map the diffuse interstellar medium, providing average infrared emission spectra at 12, 25, 60, and 100 μm. Though the mission was devoted to detect point sources, ISSA images are large-area maps, with high angular resolution. Together with these data, the full-sky images from the DIRBE experiment have also been used. These provided the absolute calibration necessary to map the dust color temperature in several passbands, but also to convert the 100 μm flux collected by IRAS into dust column density.

The flux collected by the two satellites is obtained by a superpositions of sources: the zodiacal light, extragalactic sources, Galactic point sources and finally the dust diffuse emission. All these effects have therefore been separated and subtracted, in order to leave only the dust emission. These maps, being obtained by direct observations of the interstellar dust, also revealed previously unrevealed structures as, e.g., zones of particularly low extinction (as low as $A_B = 0.02$ mag). Another result is that the dust has been shown to be tightly correlated with the HI distribution.

The bi-dimensional nature of the maps makes them particularly useful for extragalactic observations, as well as to place upper limits for the extinction values obtained by synthetic models inside the Milky Way. An example of the use of this maps as upper limits of the extinction could be found in Drimmel et al. [36], where the total modelled extinction has been obtained by integration along the lines of sight $A_V(\ell, b) = \int A_V(\ell, b, r)\partial r$ and then compared with the Schlegel's maps. In a later work by Cambrésy [17], based once again on all-sky reddening from 2MASS data, Schlegel's maps are shown to overestimate the reddening by a factor of ~ 1.5 in regions of smooth variations of the extinction with $A_V > 0.5$ while are underestimating it in regions where the extinction gradients are steep. The comparison between the near-infrared extinction and the far-infrared optical depth, in regions of $A_V > 1$ mag again shows discrepancies of 30% approximately, that are likely due to the overall presence of fluffy grains.

Chapter 6

Application of Voronoi tessellation to interstellar extinction

All the methods presented in the previous chapter depend, at different levels, on a specified geometrical model for the Milky Way, that necessarily add uncertainties on the final results. In this chapter we will describe an algorithm intended to interpolate the known values of extinction and infer the absorption towards each desired location in the Galaxy, without recurring to any model of its components. The only observable quantity that can be measured is the total extinction due to the interstellar matter laying between the observer and a star. In order to interpolate these data, as a first step, the local values of matter density in the vicinity of the stars are needed. Once these "local values" are obtained, we can integrate them along a path towards a desired point in the Galaxy, thus obtaining the required amount of extinction.

In order to evaluate the local matter density in the vicinity of a star, we have to define a finite volume that surrounds the star and can be considered its 'neighbourhood'. The more natural choice for such a volume is to consider the region formed by all those points that are nearer to this particular star than to any other star in the given catalogue of data. This correspond to the definition of a Voronoi polyhedron for the considered source. In order to construct such a structure, the Voronoi tessellation of the distribution of stars is needed.

6.1 Voronoi tessellation

In order to understand the mathematical definition of the Voronoi tessellation, it is useful to imagine a distribution of N seed points in a plane. Around each of this points a circle, or bubble, is expanding until it finally touches a neighbouring one, and it stops growing in that direction. As the bubbles start growing all at the same moment, and with the same velocity of expansion, they encounter at the intermediate point among two near seeds. The final configuration is a foam composed of N regions, each one surrounding a single seed point. This is the Voronoi tessellation (in two dimensions) of the initial seed distribution. Some examples are given in figure 6.1.

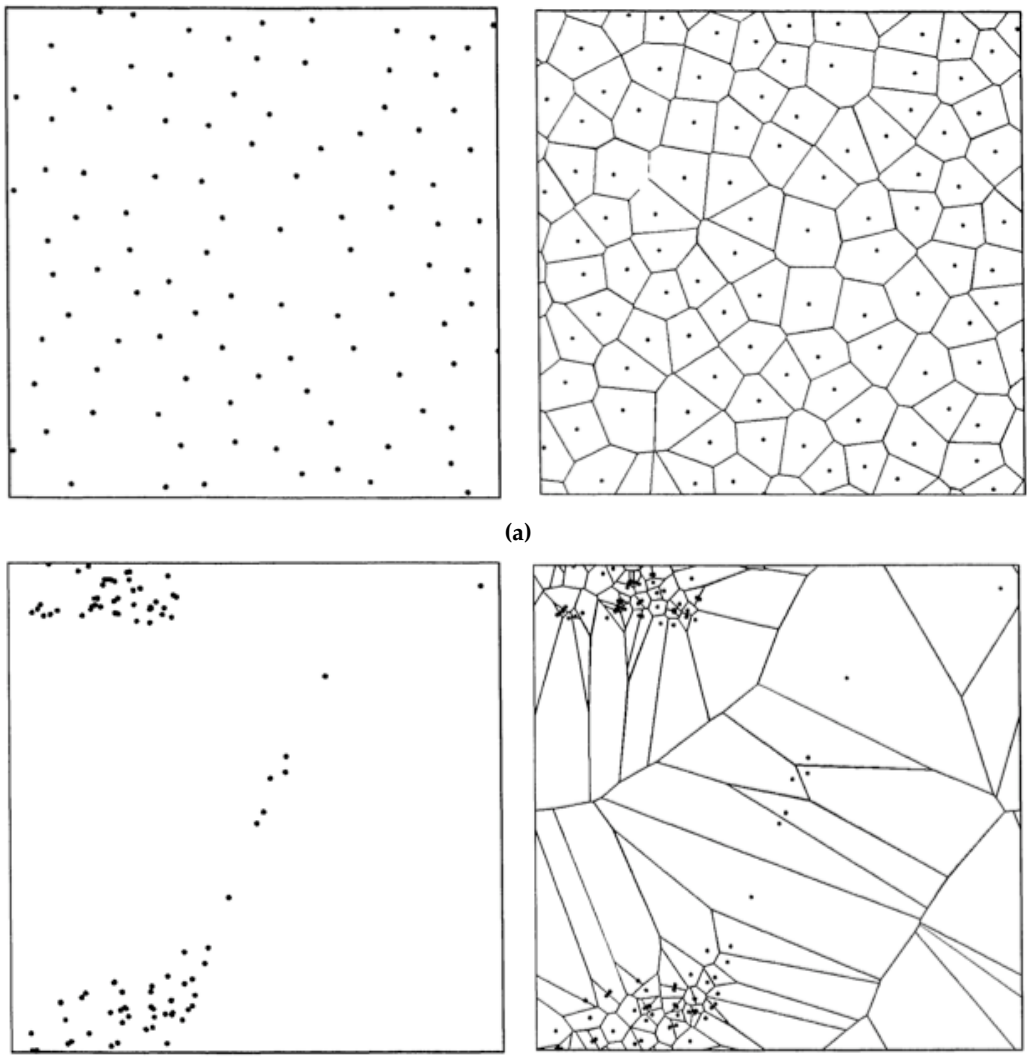

(a)

(b)

Figure 6.1: *Two examples of random distribution of points and their corresponding voronoi tessellations, obtained with periodic boundary conditions. Images taken from Icke & van de Weygaert [63]*

Formally, given a distribution of N nuclei P_i, in an arbitrary dimensional space, their Voronoi tessellation is a subdivision of space in N regions, or Voronoi polyhedrons, Π_i each one composed of all the points that are nearer to one specified nucleus rather than to any other in the collection. We may thus write

$$\Pi_i = \{x \mid d(x, P_i) < d(x, P_j) \quad \forall j \neq i\} \tag{6.1}$$

where $d(x, P)$ is the euclidean distance from x to P.
This tessellation of the space and the corresponding polyhedrons have peculiar properties. One of these, for example, is that each region, being the intersection of open half-spaces bounded by the perpendicular bisectors of the segments $P_i - P_j$, is a convex polyhedron. This geometrical tool, though known as early as 1644 (in some Descartes work), is named after Georgy Fedoseevich Voronoi, that in 1908 analyzed the properties of the tessellation in a generic n-dimensional space. This tessellation is used mainly when dealing with sponge-like or patchy distributions of elements and has applications in great number of disciplines, that span, e.g., from meteorology and geophysics, to condensed matter physics, nearest neighbor search, image reconstruction and crystallography, assuming often different names, according to the scientist that introduced the concept in each field. The same geometrical definition is known as Dirichlet regions or Thiessen polytopes, as well as fundamentals domains or polygons. In cosmological studies the tessellation is used to construct model of the large scale structures. These seem to clusters in pancakes, filaments and nodes. A Voronoi cell expanding from the center of a void region can mimic the observed structures, with the advantages of studying more and more spherical regions that always have a low density, thus being in a linear regime, whereas the same large scale structure described from the galaxies point of view, lead to aspherical structures whose density keep growing with time. An analysis of statistical properties of bi-dimensional voronoi tessellation can be found e.g. in Icke & van de Weygaert [63]

The Voronoi tessellation is a planar graph and as such it can have its associated dual graph. Given a planar graph G, its "dual graph" G^* is the one that has a vertex for each plane region of G (including the exterior region), and an edge X^* wherever G has an own edge x joining two neighboring regions (fig.6.2). Each edge X^* do cross only the corresponding edge x. The term "dual" is used because the two graphs G and G^* are one the dual graph of the other.

The dual graph of a Voronoi tessellation is the Delaunay triangulation (DT), defined as that particular connection of the nuclei P_i for which the circumcircles enclosing each triangle are empty, i.e. contains no seed points P_i (fig. 6.3). The circumcentres of the triangles, being equidistant from three seed points, are Voronoi vertex. The definition, as for Voronoi tessellation, can easily be reformulated for a generic dimensional space, or it can be extended to non-euclidean metrics.

The DT, defined in n-dimension, is also related to "convex hulls" defined in a higher dimension $n + 1$, the convex hull of a set of points being the minimum convex boundary containing those points. Because of the large interest in these mathematical tools, there are

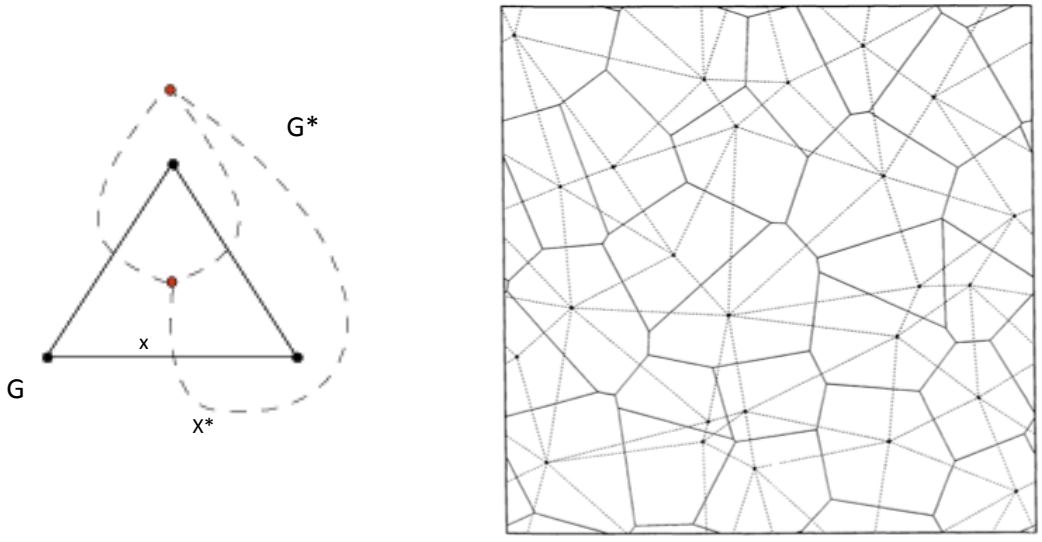

(a) *Example of dual graphs.* **(b)** *Voronoi - Delaunay duality.*

Figure 6.2: *Dual graphs. (a) The triangle composed of solid lines (G) is a plane graph, and the dashed lines form its dual graph (G*), or vice versa. (b) The dual graph of a Voronoi tessellation (solid lines) is the Delaunay triangulation (dotted lines). Image from Icke & van de Weygaert [63])*

a variety of algorithms available to construct both Delaunay and Voronoi diagrams in 2, 3 or higher dimensions.

In the original definition of Voronoi tessellation, the cells boundaries are determined by the intersections of "bubbles" expanding simultaneously from each nucleus, all at the same rate of expansion. In this case the wall common to two confining cells is equidistant from the two nuclei. Many variations on this theme can also be found, leading to diverse and useful tessellations. One of these generalizations is the tessellation that can be obtained considering diverse metrics to define the distance. For all the examples that follow, see van de Weygaert, Ph.D. Thesis [125] and references therein.

One of the possible variants is given by the *Johnson-Mehl* model. The cells of the tessellation are thought again as the final configuration obtained by bubbles expanding at the same rate from all the generating nuclei. In this case, though, the nuclei are generated by some birth process, Let us think of a configuration of nuclei, with the shells expanding at same velocity v from them. At the time t_0, the shells have dimension vt_0 that we can suppose to be less than a typical distance between two nuclei. If at this instant a nucleus is created, its cell, after a time δt, will occupy all the vacant region within the sphere $v\ \delta t$. If a nucleus is born inside a cell of another, preexisting nucleus, then it vanishes immediately. Those that survive have a cell that expands isotropically in each direction, until other confining cells are met. In the case of nuclei born all at the same instant, this tessellation coincide with the Voronoi one.

Another different generalization is given by the *weighted Voronoi tessellation*. In this case the bubbles are not expanding at the same rate, but on the contrary the growth velocity depend on the nucleus, by some weight function. One of the applications of this vari-

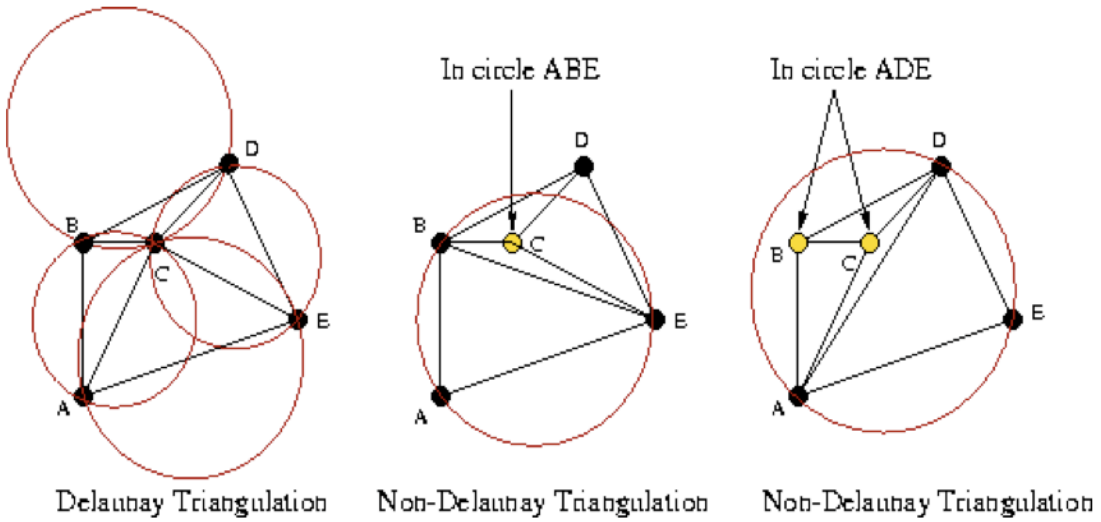

Figure 6.3: *Examples of different trinagulations for the same set of 5 points. In a Delaunay triangulation each circumcircle must be empty. This prescription is satisfied only in the left-most figure.*

ant, surprisingly, can be found in the an automatic algorithm designed to construct images with the technique of stippling (Secord [109], see fig. 6.4). The technique, initially born for typographic printing of artistic images, consists in rendering images with many dots of ink, accurately placed to create darker and lighter regions giving the impression of tone. The difficulty of the technique is to find the "well-placed" set of dots, taking care not to create spurious patterns, clumpy regions, or leave uneven voids. This effect can be reached considering centroids Voronoi tessellations (i.e. each nucleus coincide with the centroid of its Voronoi cell), and weighting different regions by the colour intensity, with cells produced in lighter regions, expanding at higher velocity. In this case the tessellation is used in a reverse approach, that is, starting from a tessellation the algorithm find the corresponding nuclei.

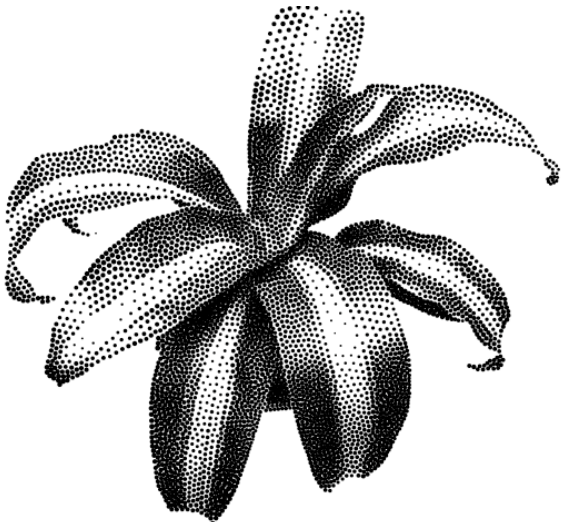

Figure 6.4: *Example of an image rendered with the stippling tecnique. The algorithm used to generate the image is based on the Weighted Voronoi tessellation (Secord [109]).*

Given a distribution of seed points occupying a three dimensional volume, again we can define the loci of points nearer to the corresponding seed rather than any other element of the distribution and therefore construct its (tridimensional) Voronoi tessellation. What we obtain in this case is a foam of convex polyhedra (see some example in fig. 6.5) that fill all the available space. The algorithms required to calculate the Voronoi foam are rather complex with respect to the 2D case. The statistical properties of three-

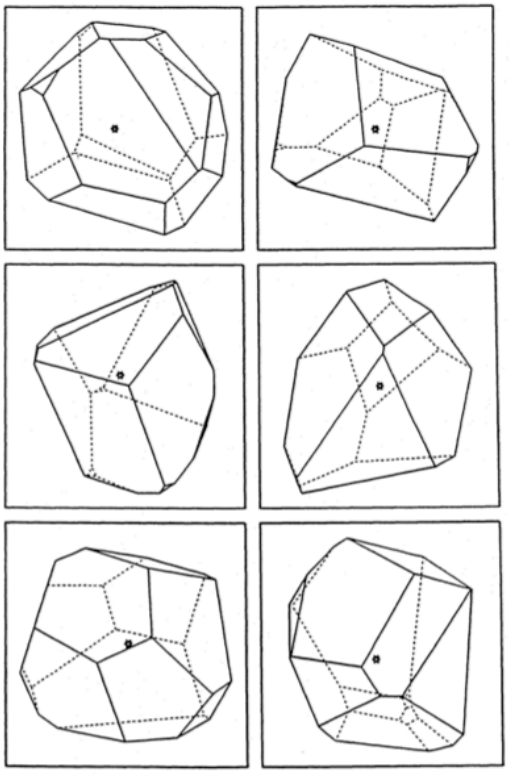

Figure 6.5: *Examples of Voronoi polyhedra in three dimensions. Image from van de Weygaert [126].*

dimensional Voronoi foams are studied, e.g., in van de Weygaert [126], van de Weygaert, Ph.D. Thesis [125], where a great number of independent nuclei-distributions has been produced via Monte Carlo simulations. One of the results of these statistical analyses is that 2D slices obtained intersecting a 3D Voronoi foam with a plane, are not, in general, 2D Voronoi tessellations themselves.

6.2 Extinction data

In order to construct the interpolating algorithm, we need information on position and absorption for as many points in the Galaxy as possible, therefore we look for these features among the available catalogues. We found basically two catalogues suited for our purposes, one is the "Catalogue of Extinction Data" produced by Neckel, Klare & Sarcander [91] with measured extinction towards more than 12,000 sources, and the "The catalogue of extinction and distances derived from UBV data" by Guarinos [57], with approximately 15,000 sources located in the solar neighborhood. Both of these catalogues have positional and distance data as well, but to further increase the precision on distance values, we considered the geometric parallax listed in the Hipparcos catalogue (with relative errors lower then 30%). All the utilized catalogues are available online at the webpage of the Centre de Données astronomiques de Strasbourg (CDS) `http://webviz.u-strasbg.fr/viz-bin/VizieR`.

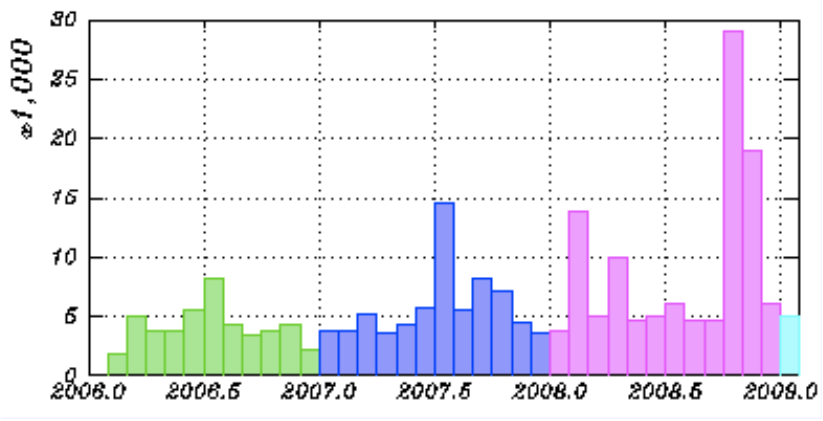

Figure 6.6: *"Popularity" of the Neckel & Klare's catalogue, extracted from the VizieR-CDS webapge. The plot shows the number of monthly requests addressed to the catalog on all VizieR mirrors.*

6.2.1 Neckel & Klare's catalogue

The catalogue, presented in Neckel & Klare [92], is composed of 12547 O to F stars (including open clusters and 7565 O and B stars) of known absorption. In addition to these data, for each entry there is a distance value as well. In some case the distance modulus has been inferred using absolute magnitudes based on the spectroscopic classification. From this data we have excluded Wolf-Rayet and δ Cephei stars that may have particular environment and a great circumstellar absorption, becoming non-representative of the nearby interstellar matter distribution. We have not considered open clusters too. As O and B stars often are associated with stellar formation sites, or can be embedded in circumstellar dusts enhancing the extinction, for a first description they have also been excluded. Some entries showed discrepant results, such as very close stars with excessively high absorption values or stars with negative colour excesses, that possibly are due to wrong spectroscopic classifications. These sources have been excluded too. After these restrictions the total sample is composed of approximately 2100 sources.

Though dating back to 1980, the catalogue is still very popular, being one of the most complete to trace absorption patterns in the Galaxy and particularly on the Galactic disk. This is evident even looking at the monthly requests addressed to it (fig. 6.6), as reported in the VizieR webpageof CDS.

325 fields are identified in the galactic belt between latitudes -7.6 and 7.6 deg. This has been accomplished with photographs of the Galaxy, highlighting regions of rather homogeneous extinction and star density. A law of interstellar extinction as a function of distance, up to 3 Kpc, has been determined for each field. Some examples of the selected fields and of the extinction laws are shown in fig. 6.7.

6.2.2 Guarinos' catalogue

This catalogue (Guarinos [57]) is devoted to the study of the interstellar medium in the solar neighbourhood. It consists principally of a collection of visual extinction A_V and distances for 15449 sources, not including peculiar stars.

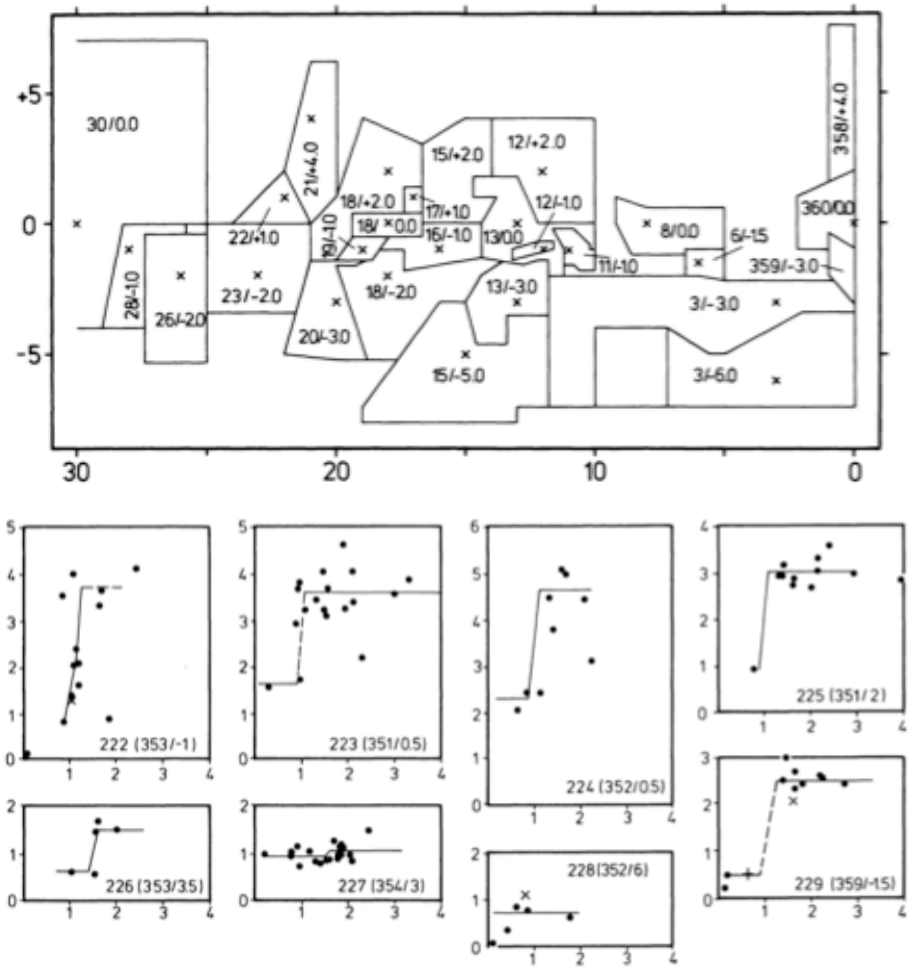

Figure 6.7: *Examples of field selection and extinction laws in Neckel & Klare. In the upper panel the ordinates are latitudes, and the abscissas are longitudes. In the lower panel some extinction law obtained for single fields are drawn. The plotted data are visual absorptions (in the ordinates, measured in mag) and heliocentric distances (in the abscissas, measured in Kpc). The field corresponding to each graph is labelled by (ℓ, b) coordinates of the centroid. Images extracted from Neckel & Klare [92].*

In order to create a catalogue as homogeneous as possible, the data are based on UBV photometry from the Mermilliod [85] compilation and MK spectral classification, obtained from the largest available spectral classifications catalogues (principally those of Houk, 1975, 1978, 1982, 1988 and Jaschek, 1978, together with those from Buscombe, 1977, and Jensen, 1983). A best-fit algorithm had been developed to assign an MK type, the corresponding absolute magnitude and intrinsic colour to the sources, and the final data are corrected for discrepant results that, as mentioned in the Neckel & Klare's case, include negative extinction values (in this case 390 sources), apparently very close stars with heavy reddening or the opposite case of apparently very far stars with low reddening. This process reduced the source number from more than 160000 objects to a final sample of 16300 stars, of whom only the 15449 with distance lower than 3 Kpc have been catalogued. Of this sample, (U-B) colours are available in 82% of the cases. The final product is the tabulated catalogue distributed by CDS, that includes absolute magnitudes, intrinsic colours $(B-V)_0$, interstellar

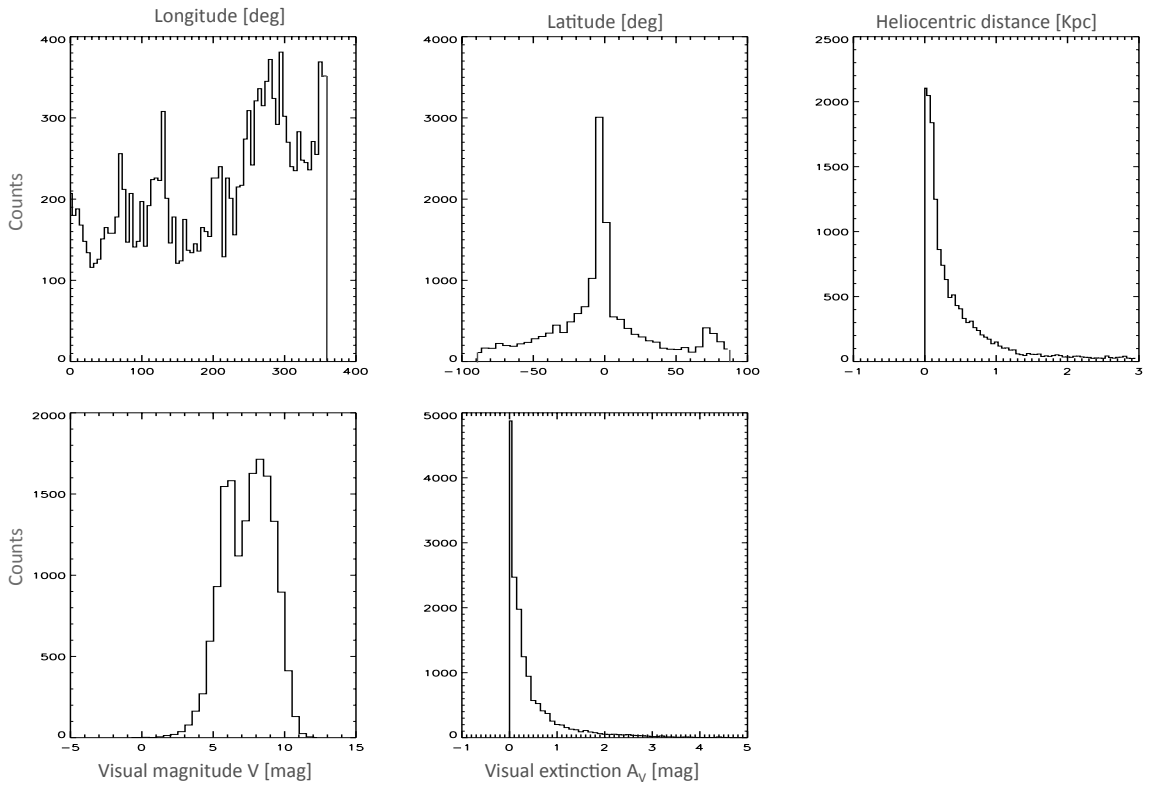

Figure 6.8: *Histograms showing the distributions for the 15500 sources in "Catalogue of extinction and distances"(Guarinos [57]).*

extinction A_V and heliocentric distance. The distributions of the data in coordinates and absorption A_V are in figure 6.2.2.

6.2.3 Hipparcos catalogue

Hipparcos (HIgh Precision PARallax COllecting Satellite) was a pioneering European Space Agency's mission devoted to the measurement of positions, parallaxes and proper motions of a huge number of stars. The satellite was launched on August 1989 and have been operative until March 1993. The primary products are the Hipparcos and Tycho Catalogues (The Hipparcos and Tycho catalogues [110]), each containing high quality astrometric and photometric data extracted from approximately 1000 Gbit of raw satellite data by four different scientific consortia (Perryman et al. [99]).

In the main Hipparcos catalogue 118,218 sources are listed with 1 milliarcsec (mas) level astrometry, while the Tycho catalogue includes much more sources (1,058,332 stars, that become 2,539,913 with the Tycho 2 Catalogue completed in 2000. These include 99% of all stars down to magnitude 11) with lesser accuracy (20-30 mas astrometry) and is the star mapper for the primary mission.

Hipparcos sources have been selected, eliminating 262 stars without known parallax and the ones with error greater than 30%. The errors are of order 0.7-0.9 mas for stars brighter

Neckel & Klare	HIPPARCOS	HD id
8889	87381	16220
9556	92487	174152
10704	101109	195406
10761	101539	196197
11243	106783	205811
11709	112450	215545
11914	114702	219175

Table 6.1: *Correspondence between HD, Hipparcos and Neckel & Klare's identifiers for seven ambiguous cases. The match has been found manually, based on coordinates and common parameters.*

than 9 mag. Because of this high astrometric precision and the vast amount of detected sources, the Hipparcos catalogue has been used to correct and integrate the distance of the catalogues described in the previous sections.

In order to cross-identify the sources in the extinction catalogues and in the Hipparcos one, the Henry-Draper (HD) and DM (Bonner, Cordoba and Cape Photographic Durchmusterung) classifications has been used. In seven cases, where more entries with the same HD identifier have been found, we have manually identified the corresponding stars (table 6.2.3) from comparisons on the provided coordinates and other parameters commons to the various catalogues.

Histograms showing the distribution of the selected 2100 Neckel & Klare's data in terms of longitude, latitude, distance and visual extinction are in figure (6.2.3). The distances are those given by the Hipparcos parallaxes.

6.3 The model

The algorithm is aimed at interpolating the catalogues data and get information abut the extinction in different positions of the Galaxy. As a first step, the Voronoi foam relative to the given set of stellar positions, is required. Once the three dimensional structure of the polyhedrons is obtained, the local density of absorption around the target star is calculated.

6.3.1 The local absorption density

Once a sample of stars with precisely known positions is obtained, it can be used to define Voronoi "generating nuclei" (here we call them equivalently *generating stars* or *nuclei*) and to calculate the corresponding tessellation. The interstellar medium inside a Voronoi cell surrounding each star is assumed homogeneous. In order to interpolate the extinction values measured towards the stars, we have to derive the density of interstellar matter in each Voronoi cell.

Let us indicate with N_0 the number of photons emitted by the source and with $N(x)$ the number of the photons detected after a column of interstellar medium of length x. The particles in the column have density n and cross-section σ. The ratio $N(x)/N_0$ per unit time,

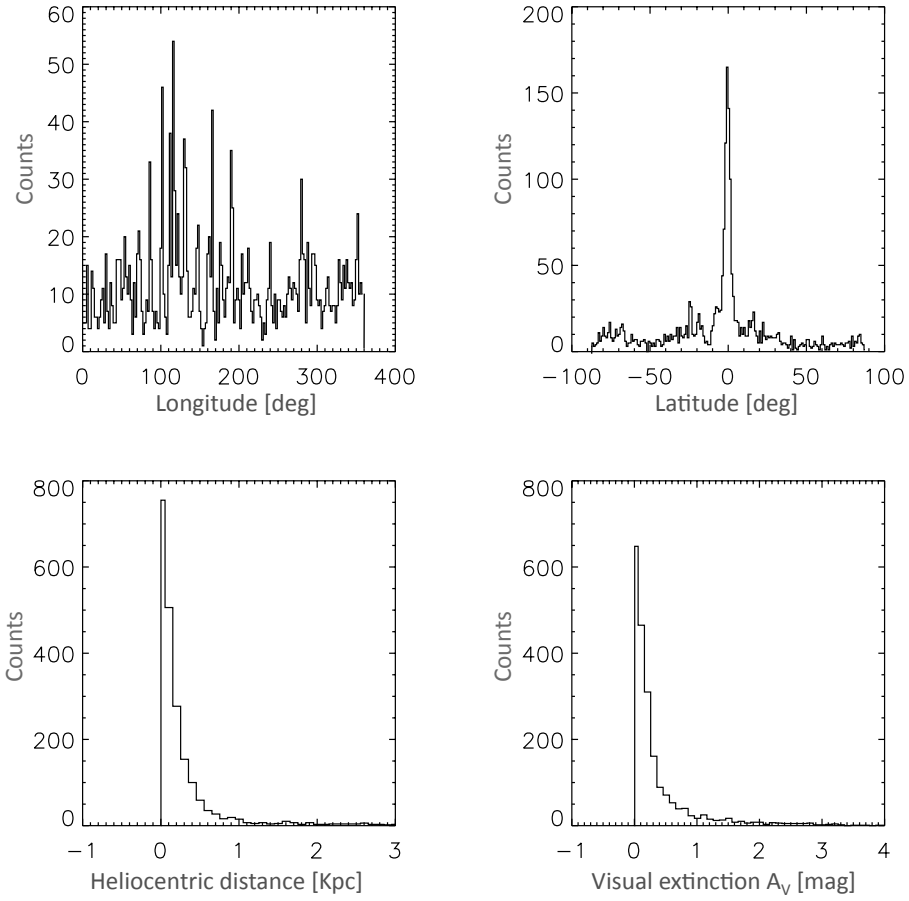

Figure 6.9: *Statistic of 2100 sources selected from "Catalogue of extinction data" (Neckel, Klare & Sarcander [91]) without considering O and B spectral type stars.*

per unit solid angle, per unit wavelength and per unit surface is given by

$$\frac{N(x)}{N_0} = \mathrm{e}^{-n\sigma x}\,\mathrm{d}t\,\mathrm{d}\lambda\,\mathrm{d}\Omega\,\mathrm{d}S\ . \tag{6.2}$$

The observed (F_λ) and the emitted (F_λ^0) fluxes are proportional respectively to the number of photons $N(x)$ and N_0, therefore the absorption, defined in equation (5.1), is proportional to $\int n\,\sigma(\lambda)\,\mathrm{d}x$. The local absorption density is

$$\frac{\mathrm{d}A_\lambda}{\mathrm{d}x} \propto n\,\sigma(\lambda) \tag{6.3}$$

and we can consider equivalently the density of interstellar medium or that of extinction inside a Voronoi cell.

6.3.2 The algorithm

Some concepts, related to the Voronoi foam, are introduced to calculate the density of extinction in the neighborhood of a star. Each star i has the corresponding extinction A_{V_i}

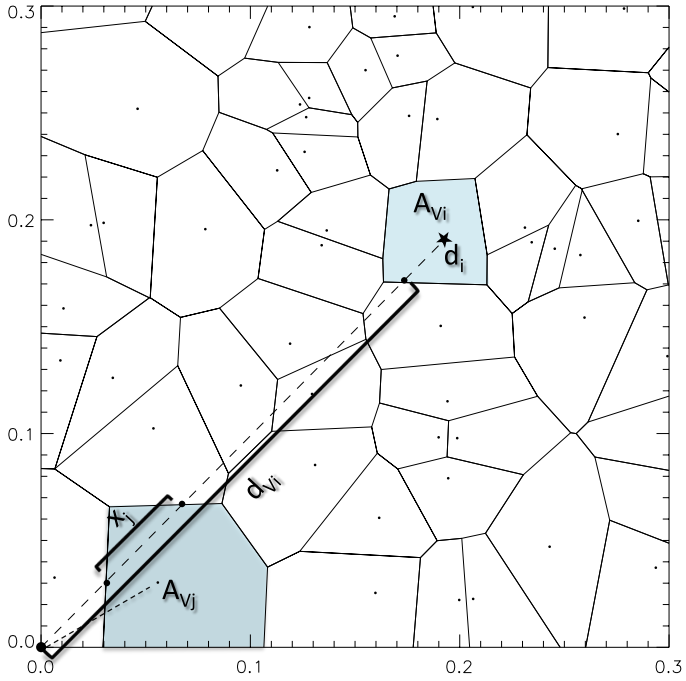

Figure 6.10: *Schematic description of the parameters defined for a Voronoi cell. The Sun is located in (0,0), stars are indicated as little dots, and their cells are traced. The graph is in arbitrary units. The line of sight towards one of the stars (i-th star, marked with a black symbol in the coloured cell) is represented by the long dashed line. The nomenclature used in the text is also drawn: the total visual extinction A_{V_i} towards the star, the heliocentric distance of the star d_i and that of the front-end (marked with a black dot) of its cell d_{V_i}. The same line of sight cross a cell j for a length x_j. Note the difference between x_j, directed towards the i-th star, and the difference $(d_j - d_{V_j})$ inside the same cell, but directed towards the j-th source.*

and heliocentric distance d_i, while d_{V_i} is the heliocentric distance of the front-edge of its Voronoi polyhedron. This last quantity is given by the interception between the line of sight and the Voronoi cell, as shown in fig. 6.10 where a bi-dimensional example is illustrated.

The set of all $\{A_{V_i}\}$ are the catalogued extinctions. The underlaying idea is to define local values of extinctions ρ_{A_V}, such that, integrating along a line of sight, the observed extinction is recovered.

The amount of extinction due to a single cell i (indicated with $\widetilde{A}_{V_i}$), is calculated subtracting from the visual extinction A_{V_i} of the corresponding "generating star", the contribute of all the other cells intercepting the line of sight between the observer and the i-th star.

$$\widetilde{A}_{V_i} = A_{V_i} - \int_0^{d_{V_i}} \left(\frac{\mathrm{d}A_V}{\mathrm{d}x} \right) \mathrm{d}x \ . \tag{6.4}$$

In each cell we can derive the density of absorption ρ_{A_V}, or local extinction per unit length, dividing $\widetilde{A}_{V_i}$ by the distance $d_i - d_{V_i}$ between the front-edge of its Voronoi polyhedron and the real position of the generating star.

$$\rho_{A_V i} = \frac{\widetilde{A}_{V_i}}{d_i - d_{V_i}} \ . \tag{6.5}$$

The procedure to find $\rho_{A_V i}$ is straightforward only for the front-most cells (that is the Voronoi polyhedrons of those stars for which the line of sight traverse no other Voronoi cells than its own). In such cases $d_{V_i} = 0$ and thus we have:

$$\widetilde{A}_{V_i} = A_{V_i} \qquad ; \qquad \rho_{A_V i} = \frac{\widetilde{A}_{V_i}}{d_i} \; . \tag{6.6}$$

Once we have obtained the absorption density for the front-most cells, we can calculate the local extinction of a star beyond them (where the line of sight traverse the j-th cell with a total amount x_j) replacing the integral in equation (6.4) with the sum $\sum_j (\rho_{A_V j} \cdot x_j)$.

In order to perform these calculations, an algorithm has been coded. In input, it need a file with the galactic coordinates $(\ell II, bII)$, distance and visual absorption A_V for the known stars. Where needed, the data coming from different catalogues are converted by means of the relations (5.2, 5.3). The sources must be sorted into ascending distances. Analyzing each line of sight at a time, it finds the cells crossed and evaluate the corresponding lengths x_j, storing these values into an indexed matrix. At this point it calculates the local absorption density $\rho_{A_V i}$ for the front-most cells applying equation (6.6). As the sources are sorted by increasing distances, the lines of sight of successive stars cross cells where ρ_{A_V} has already been evaluated. For these sources the algorithm calculates $\rho_{A_V i}$ with the expression (6.5), where

$$\widetilde{A}_{V_i} = A_{V_i} - \sum_{j=0}^{i-1} (\rho_{A_V j} \cdot x_j) \tag{6.7}$$

The code proceeds scanning all the stars and evaluating for each one the corresponding ρ_{A_V}. Once this step is completed, the stored values can be used to calculate the total absorption to a given point (ℓ, b, d).

6.3.3 Preliminary results

A first test, conducted to check the correctness of the algorithm, was aimed to calculate total visual absorptions in the same points where are located the input sources. If the densities ρ_{A_V} were correctly calculated, the expected outputs are again the observed A_V given in input. The results obtained when supplying a set of nearly 12000 sources, including O and B spectral type stars, and the analogous one for a sample of approximately 3000 sources, are shown in figure 6.11. The errors are smaller for the second sample, but the calculated values are in both cases very accurate.

In some cases, the $\rho_{A_V i}$ obtained are negative. This occurs when the computed $\sum_j (\rho_{A_V j} \cdot x_j)$ exceeds the observed A_{V_i} for that particular cell, but is not physically meaningful. To avoid this computational effect, a number of modifications to the original model have been considered.

The negative result can be due to the presence of very localized absorbing material (giving rise to a high measured A_V) , or to excessively vast dimensions of the preceding cells along the path. In the first case, in a $A_V/dist$ diagram this effect would be seen as an ex-

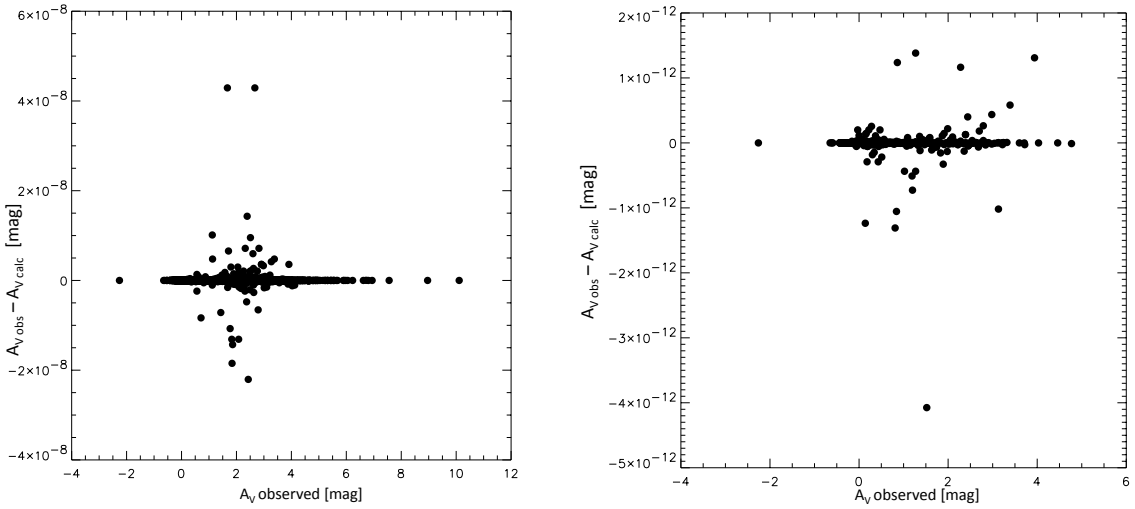

Figure 6.11: *Calculated vs. observed A_V values. The sources in input in the code are a merge of those in Neckel & Klare catalogue. On the left panel, the plot is obtained for 11623 sources, including O and B spectral type stars, while on the right for 2914 A to F stars.*

cessive rise of the extinction curve followed by a sudden decrease that bring the curve back to the observed A_{V_i} at the distance d_i. The algorithm in this case can be modified so that, whenever a negative $\rho_{A_V i}$ is obtained, the corresponding cell (i) is merged with the previous one in the line of sight $(i-1)$. Assuming that the extinction in the $i-1$ cell is overestimated, the new density for the i-th cell is obtained by

$$\rho'_{A_V i} = \frac{\left(A_{V_i} - \sum_{j=0}^{i-2}(\rho_{A_V j} \cdot x_j)\right)}{d_i - d_{V(i-1)}} \ . \tag{6.8}$$

This is equivalent to obtain a curve $A_V/dist$ with equal slope for the two last cells, that ends in the correct (A_{V_i}, d_i). When this correction is not sufficient to obtain a positive $\rho_{A_V i}$, the same procedure is followed merging the preceding cells.

The second reason for negative absorption densities, as stated above, is an excessive dimension of a number of preceding cells. In order to correct for this effect, a maximum radius has been introduced r_{max} for each cell. The Voronoi polyhedrons, then, are intersected with the maximum allowed sphere. This is particularly suited for stars belonging to rare zones, where the cells tends to be expanded (a bi-dimensional example is in figure 6.1) as well as for O or B spectral type sources, that are often associated with dense regions, or could be most probably associated with circumstellar extinctions.

The results obtained in this work are still preliminary and further investigations are still needed, in order to refine the model.

Conclusions

The interstellar medium is a mixture of particles (e.g. silicates, polycyclic aromatic hydrocarbon molecules or graphitic grains) and gas (basically hydrogen) that irregularly permeates the Galaxy, forming clouds complexes and other structures. This elusive medium has strong effects on the radiation emitted by astronomical sources, being responsible for the absorption and scattering of the electromagnetic emission.

Some of the methods used to indirectly map the interstellar absorption have been described. All these diverse models, however, need to take assumptions on the properties or distribution of a number of Galactic components. This necessarily add uncertainties to the final results.

The approach presented in this work is based on a spatial interpolation of the observed absorption, with the advantage of being independent from Galactic models. The measured extinction is given by the cumulative effect of the column of dust laying between the observer and the emitting source. To interpolate the values of absorption, therefore, a "local density" ρ_{A_V} is needed. Voronoi polyhedrons have been used in order to define the neighbourhood of each star. All the polyhedrons (or cells) together become a foam that cover the entire space. Inside each cell the matter density is assumed to be homogeneous, and this allows to calculate the absorption density ρ_{A_V} from the A_V of the generating star. The method can give reasonable results only when the Voronoi cells are small enough to consider homogeneous the enclosed matter. This translates into the need of a great number of measures of extinction. To this end the catalogues of extinctions collected by Neckel & Klare and by Guarinos have been used. The Hipparcos catalogue, besides, has been used to assign the correct distance to each star.

Once the local values of extinction have been calculated, the total amount of absorption in a new direction, $A_V(\ell, b, d)$, is obtained integrating them along the path from the observer to the point (ℓ, b, d). The algorithm have been showed to successfully reconstruct the original values, within errors of orders 10^{-8}, but it shows strong A_V fluctuations at intermediate positions. Some refinements of the basic method have been considered to avoid zones of negative densities, that were generated by the algorithm but are not physically meaningful. A maximum radius for the neighborhood of the stars has been introduced, so that the cells results from the interception between the maximum allowed sphere and the Voronoi polyhedron. This correspond to impose a limit to the dimension of the zone in which the matter is considered homogeneous. In this case there is some void space among the cells, where no contribution to the total extinction is considered. Another variation to the origi-

nal algorithm, introduced to avoid negative extinction densities, consists in considering the mean ρ_{A_V} evaluated in he three adjacent cells along the line of sight. The adopted corrections ameliorate the results of the algorithm, but other refinements are still needed to obtain higher precisions. Further developments on this topic are still in progress.

List of Figures

List of Tables

Bibliography

[1] Abramowitz M., Stegun I.A., 1972, Handbook of mathematical functions. New York, Dover publications. 1972.

[2] Alpar M.A., 2001, ApJ, 554, 1245

[3] Amôres E.B., Lépine J. R. D. 2005 AJ, 130, 659

[4] Baade W. 1942 ApJ 96, 188

[5] Baade W., Zwicky F., 1934, PNAS, 20, 254

[6] Baring M., Harding, A., 2007, Ap&SS, 308, 109

[7] Baring M., Harding, A., 2008, Astrophysics of Compact Objects, International Conference on Astrophysics of Compact Objects. AIP Conference Proceedings, 968, 93 [arXiv:0804.0435]

[8] Beloborodov A., Thompson C., 2007, ApJ, 657, 967

[9] Bernardini F., et al. 2008, A&A, submitted

[10] Bernstein R.A., Freedman W.L., Madore B.F. 2002 ApJ 571, 107

[11] Bohlin R.C., Savage B.D., Drake J.F. 1978 ApJ 224, 132

[12] Braithwaite J., Spruit H.C., 2006, A&A, 450, 1097

[13] Braithwaite J. 2008, MNRAS submitted, arXiv:0810.1049

[14] Bronzan J.B., 1971, AJP, 39, 1357

[15] Burwitz V., Haberl F., Neuhäuser R., Predehl P., Trümper J., Zavlin V. E. 2003 A&A, 399, 1109

[16] Cambrésy L. 1999 A&A 345, 965

[17] Cambrésy L. et al. 2005 A&A 435, 131

[18] Cameron, A.G.W. 1959, ApJ, 130, 884

[19] Camilo F., Ransom S.M., Halpern J.P. , Reynolds J., 2007, ApJ, 666, L93

[20] Camilo F., Reynolds J., Johnston S., Halpern J.P., Ransom S.M., van Straten W. 2007, ApJ, 659, L37

[21] Castro-Tirado A.J. et al. 2008 Nature, 455, 506

[22] Cardelli J. A., Clayton G. C., Mathis J. S. 1989 ApJ 345, 245

[23] Chandrasekhar S., Kendall P.C. 1957, ApJ, 126, 457

[24] Cholonieswski J., Valentijn E.A. 2003 AcA 53, 265

[25] Choudhuri A.R. "The Physics of Fluids and Plasmas. An Introduction for Astrophysicists" Cambridge University Press, 1976. Cap.14

[26] Cuperman S., Ditkowski A. 1991, A&A, 241, 646

[27] Dall'Osso S. et al. 2003, ApJ, 599, 485

[28] Dall'Osso S., Shore S.N., Stella L. 2008, MNRAS submitted, arXiv:0811.4311

[29] Dame T.M., Thaddeus P. 2004 ASP Conf.Ser. 317

[30] De Luca A., Caraveo P.A., Esposito P., Hurley K. 2008, ApJ in press, arXiv:0810.3804

[31] Den Hartog P.R., Kuiper L., Hermsen W., Kaspi V.M., Dib R., Knödlseder J., Gavriil F.P. 2008, A&A, 489, 245

[32] Den Hartog P.R., Kuiper L., Hermsen W. 2008, A&A, 489, 263

[33] Draine, B. T. 2003 ARA&A 41,241

[34] Draine, B. T.; Li, A. 2007 ApJ, 657, 810

[35] Drake J.J. et al. 2002 ApJ, 572, 996

[36] Drimmel R., Cabrera-Lavers A., López-Corredoira M. 2003 A&A 409, 205

[37] Drimmel R., Spergel D.N. 2001 ApJ 556, 181

[38] Duncan R.C., Thompson C., 1992, ApJ, 392, L9

[39] Dutra C.M. , Bica E. 2000 A&A 359, 347

[40] Ekşi, K.J. , Alpar M.A., 2003, ApJ, 599, 450

[41] Ertan Ü. , Alpar M.A., 2003, ApJ, 593, L93

[42] Esposito P., Tiengo A., Mereghetti S., Israel G.L., DeLuca A., Götz D., Rea N., Turolla R., Zane, S. 2008, ApJ Letters in publication, arXiv 0812.0014

[43] Fernandez R. , Thompson C., 2007 ApJ, 660, 615

[44] Feroci M., Hurley K., Duncan R.C., Thompson, C. 2001, ApJ, 549, 1021

[45] Fitzpatrick E.L. 1999 PASP 111, 63

[46] Fitzpatrick E.L. 2004 astro-ph/0401344

[47] Fitzpatrick E.L., Massa D. 2007 ApJ 663, 320

[48] Fuchs Y., Mirabel F., Chaty S., Claret A., Cesarsky C. J., Cesarsky D. A. 1999, A&A, 350, 891

[49] Gaensler B. M., McClure-Griffiths N. M., Oey M. S., Haverkorn M., Dickey J. M., Green A. J., 2005, ApJ, 620, L95

[50] Gavriil F. P., Gonzalez M.E., Gotthelf E. V., Kaspi V. M., Livingstone M.A., Woods, P. M. 2008 Science, 319, 1802

[51] Garcia de Andrade L. C. 2006 PhPl 13b, 2309

[52] Goodwin S.P., Mestel J. , Mestel L., Wright G.A.E. 2004 MNRAS 349, 213

[53] Gotthelf E. V., Halpern J.P. 2008 AIPC, 983, 320

[54] Gordon K. D., Clayton G. C., Misselt K. A., Landolt A. U., Wolff M. J. 2003 ApJ 594, 279

[55] Götz D., Mereghetti S., Tiengo A., Esposito P. 2006, A&A, 449, L31

[56] Gruzinov A. 2007 ApJ 667L, 69

[57] Guarinos J. 1995 yCat.5086 0G

[58] Hakkila J., Myers J.M., Stidham B.J., Hartmann D.H. 1997 AJ 114, 2043

[59] Harding A.K., Lai D. 2006, Rep. Prog. Phys., 69, 2631

[60] He H., Wang H., arXiv 0704.0156

[61] Heyl J.S. 2005, astro-ph, 0504077

[62] Hudson T.S., Wheatland M.S. 1999 SoPh 186, 301

[63] Icke V., van de Weygaert R. 1987 A&A 16, 32

[64] Kasumov F.K., Allahverdiev A.O. 2008 A&A submitted, arXiv:0810.5264

[65] Keane E.F., Kramer M. 2008, MNRAS submitted, arXiv:0810.1512

[66] Kondratiev V.I. et al. 2008 ApJ submitted

[67] Kuiper,L., Den Hartog P.R., Hermsen, W., 2008, arXiv:0810.4801

[68] Kuiper,L., Hermsen, W., Mendez, M., 2004, ApJ, 613, 1173

[69] Kuiper L., et al., 2006, ApJ, 645, 55

[70] Lattimer J.M., Prakash M. 2004 Science 304, 536

[71] Levine R.H. 1975, SoPh, 44, 365

[72] Low B.C. 1986, ApJ, 307, 205

[73] Low B.C. , Flyer N. 2007, ApJ, 668, 557

[74] Low B.C., Lou Y.Q., 1990, ApJ, 352, 343

[75] Lyutikov M. 2003 MNRAS 346, 540

[76] Lyutikov M., Gavriil F. P., 2006, MNRAS, 368, 690

[77] Marshall D.J., Robin, A.C., Reylé C., Schultheis M., Picaud S. 2006 A&A 453, 635

[78] Mastrano A., Melatos A. 2008, MNRAS, 387, 1735

[79] Marsden D., White N. E. 2001 ApJ, 551, 155

[80] Mazets E. P. et al. 1999 ApJ, 519, L151

[81] McLaughlin M.A. et al. 2006 Nature, 439, 817

[82] Mereghetti, S., et al., 2005, A&A, 433, L9

[83] Mereghetti S. 2008, A&A Rev., in press [arXiv:0804.0250]

[84] Mereghetti S., Tiengo A., Vianello G. 2006 astro-ph/0612543

[85] Mermilliod J.C. 1987 A&A.Suppl.Ser. 71, 413

[86] Mestel L. 1973 Ap & SS, 24, 289

[87] Misiriotis A. et al. 2006 A&A 459,113

[88] Minkowski R. 1942 ApJ 96, 199

[89] Muno M. P. et al., 2006, ApJ, 636, L41

[90] Mursula, K.; Hiltula, T. 2004 SoPh, 224, 133

[91] Neckel T., Klare G., Sarcander M. 1995yCat 2062

[92] Neckel T., Klare G. 1980 A&AS 42, 251

[93] Nobili L., Turolla R., Zane S., 2008a, MNRAS, 386, 1527

[94] Nobili L., Turolla R., Zane S., 2008b, MNRAS, 389, 989

[95] Page D., Sarmiento A., 1996, ApJ, 473, 1067

[96] Palmer D. M. et al. 2005 Nature, 434, 1107

[97] Pavan L., Turolla R., Zane S., Nobili L. 2008 MNRAS submitted

[98] Perna R., Gotthelf E.V., 2008, ApJ, 681, 522

[99] Perryman M.A.C. et al. 1997 A&A 323, 49

[100] Popov S.B. 2006, astro-ph, 0610593

[101] Popov S.B., Turolla R., Possenti A. 2006, MNRAS, 369, L23

[102] Predehl P., Schmitt J. H. M. M. 1995 A&A 293, 889

[103] Rea N., Zane S., Turolla R., Lyutikov M., Götz D. 2008, ApJ, 686, 1245

[104] Robin A.C., Reylé C., Derriér S., Picaud S. 2003 A&A 409, 523 (Erratum 2004 A&A 416, 157)

[105] Rosenbluth M. N., Bussac M. N. 1979 NucFu 19, 489

[106] Schlegel D., Finkbeiner D., Davis M. 1998 ApJ 500, 525

[107] Schwartz S. J. et al. 2005 ApJ, 627, L129

[108] Serylak M. et al. 2008, MNRAS submitted, arXiv:0811.3829

[109] Secord A. 2002, 2nd International Symposium on Non-Photorealistic Animation and Rendering (NPAR 2002)

[110] The Hipparcos and Tycho catalogues ESA 1997 URL: www.rssd.esa.int/Hipparcos/

[111] Thompson C., Beloborodov, A. M., 2005, ApJ, 634, 565

[112] Thompson C., Duncan R.C., 1993, ApJ, 408, 194

[113] Thompson C., Duncan R.C., 1995, MNRAS, 275, 255

[114] Thompson C., Duncan R.C., 1996 ApJ, 473, 322

[115] Thompson C., Duncan R.C., 2001, ApJ, 561, 980

[116] Thompson C., Lyutikov M., Kulkarni S.R., 2002, ApJ, 574, 332

[117] Tiengo A., Mereghetti S. 2007 ApJ, 657, L101

[118] Timokhin A. N. 2007 MNRAS 379, 605

[119] Trumpler R.J. 1930 PASP 42, 214

[120] Uchida T. 1997a, Phys. Rev. E, 56, 2181

[121] Uchida T. 1997b, Phys. Rev. E, 56, 2198

[122] Uchida T. 1998, MNRAS, 297, 315

[123] Uzdensky D. A. 2003 ApJ 598, 446

[124] Vink J., Kuiper L. 2006 MNRAS, 370, L14

[125] van de Weygaert R. 1991 *Voids and the geometry of large scale structure*, PhD thesis, Leiden.

[126] van de Weygaert R. 1994 A&A 283, 361

[127] Wolfson R., 1995, ApJ, 443, 810

[128] Woods P. M. et al. 2005, ApJ, 629, 985

[129] Woods P.M., Thompson C.. 2006, in: Compact stellar X-ray sources. Edited by Walter Lewin & Michiel van der Klis. Cambridge Astrophysics Series, No. 39. Cambridge, UK [astro-ph/0406133]

[130] Woods P.M. et al. 2007, ApJ, 654, 470

[131] Xie B.S., Yin X.T., Luo X., 2006, Phys.Scr., 73, 655